

ULTRAFAST LASER FABRICATION OF WAVEGUIDES IN GLASSES AND CRYSTALLINE MATERIALS

by

Benjamin W. McMillen

B.S. in Electrical Engineering, University of Pittsburgh 2003

M.S. in Electrical Engineering, University of Pittsburgh 2007

Submitted to the Graduate Faculty of
Swanson School of Engineering in partial fulfillment
of the requirements for the degree of
Doctor of Philosophy in Electrical Engineering

University of Pittsburgh

2012

UNIVERSITY OF PITTSBURGH
SWANSON SCHOOL OF ENGINEERING

This dissertation was presented

by

Benjamin W. McMillen

It was defended on

July 17th, 2012

and approved by

William Stanchina, PhD, Professor and Chairman, Department of Electrical and Computer
Engineering

Guangyong Li, PhD, Assistant Professor, Department of Electrical and Computer Engineering

Yiran Chen, PhD, Assistant Professor, Department of Electrical and Computer Engineering

Sung Kwon Cho, PhD, Assistant Professor, Department of Mechanical Engineering

Kevin Chen, PhD, Professor, Department of Electrical and Computer Engineering

Copyright © by Benjamin W. McMillen

2012

ULTRAFAST LASER FABRICATION OF WAVEGUIDES IN GLASSES AND CRYSTALLINE MATERIALS

Benjamin W. McMillen, PhD

University of Pittsburgh, 2012

Over the last decade, the ultrafast laser has emerged as a powerful tool to shape three-dimensional photonic circuits in transparent dielectric materials. One of the unique traits of this fabrication approach is its ability to produce photonic circuits in bulk optical substrates with proven optical quality. It therefore bypasses all challenges associated with multi-step thin-film based material synthesis and fabrication techniques.

In this thesis, the ultrafast direct laser writing (DLW) technique is applied to several materials, including fused silica, lithium tantalate ($LiTaO_3$), sapphire (Al_2O_3), and gallium lanthanum sulfide (GLS) chalcogenide glass to produce 3D photonic circuits. Optimal processing conditions are determined through the analysis of the guided-mode characteristics of these structures, while the mechanisms behind the laser-induced refractive index change are investigated with such techniques as micro-structural Raman imaging, and second-harmonic microscopy.

This research identifies optimized processing conditions by considering laser-induced multi-photon ionization, pulse distortion due to nonlinear Kerr interactions, and laser-induced thermal effects, all in connection with the intrinsic material properties. Based on this fundamental understanding of ultrafast laser material interactions, spatial and temporal pulse

femtosecond time scales with micrometer spatial resolution. This work has yielded high quality low-loss photonic circuits in chalcogenide glasses for nonlinear and mid-IR applications.

TABLE OF CONTENTS

PREFACE.....	XIII
1.0 INTRODUCTION.....	1
1.1 MOTIVAION.....	1
1.2 DISSERTATION ORGANIZATION.....	5
2.0 BACKGROUND	8
2.1 ENERGY TRANSFER	8
2.1.1 Photoionization.....	9
2.1.2 Avalanche Ionization	12
2.1.3 Relaxation and Modification.....	13
2.2 EXPOSURE VARIABLES IN GLASSES.....	16
2.2.1 Role of pulse width.....	16
2.2.2 Focusing – Linear and Nonlinear Propagation	17
2.3 EXPOSURE VARIABLES IN CRYSTALS	27
2.4 EXPERIMENTAL SETUP.....	30
2.4.1 Method for Waveguide Creation	30
2.4.2 Motion Stage and Laser System	32
2.4.3 Characterization Stage	34
3.0 POLING IN FUSED SILICA	37

4.0	FEMTOSECOND MODIFICATIONS IN CRYSTALLINE MATERIALS	50
4.1	LITHIUM TANTALATE	51
4.2	SAPPHIRE.....	68
5.0	CHALCOGENIDE GLASS	78
5.1	GALLIUM LANTHANUM SULFIDE (GLS).....	80
5.2	BRAGG WAVEGUIDES IN GLS	88
6.0	SUMMARY	101
6.1	CONCLUSION.....	101
6.2	FUTURE OUTLOOK.....	104
	BIBLIOGRAPHY	106

LIST OF FIGURES

- Figure 2.1 - Plot of the threshold intensity dependence on material bandgap for an incident pulse width of 100 fs at 800 nm wavelength. Note that the trend of increase for wider-bandgap materials is linear, and only increases by roughly a factor of two over the 3 to 5 photon bandgap range. Reprinted by permission from Macmillan Publishers Ltd: Nature Publishing Group, [Nature Photonics](#) [44], copyright 2008..... 11
- Figure 2.2 - Illustration of the various processes involved with photoionization: (a) multi-photon ionization, (b) free carrier absorption, and (c) impact ionization. Reprinted with kind permission from Springer Science and Business Media from [46], (Figure 1), [Applied Physics A: Materials Science and Processing](#). Copyright 2004. 13
- Figure 2.3 - Plot of the timescales involved with femtosecond laser-material interaction. While most of the energy is absorbed in the femtosecond time range, changes in material continue to evolve well into the microsecond range. Reprinted by permission from Macmillan Publishers Ltd: Nature Publishing Group, [Nature Photonics](#) [44], copyright 2008..... 17
- Figure 2.4 - Diagram of a laser pulse undergoing the process of self-focusing (a) and self-phase modulation (b) due to the effects of nonlinear refractive index. Reprinted with kind permission from Springer Science and Business Media from [46], (Figure 1), [Applied Physics A: Materials Science and Processing](#). Copyright 2004. 21
- Figure 2.5 - Self-focusing for a feature written in fused silica with a low NA focusing objective. The laser was incident from the bottom of the image. The bright orange spot near the lower half of the image is the original focus. Multiple foci are seen after this point as the pulse sequentially self-focuses and de-focuses. The dark areas along the line of focus are likely voids formed from the high intensity..... 24
- Figure 2.6 – Diagram of the method used for waveguide fabrication. 31

Figure 2.7 – Diagram of the ultrafast laser waveguide writing system.	32
Figure 2.8 – Diagram of the characterization system used for measurement and analysis of ultrafast laser written waveguiding structures.	36
Figure 3.1 - Illustration of the thermal poling process in silica glasses. (a) Overview of the thermal poling setup. (b) Charge migration in relation to attached electrodes and waveguide position. (c) Top and end-facet view of poled waveguides. The red arrows mark the incident writing beam direction. Reprinted with permission from Honglin An, University of Sydney.	41
Figure 3.2 - White Light microscopy images of the laser-written waveguide structures in Corning 7980 silica plates. (a) Top view and (b) side view. The line spacing is 100 μm . The writing laser was incident from left to right in (b). Reprinted with permission from [30]. Copyright 2009, American Institute of Physics	43
Figure 3.3 - Distribution of SH light in femtosecond-laser-modified Corning 7980 silica thermally poled for 70 min. (a) and (d) are ordinary transmission images, (b) and (e) are SH images, and (c) and (f) are overlay images of the corresponding ordinary transmission and SH images. Reprinted with permission from [30]. Copyright 2009, American Institute of Physics	44
Figure 3.4 - Distribution of SH light in femtosecond-laser- modified Corning 7980 silica thermally poled for 100 min. (a) and (c) are ordinary transmission images, while (b) and (d) are SH images. Reprinted with permission from [30]. Copyright 2009, American Institute of Physics	46
Figure 3.5 - Distribution of chemical elements within the femtosecond laser-modified region of soda lime glass. The inset shows an SEM image of the laser-modified region. Reprinted with permission from [30]. Copyright 2009, American Institute of Physics	48
Figure 4.1 - Optical microscope images of laser induced damage sites in lithium tantalate for pulse energies and translation speeds of (a) 1.6 μJ at 5 mm/s and (b) 300 nJ at 1 mm/s. Reprinted with permission from [31]. Copyright 2008, American Institute of Physics . ..	54

- Figure 4.2 – (a) White light image of a damage site fabricated with with 1.6 μJ pulses and a velocity of 5 mm/s. (b)-(e) Layout of various guiding regions for the damage displayed in (a). The scale bar in the image represents a distance of 15 μm . Reprinted with permission from [31]. Copyright 2008, [American Institute of Physics](#). 55
- Figure 4.3 – (a) White light image for a damage site fabricated at 300 nJ and a velocity of 1 mm/s. (b) guided mode for the damage site written displayed in (a). The scale bar in the image represents a distance of 15 μm . Reprinted with permission from [31]. Copyright 2008, [American Institute of Physics](#). 56
- Figure 4.4 - X and Y mode-field-diameters for the 300 nJ damage site depicted in Figure 4.3. Reprinted with permission from [31]. Copyright 2008, [American Institute of Physics](#). .. 57
- Figure 4.5 – Detail of the second-harmonic setup used for characterization of the poled silica samples. Reprinted with permission from Honglin An, University of Sydney. 59
- Figure 4.6 - (a) Microscope image for the laser damage site written at 300 nJ and 2 mm/s translation speed as captured with the SH microscope setup and (b) the corresponding SH image. The incident writing beam direction and polarization and propagation direction of the incident excitation laser are indicated in (a) and (b) respectively. The blue region in (b) indicates a saturation of the SH signal. Reprinted with permission from [31]. Copyright 2008, [American Institute of Physics](#). 60
- Figure 4.7 – (a) Microscope image of a damage site written at 300 nJ and a translation speed of 1 mm/s. (b) Guided mode profile of the stress-induced waveguide at 1550 nm. Note the proximity to the laser-induced damage site. (c) $x(zz)\bar{x}$ micro-Raman spectrum as obtained from the bulk (black) and waveguide (red) locations. The inset shows a magnified view of the $A_1(\text{TO4})$ mode. Reprinted with permission from [113]. Copyright 2009, [American Institute of Physics](#). 62
- Figure 4.8 – Spatial Raman maps for the $A_1(\text{TO4})$ mode, showing (a) the integrated Raman intensity, (b) Raman shift, and (c) line width of the $A_1(\text{TO4})$ mode. Reprinted with permission from [113]. Copyright 2009, [American Institute of Physics](#). 64
- Figure 4.9 – (a) optical microscope image of a laser-induced damage site written at 1 μJ and 1 mm/s translation speed. (b) Spatial map of the integrated Raman intensity for the $A_1(\text{TO4})$ mode and (c) induced shift of the same mode. Reprinted with permission from [113]. Copyright 2009, [American Institute of Physics](#). 66

Figure 4.10 - Optical microscope images of the end face of the irradiated Sapphire sample as obtained for different pulse energies and translation speeds. The black arrows visible in the top of the figure indicate the propagation direction of the UV writing pulses. Fundamental propagation modes at 632 nm for each waveguide are shown in the bottom half of the figure. Note that, for the feature written with pulse energy of 350 nJ, no waveguiding was found for the maximum translation speed. Scale bar is 20 microns. Reprinted with permission from [35]. Copyright 2009, [Optical Society of America](#)..... 70

Figure 4.11 - (a) Measured micro-luminescence spectra from the micro-structured sapphire sample, as obtained after 488 nm excitation. The R_1 and R_2 lines generated by Cr^{3+} traces are labeled. (b) Spatial dependence of the R_1 line intensity and (c) bandwidth as obtained from the laser-written feature fabricated with a pulse energy of 500 nJ and a translation speed of 0.2 mm/s. Scale bar is 20 microns. Reprinted with permission from [35]. Copyright 2009, [Optical Society of America](#) 73

Figure 4.12 - Spatial distribution of the spectral shift of the R_1 line as measured for four damage sites. The pulse energy and translation speed for each feature is labeled accordingly. The direction of the incident writing beam and waveguide location are represented by solid and dashed arrows, respectively. Reprinted with permission from [35]. Copyright 2009, [Optical Society of America](#)..... 75

Figure 5.1 – Plot of guided modes displaying the pulse width dependence of the waveguide writing process in GLS chalcogenide glass at pulse widths of 240 fs (left) and 2 ps (right). The images in (A) and (F) are representative white light images of the laser-induced damage sites, as captured with a microscope. These are given as a reference so that the guided modes may be spatially located within the feature. Reprinted with permission from [28]. Copyright 2012, [Optical Society of America](#) 81

Figure 5.2 – End facet views (top) and corresponding guided modes at 1560 nm (bottom) for waveguides fabricated in GLS chalcogenide glass using the astigmatic beam shaping technique. Left to right: (A) 2.75 ps, (B) 2.1 ps, (C) 1.5 ps, (D) 1 ps, (E) 500 fs. A minimum mode field diameter of 11.3 μm was found at the waveguide written with a pulse width of 1.5 ps. For features written at 4.5 ps and 3.75 ps, guiding was only found for a wavelength of 635 nm. These features were not visible under a standard white-light microscope. Reprinted with permission from [28]. Copyright 2012, [Optical Society of America](#)..... 83

Figure 5.3 – (top) Plot of the fringe pattern obtained for the lowest loss feature written at 1.5 ps, with a loss of 0.65 db/cm and (bottom) the mode-field diameter of all guided modes and loss vs. pulse-width. Optimal writing conditions are found for features which coincide with a pulse width of 1 – 1.5 ps. Reprinted with permission from [28]. Copyright 2012, [Optical Society of America](#)..... 84

Figure 5.4 – Spatial Raman maps indicating a reduction of Raman intensity for three waveguides written pulse widths of 1, 1.5 and 2.1 ps. The scale bar in the images represents a distance of 3 μm . Reprinted with permission from [28]. Copyright 2012, [Optical Society of America](#)..... 86

Figure 5.5 - Top view of laser written Bragg waveguides in GLS CHG glass for 25% and 50% duty cycle. First through sixth order gratings are shown with a zeroth order (no grating) waveguide shown at the top for comparison. All features were written at 300 nJ / pulse, 1 mm/s, and 1.5 ps pulse-width. The writing beam was incident into the figure, with the writing direction from right to left. 90

Figure 5.6 - End facet view of laser written Bragg waveguides in GLS CHG glass, showing approximate guided mode locations. All features were written at 300 nJ, 1 mm/s translation speed, and 1.5 ps pulse width. The writing laser was incident from the top of the figure. Features written with a duty cycle of 50% tended toward multi-mode guiding, suggesting increased thermal effects due to a higher average power incident on the glass, which is expected for picosecond regime laser writing. 93

Figure 5.7 - Grating spectra for Bragg reflectors fabricated in GLS chalcogenide glass with a fixed pulse energy of 300 nJ and 1 mm/s translation speed. The top half of the figure represents spectra obtained for features written with a duty cycle of 25%, while the bottom half represents those fabricated with a duty cycle of 50%. Both reflection (green, yellow) and transmission (blue, orange) are displayed..... 95

Figure 5.8 – Plots of the grating FWHM (top) and grating strength (bottom) versus grating order. 99

PREFACE

I would like to thank Dr. Kevin Chen for giving me the opportunity to pursue this degree, as well as to Dr. Joel Falk for his editing assistance and advice over the years. I would also like to thank Jim Lyle and Bill McGahey for their never ending and continued technical support for computers and equipment. Finally, I would like to thank Scott Topper, Scott MacPherson, Bob Barr, and Dan Lewis for their help and guidance in constructing the various apparatus that were built for the purpose of the work presented here.

1.0 INTRODUCTION

1.1 MOTIVAION

Since the initial demonstration of ultrafast-laser inscription of waveguide structures in glass by Davis *et al* [1], the research field of ultrafast laser processing has seen significant growth in the area of 3D photonic device fabrication. Using this newfound approach, researchers have found that the traditional rules and challenges associated with multi-step thin-film based material synthesis and fabrication techniques may be bypassed completely, allowing for a one-step fabrication process. Additionally, the 3D nature of ultrafast laser processing gives rise to significantly more complicated structures and devices, never before possible with a traditional planar geometry.

With respect to integrated photonic devices, the increasing trend of device miniaturization has seen rapid growth over the past 30 years. The push for miniaturization started in the 1970's with the advancements in integrated circuits and microelectronics [2], followed by the MEMS revolution [3] in the 1990 – 2000's. Recently, these ever shrinking devices have been subjected to the introduction of increasing complexity with micro- and nano-systems incorporating integrated photonics [4], bioprocessing and lab-on-chip features [5], and micro-mechanical systems [6]. Driving factors in the development of these devices are numerous:

increased efficiency, smaller footprint, fast response times, and higher resolution, just to name a few.

Fabrication of these devices has been traditionally accomplished by two main technologies. The first is based off of thin film deposition techniques, which have been adapted from the microelectronics industry. This method of fabrication requires clean room facilities and consists of sequential deposition and selective removal of precise amounts of material. Through careful selection of the material composition, deposition rate, and selective material removal via photolithographic processes and etching, increasingly complex devices are possible [7,8]. However, despite the successes of this method, several major drawbacks have also been encountered, the first being that, along with increased device complexity comes a compounding problem of material incompatibility. Any mismatch in lattice constant between one material and another leads to defects in the resulting device structure, which often limits the thickness of the deposited film and introduces defects which can affect device performance. Additionally, devices are limited to a planar geometry due to the layer-by-layer approach used for fabrication, which for the work presented here, is most prominent in the case of planar light wave circuits (PLC) [9]. The confinement of these devices to a two dimensional geometry limits scaling in both density and overall size.

The second fabrication technology is that of micro-assembly [10]. Recently, this process has seen renewed interest through the development of nanotechnology, including carbon nanotubes [11] and semiconductor nanowires [12]. More traditionally however, micro-assembly can be thought of as an extension or continuation of thin film processes, whereby more complex devices are assembled (on a micro- or nano-scale) using simpler devices derived from the thin-film processes previously mentioned. With this approach, the challenges faced are also

numerous, the most notable being the difficulty of precise alignment, bonding, and joining of the individual components.

Fabrication difficulties aside, the larger challenge faced when using either of these techniques is one of cost. The development of micro and nanotechnologies over the past three decades has not been paralleled by a reduction in size of the equipment used in the manufacturing process. These incredibly small and complex devices are produced with even more complex large-scale equipment, which must be housed in a clean-room facility. Tremendous capital investments are required to maintain these foundries, and due to an affinity toward low-cost silicon based processes, only large scale, high-yield (and silicon-based) technologies are pursued. This not only limits innovation and inhibits technologies that would otherwise flourish, but also hinders scientific advancement for the future. Additionally, the processes and foundries associated with silicon processes consume vast amounts of energy, most of which is put toward maintaining the clean room environment necessary for photolithographic processes (90 – 95% for air temperature, purity, and humidity control). These additional costs are facing more and more opposition as the awareness of reduced energy consumption and efficiency become more prevalent.

More recently, developments in solid-state laser technology have enabled generation of femtosecond duration laser pulses [13-15], allowing for a direct approach to device fabrication in bulk materials [1]. The term ‘device’ has very broad implications, though here it is taken to describe waveguides and similar waveguide based photonic devices. Due to the extremely short time duration of femtosecond laser pulses, peak intensities on the order of GW/mm^2 or even TW/mm^2 are often encountered. This direct-laser-write (DLW) approach takes advantage of nonlinear absorption processes that occur with such high intensities, enabling precise energy

deposition within a bulk substrate, an approach that has several key advantages over traditional thin film, multi-step processes.

With thin-film processes, the procedure for device fabrication may be thought of as an indirect approach. Many steps are required to reach the outcome of the process: a finished, functional device. The DLW method offers the advantage that it is truly a direct approach. Only a single step is required (as opposed to multiple deposition and etching steps) to fabricate complicated devices such as Bragg waveguide devices [16] and splitters [17,18], making it particularly attractive for such applications as rapid prototyping and small-batch runs. Additionally, the associated overhead cost with device production is also considerably lower. Devices may be fabricated in bulk substrates, which are often cheaper and of a higher purity than their thin-film counterparts. As there is no thin-film deposition or etching required, device fabrication may be performed outside of a clean-room environment. These factors also remove the need for expensive development of a photolithographic mask typically needed in traditional thin-film fabrication processes. The dramatically reduced cost of the DLW technique directly translates to faster production times with lower complexity of the device production facilities.

The femtosecond DLW approach is also highly flexible in terms of material choice and process parameters such as wavelength, pulse width, repetition rate, focusing conditions, and translation speed of the substrate. Unlike traditional thin-film processing, which requires optimized procedures for specific materials (i.e. silicon, gallium arsenide, etc..), femtosecond laser device inscription relies on nonlinear photoionization processes. When using ultrafast laser processing, index change is created through a multi-photon process [1], which directly accesses the bandgap of these transparent materials, thereby making photosensitivity a universal process across a variety of wide-bandgap transparent dielectrics [19-27].

Finally, the femtosecond DLW approach is a truly three-dimensional process. When using bulk optical substrates, waveguides or other complex optical devices may be defined at arbitrary depths using geometries that would normally be impossible with traditional thin-film techniques.

In recent years, these techniques have been applied to a variety of materials including glasses [1,23,28-30], crystalline materials [31-36], ceramics [37,38], and polymers [39]. The goal of this work is to apply these fabrication techniques and material interactions for the purpose of creating photonic devices in new materials, while gaining an understanding for the physical processes involved. The basics of waveguide fabrication have been demonstrated, utilizing a variety of writing techniques. These techniques are then applied to create complex structures such as Bragg waveguide reflectors in gallium lanthanum sulfide chalcogenide glass.

1.2 DISSERTATION ORGANIZATION

Chapter 2 contains background information necessary to give the reader a better understanding of the advantages of the direct-laser-write (DLW) technique. An overview of energy transfer from the laser pulse to the material lattice will then be given, as this process is vital to the successful creation of permanent changes in material refractive index. This is then followed by a description of the experimental processes by which these processes are applied to create structures capable of guiding light.

Chapter 3 presents the application of another fabrication technique known as poling in an attempt to introduce second-order nonlinearities into fused silica, a material that normally contains no second-order nonlinearity. The method of poling used creates a charge layer using

elevated material temperatures, which is then migrated across the sample with a high-strength electric field. The goal of this work was to overlap this charge layer (which is responsible for the introduction of higher second-order nonlinearities) with laser-written waveguides to take advantage of a stronger interaction through stronger optical confinement. These induced nonlinearities are studied using second-harmonic microscopy.

Chapter 4 takes the DLW method a step further, using an indirect approach to generate a refractive index change in crystalline materials. By creating voids in the crystal lattice, stresses are introduced into an otherwise regular crystalline structure. These stresses may either compress or dilate the bulk substrate surrounding a laser-induced void, leading to a change in refractive index. This fabrication technique is first applied to lithium tantalate, which has similar useful nonlinearities to those found in lithium niobate. The inherent second-order nonlinearities provide for greater interactions when combined with strong optical confinement, such as that present in a waveguide. The resulting guiding structures are again stress induced. The mechanism of index change was studied using micro-Raman confocal imaging by measuring the laser-damage induced shift of various vibrational modes of the substrate. Additionally, second-harmonic microscopy was used to determine the preservation of the nonlinearities within the guiding structure.

This writing technique is then extended to include pure sapphire, where magnitude of the induced refractive index change is relatively weak. Trace amounts of chromium are used in combination with micro-Raman confocal imaging as an analysis tool to investigate the origins of these refractive index changes.

Chapter 5 presents waveguide fabrication in gallium lanthanum sulfide (GLS), a highly non-linear glass. To overcome fabrication challenges associated with the high refractive index of

this material, spatial beam shaping is employed to improve the symmetry of the waveguide cross section. Further studies are presented involving temporal pulse shaping using a spatial light modulator, ultimately obtaining low-loss guiding structures. This process is then applied to the creation of multi-order Bragg reflectors in GLS.

Chapter 6 presents the conclusions and future outlook of fabrication of optical devices in transparent dielectrics using femtosecond lasers.

2.0 BACKGROUND

2.1 ENERGY TRANSFER

Structural modifications in bulk dielectrics are brought about through laser-induced optical breakdown, a process that consists of three stages: initial generation of free electron plasma, energy relaxation, and subsequent material modification. With intensities approaching 10 TW/cm^2 available from modern ultrafast laser systems, the onset of strong nonlinear absorption is easily obtained by focusing pulses from these laser systems, leading to localized energy deposition within the substrate. Energy is transferred from the laser pulse to the lattice of the receiving material [40,41], generating electron-hole plasma; a process that begins with the excitation of electrons within the dielectric lattice. Femtosecond irradiation and subsequent energy transfer generates a permanent structural modification or change in phase, resulting in a change in the refractive properties of the material. Unlike traditional processes, which rely on the presence of defect states within the substrate, ultrafast laser processing does not rely on indirect access to the material bandgap, as the energy of a single photon from an incident laser pulse is not large enough to promote electrons from the valence to the conduction band [15,42]. This non-linear process of energy transfer is the basis for ultrafast laser processing.

2.1.1 Photoionization

Laser pulses available from commercial laser systems vary in spectrum from visible to the mid-infrared ($\sim 700 - 1100$ nm) and as such, contain insufficient photon energy to be linearly absorbed in most glasses ($h\nu < E_g$). Direct exposure to high intensity laser pulses is responsible for the promotion of electrons to higher energy states through nonlinear absorption, which may occur via two mechanisms: multiphoton ionization (MPI) and tunneling ionization [41-43].

Multiphoton ionization is a process by which multiple photons are absorbed to promote an electron to a higher energy state, such that $m h\nu > E_g$, where m is the number of photons absorbed, $h\nu$ is the photon energy of the incident light, and E_g is the bandgap of the material. In this regime, the density of electrons in the conduction band (N_e) grows as:

$$\left(\frac{dN_e}{dt} \right)_{MPI} = \sigma_m I^m \quad \text{Equation 2.1}$$

where σ_m is the multiphoton absorption coefficient for the absorption of m -photons. For fused silica, with a laser wavelength of 800 nm, a typical value for m is ~ 6 , demonstrating the high intensity selectivity of this process. This process however, is only dominant at low laser intensity and high frequency.

At high laser intensity and low frequency, tunneling is the dominant ionization mechanism. The strong field present with very short pulses (< 10 fs) distorts the band structure and reduces the potential barrier between the valence and conduction band through superposition of the coulomb field of the nucleus and the electromagnetic field of the laser pulse. Electrons

may now escape their bound states via direct band transitions, which proceeds through quantum tunneling. Tunneling and multi-photon ionization are both described under theory developed by Keldysh, which describes the transition from multi-photon ionization to tunneling using the Keldysh parameter [43]:

$$\gamma = \frac{\omega(2m^* E_g)^{1/2}}{eE} \quad \text{Equation 2.2}$$

where ω is the laser frequency, m^* is the electron effective mass, E_g is the bandgap energy, and E is the laser electric field amplitude. For values of γ greater (less) than 1.5, multi-photon (tunneling) ionization dominates. For typical laser parameters and material properties, $\gamma \sim 1.5$ so that nonlinear photoionization is a combination of the two processes [42].

It is important to note however, that energy transfer from the laser pulse to the receiving material does not solely depend on non-linear ionization. If this were the case, the bandgap variation for different materials would cause an enormous variation in the required incident pulse energy (large variation in absorption probability) required for material modification. For a given material with bandgap energy $E_{gap} = N$ photons, the probability of photon absorption is given as I^N , where I is the laser intensity. It is clear that a variation in bandgap should cause a non-linear scale in required pulse energy, however this is not the case. Experiments have shown that only a slight variation in the threshold energy required for material modification is found for a wide variety of materials (Figure 2.1), which indicates that another process (in addition to MPI) is responsible. This process, which depends linearly on laser intensity, is known as avalanche ionization.

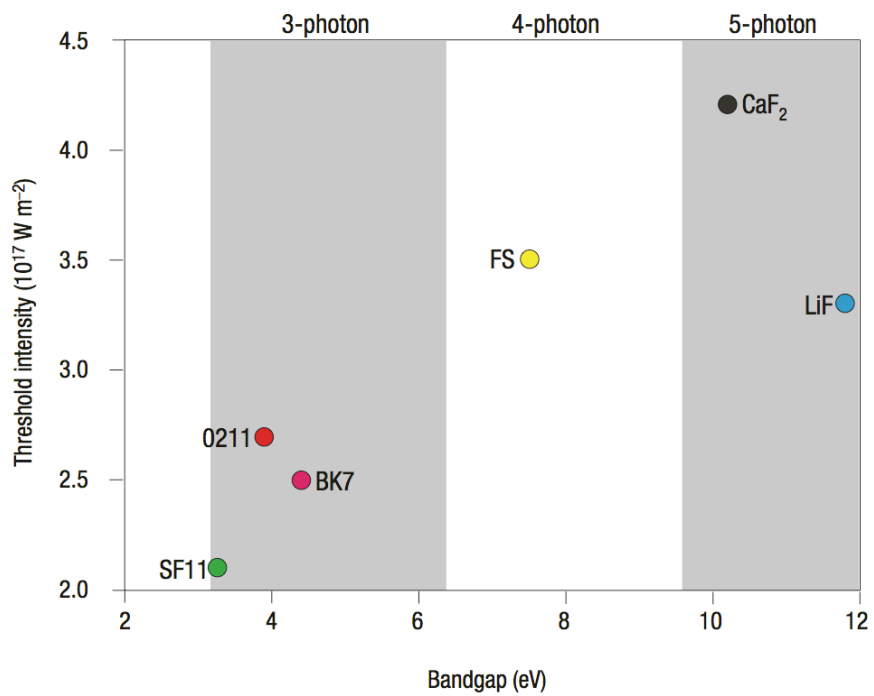


Figure 2.1 - Plot of the threshold intensity dependence on material bandgap for an incident pulse width of 100 fs at 800 nm wavelength. Note that the trend of increase for wider-bandgap materials is linear, and only increases by roughly a factor of two over the 3 to 5 photon bandgap range. Reprinted by permission from Macmillan Publishers Ltd: Nature Publishing Group, [Nature Photonics](#) [44], copyright 2008.

2.1.2 Avalanche Ionization

The process of avalanche ionization is initially seeded with excited electrons that have been promoted to the conduction band through MPI processes. Once in the conduction band, these electrons may linearly absorb additional photons in a process known as free carrier absorption (Figure 2.2(b)). When an electron in a high-energy state exceeds the conduction band minimum by more than the bandgap, it may ionize a second electron, freeing it from its bound state in the valence band, creating two electrons at the conduction band minimum [45]. This process continues until the excited electrons gain enough kinetic energy to free other electrons from their bound states via impact ionization. The combination of these two processes is known as avalanche ionization (Figure 2.2(c)) and continues as long as the driving field of the laser pulse is present. For this process, the density of electrons in the conduction band grows as:

$$\left(\frac{dN_e}{dt} \right)_{avalanche} = \alpha I N_e \quad \text{Equation 2.3}$$

where N_e is the electron density in the conduction band, I is the laser intensity, and α is the avalanche ionization coefficient. Avalanche ionization dominates over non-linear absorption and is responsible for the linear dependence of the threshold energy required for material modification.

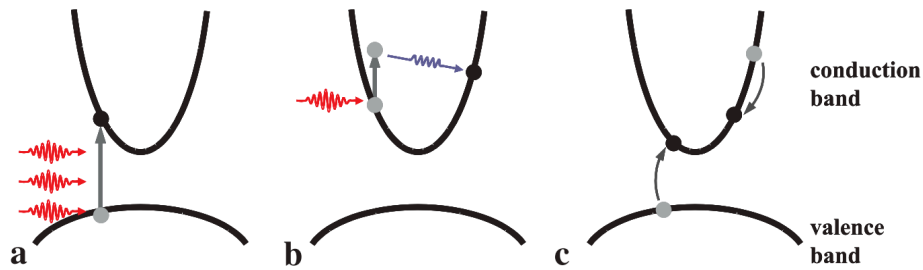


Figure 2.2 - Illustration of the various processes involved with photoionization: (a) multi-photon ionization, (b) free carrier absorption, and (c) impact ionization. Reprinted with kind permission from Springer Science and Business Media from [46], (Figure 1), [Applied Physics A: Materials Science and Processing](#). Copyright 2004.

2.1.3 Relaxation and Modification

As excited electrons return to lower energy states, they impart energy to the material lattice, which undergoes structural modification resulting in a change in the refractive index. This change can take on one of several morphological forms depending on the pulse energy delivered to the substrate, and also depends on other processing parameters (such as pulse width, focusing conditions, wavelength, etc.) as well as the properties of the substrate. These changes may be classified into three categories: a smooth refractive index change [47], a change in refractive index that displays form birefringence [48-50], and the formation of voids [51].

The generation of refractive index change requires minimum threshold energy to initiate the required absorption processes. If the incident laser pulse energy is kept close to this value,

then a localized, smooth refractive index change (Δn) will be produced within the focal volume. For the work presented here, smooth refractive index change is the most useful, as it is required for low propagation loss in guiding structures. The magnitude of induced index change varies from material to material, but is typically around 10^{-3} [24,47,52-54], which is similar to the index contrast found in standard telecom fiber. In silica glasses, this isotropic regime of index change is attributed to densification from rapid quenching of the material within the focal volume from a higher temperature [55,56]. Confirmation of this theory has been supported by Micro-Raman imaging of the laser-exposed regions, which shows an increase in 3- and 4-member rings, indicating material densification [55].

This refractive index change is often not spatially homogenous, which may be caused by a number of phenomena including material densification, a change in the fictive temperature of the material, color center formation, and residual stresses from the laser micro-machining process [22,47,53,55-58]. These effects can be drastically different for different materials and processing conditions, and in some cases may be exploited to produce guiding structures which favor strong mode confinement and low guiding losses.

Intermediate pulse energies (between threshold and void formation), have been shown to generate birefringent structures in silica glass, as first reported by Sudrie *et al.* [48]. This type of index change is known as form birefringent index change [49,59-62]. Optical confinement is still possible in these structures although it is highly dependent on the polarization of the guided light. Kazansky suggested that the so-called form birefringence is due to periodic nanostructures resulting from interference between the incident laser pulse E-field and the generated electron plasma [49], however other theories propose a mechanism of inhomogeneous dielectric breakdown leading to the formation of nanoplasma. Regardless of the formation mechanisms

involved, form birefringence has found prolific use in the area of microfluidics. The orientation of laser-induced nanogratings is dependent on the incident laser pulse polarization. When the nanogratings are aligned parallel to the laser scan direction (laser polarization perpendicular to the scan direction), preferential etching of the glass is found, since laser exposed areas of silica are more susceptible to chemical attack by hydrofluoric acid due to the difference in bond angle of the newly formed 3- and 4-member rings. Though it is not preferred for the creation of waveguides, form birefringent index change has been exploited for the fabrication of microchannels for microfluidic applications [63-66].

The choice of pulse energy is critical to creation of useful index change, since too much energy can have detrimental effects on the substrate material and leads to void formation. At moderately high levels of incident pulse energy, the area of the generated electron-hole plasma is increased, leading to a reduction in ionic shielding. After pulse energy is transferred to the lattice (~ 10 ps), the coulomb repulsion between ions [57] within the substrate generates pressures in excess of Young's modulus. A shockwave is generated, leaving behind a less dense or hollow core in the region of the focal volume. Through conservation of mass, a shell of compacted, higher index material often surrounds the lower density core [51]. For nominal waveguide performance, the formation of voids leads to an increase in scattering losses and residual stress from the disrupted material lattice. It is therefore undesirable for the fabrication of waveguides, but has found use in applications such as photonic bandgap materials [67] and 3D memory storage [68]. In order to produce a change in refractive index that is useful for the formation of waveguides, pulse energy should be chosen which is close to the threshold energy for material modification in order to avoid the various effects outlined above.

2.2 EXPOSURE VARIABLES IN GLASSES

2.2.1 Role of pulse width

The initial absorption of laser energy and subsequent ionization of bound carriers sets in motion a chain of events eventually leading up to the desired result of modified refractive index. The time scales of these processes play an important role, particularly in the choice of laser pulse-width (Figure 2.3). For sub-picosecond pulses, the energy absorption by electrons in the valence band occurs on a faster time scale than energy transfer to the material lattice, which takes place within a few picoseconds. Several nanoseconds after the arrival of the laser pulse (and long after the pulse is gone), a shockwave forms and separates from the focal volume [69-71]. Once the microsecond time scale is reached, thermal energy begins to diffuse out away from the hot focal volume, ultimately leading to non-thermal ionic motion (melting), resulting in a permanent change in the material structure [72]. The relative differences in time scale effectively decouple energy absorption from heating of the lattice.

For most transparent materials, there exists a characteristic electron-phonon scattering time (~ 1 ps), above and below which laser-material interactions differ greatly. For pulse-widths greater than this characteristic time, heat is transferred outside the focal volume generating to a heat-affected zone. This zone can lead to undesirable effects, such as residual material stress, and feature sizes that are larger than the focal volume. Mitigation of these difficulties is accomplished by choosing a pulse-width of less than 1 ps. In this case, the pulse duration is

shorter than the electron-phonon scattering time, disallowing any thermal excitation of ions outside the focal volume and leading to greater precision [73,74].

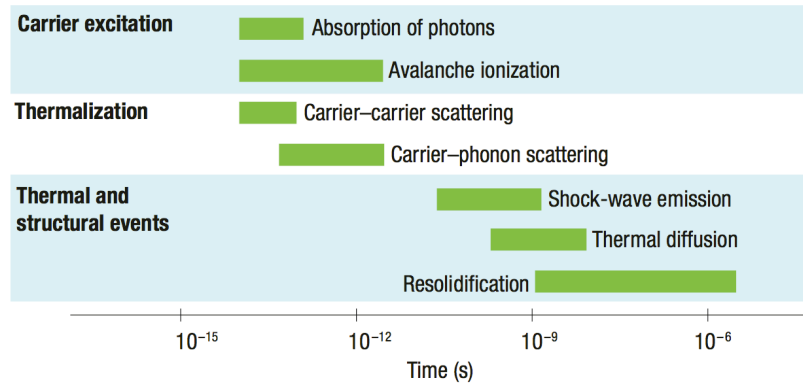


Figure 2.3 - Plot of the timescales involved with femtosecond laser-material interaction. While most of the energy is absorbed in the femtosecond time range, changes in material continue to evolve well into the microsecond range. Reprinted by permission from Macmillan Publishers Ltd: Nature Publishing Group, [Nature Photonics](#) [44], copyright 2008.

2.2.2 Focusing – Linear and Nonlinear Propagation

The promotion of electrons to higher energy states requires that an electric field be present with strength greater than or equal to the electric field that binds the valence electrons (roughly $\sim 10^9$ V/m or 5^{20} W/m²) [75]. To achieve these levels, the energy of the incident pulse can be raised significantly through stronger amplification of the laser pulse, however this leads to absorption of energy at the surface of the receiving material, which is un-desirable for the

fabrication of 3D photonic circuits. For this reason, focusing of the laser pulse using high numerical-aperture (NA) objectives is used as a means to achieve the required field strength in a controlled manner, confining material modification to the focal volume.

Experimentally, there are three parameters required for laser-induced material damage: pulse duration, pulse energy, and focusing numerical aperture (NA). Most laser systems have fundamental limits on the available minimum pulse-width and maximum pulse energy, which initially leaves the focusing numerical aperture as a variable. The effects of these three variables on the threshold intensity I^{th} required for material modification at a given wavelength λ , are expected to follow [76]:

$$I \propto \frac{E_{pulse} NA^2}{\tau_{pulse} \lambda^2 (1 - NA^2)} \quad \text{Equation 2.4}$$

where I is the laser intensity, E_{pulse} is the pulse energy, and τ_{pulse} is the pulse-width. However, this is not the case. For $\tau_{pulse} > 10$ ps, I^{th} varies as $(\tau_{pulse})^{1/2}$, indicating that joule heating of electrons excited at the beginning of the laser pulse is responsible for material damage [77]. For $\tau_{pulse} < 10$ ps only a three-fold increase in I^{th} is seen for a ten-fold increase in the laser pulse-width, τ_{pulse} . This effect is due to non-linear ionization, which creates a seed population, after which avalanche ionization (which depends linearly on laser intensity) dominates. The requirement of laser micromachining of a high density of excited electrons necessitates the use of shorter pulse-widths [41,42]. The relatively small effect of changing the laser pulse-width τ_{pulse} ultimately allows for greater flexibility in the selection of laser systems.

The researcher has some control over the size of the modified focal volume through choice of the numerical aperture of the focusing objective, as this value is based on commercially available standard objectives. The choice of objective determines the width of the focal volume (focused beam waist) and ultimately, the resulting feature size. The reader should be aware however, that certain pitfalls are present in choice of numerical aperture. Ideally, a choice should be made so as to achieve the desired feature size and index change, while avoiding nonlinear effects associated with ultrafast pulse propagation in dielectrics. These interactions cause additional distortions to the focus and change the feature size and quality in a fashion that drastically reduces the repeatability of the direct-laser-write technique [20,76,78].

When using a low-valued numerical-aperture, several processes compete with energy transfer from the laser pulse to the desired area within the substrate. The first of these is known as self-focusing, and is a result of an energy dependent distortion of the focus that occurs when the pulse energy exceeds a critical value, causing the focus to collapse to a filament, which is much smaller than the original predicted beam waist [79,80].

The large electric field associated with the high peak intensity of a laser pulse propagating through a dielectric generates microscopic displacements of the bound charges within the substrate. These displacements form oscillating electric dipoles that ultimately add up to a macroscopic polarization, which is the origin of the previously mentioned pulse distortions. For isotropic dielectrics such as fused silica, the real part of the refractive index is given by:

$$\text{Re}(n) = \sqrt{1 + \chi^{(1)} + \frac{3}{4} \chi^{(3)} E^2} \quad \text{Equation 2.5}$$

where $\chi^{(1)}$ and $\chi^{(3)}$ are the linear and nonlinear susceptibility. This can be re-written, separating the linear (n_o) and non-linear (n_2) parts of the refractive index:

$$n = n_o + n_2 I \quad \text{Equation 2.6}$$

where:

$$I = \frac{1}{2} \epsilon_o c n_o E^2 \quad n_o = \sqrt{1 + \chi^{(1)}} \quad n_2 = \frac{3\chi^{(3)}}{4\epsilon_o c n_o^2} \quad \text{Equation 2.7}$$

Nonlinear effects such as the optical Kerr effect are observed when the nonlinear refractive index (n_2) is non-zero.

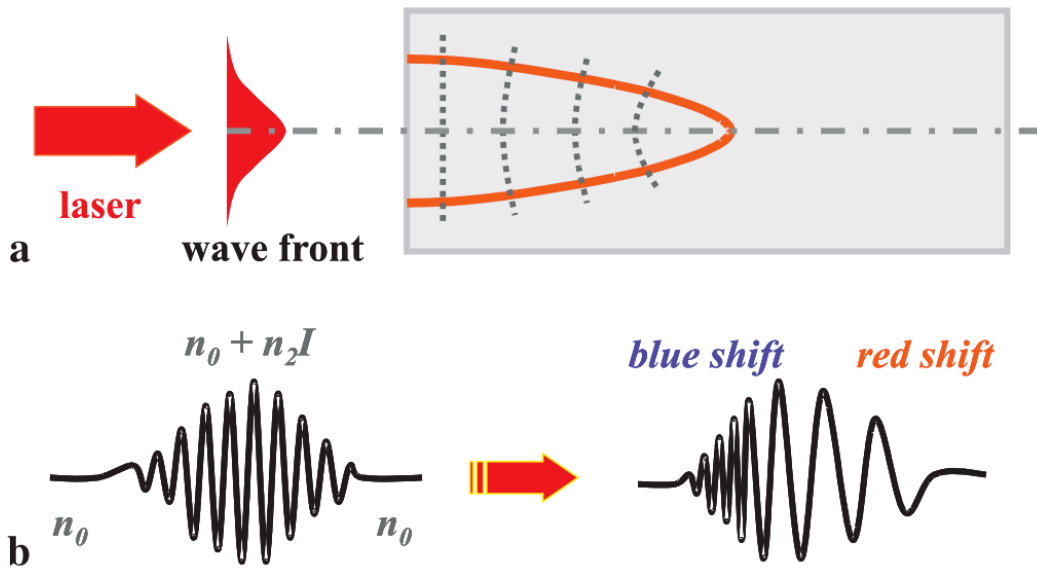


Figure 2.4 - Diagram of a laser pulse undergoing the process of self-focusing (a) and self-phase modulation (b) due to the effects of nonlinear refractive index. Reprinted with kind permission from Springer Science and Business Media from [46], (Figure 1), [Applied Physics A: Materials Science and Processing](#). Copyright 2004.

A typical laser beam has a Gaussian intensity profile, with the highest intensity at the center. Taking into consideration the above equation for the refractive index with a non-linear component, it can be easily shown that the refractive index at the center of the beam (point of highest intensity) will also be larger than at the edges. This spatial variation in refractive index leads to a lens-like effect (Figure 2.4 (a)), causing further focusing of the propagating laser pulse, though only for powers exceeding a critical value, given by [81,82]:

$$P_{cr} = \frac{3.77\lambda^2}{8\pi n_0 n_2} \quad \text{Equation 2.8}$$

When $P > P_{cr}$, collapse of the laser pulse to a singularity is predicted. This effect however, is balanced by another non-linear phenomena known as plasma defocusing. This effect is generated in much the same manner as the Kerr nonlinearities. A propagating laser pulse generates electron-hole plasma (in addition to modifying the local refractive index), which acts to defocus the beam. In this case, the real part of the refractive index is given by:

$$n = n_o - \frac{N}{2n_o N_c} \quad \text{for} \quad \omega_p / \omega \ll n_o \quad \text{Equation 2.9}$$

where:

$$N_c = \frac{\omega^2 \epsilon_o m^*}{e^2} \quad \text{Equation 2.10}$$

is the characteristic plasma density for which the plasma frequency ω_p is equal to the driving laser frequency, ω . N_c is the population density of excited electrons in the conduction band. This has the opposite effect of Kerr self-focusing, since the peak intensity at the center of the beam will reduce the refractive index due to the generation of electron-hole plasma. These two effects act together, producing further spatial inhomogeneity in the induced refractive index modification of the substrate. With these two effects combined, we have:

$$n = \left[n_o - \frac{N}{2n_o N_c} \right] + n_2 I \quad \text{Equation 2.11}$$

Depending on the focusing conditions and incident pulse energy, the effects can balance (as in the case of soliton generation) [83], or behave in an oscillatory fashion (Figure 2.5).

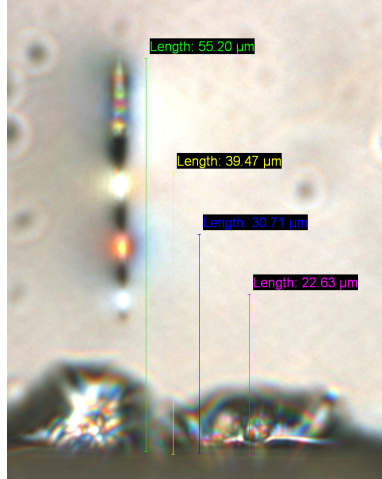


Figure 2.5 - Self-focusing for a feature written in fused silica with a low NA focusing objective. The laser was incident from the bottom of the image. The bright orange spot near the lower half of the image is the original focus. Multiple foci are seen after this point as the pulse sequentially self-focuses and de-focuses. The dark areas along the line of focus are likely voids formed from the high intensity.

Spectral broadening is a process similar to the Kerr effect, which operates in the time domain. The highly time dependent nature of the intensity of ultrafast pulses produces a time dependent variation in refractive index. This leads to a modulation in phase of the propagating pulse brought about by the time-domain envelope of the pulse itself. Taking the derivative of the pulse phase $\phi(z, t)$ with respect to time and assuming a non-zero refractive index yields [81]:

$$\frac{\partial \phi}{\partial t} = \omega - \frac{n_2 z}{c} \frac{\partial I(t)}{\partial t} \quad \text{Equation 2.12}$$

Frequency shifts are produced from the time-varying term of the phase, ultimately broadening the pulse spectrum, as shown in Figure 2.4(b). The amount of broadening depends on the nonlinear refractive index n_2 as well as the time derivative of the pulse intensity. Spectral broadening may be both desired as well as an un-desired effect. It is often exploited to produce extremely broadband sources in a process generally known as white light generation [84].

When considered with other effects such as material dispersion, spectral broadening can lead to a broadening of the propagating laser pulse and a reduction in the overall peak intensity. Material dispersion is a property of transparent dielectrics that dictates the velocity of light based on the variation of refractive index with wavelength, $n(\lambda)$. Ultrafast pulses are generated from a broad spectrum, often spanning 10 nm or more about a central wavelength, λ . The individual components of this pulse spectrum ('red' and 'blue') will ultimately travel at different velocities, spreading the pulse in time. Taking the derivative of this wavelength dependence $\frac{\partial n(\lambda)}{\partial \lambda}$, gives the group velocity, or the velocity of the envelope of the wave packet with central wavelength λ , which describes the velocity of the pulse as a whole. Taking the second derivative $\frac{\partial^2 n(\lambda)}{\partial \lambda^2}$ gives the group velocity dispersion (GVD), or the rate at which the individual wavelength components of the pulse spread. A spread in the pulse will ultimately reduce the peak intensity, leading to a reduced change in refractive index within the receiving material. This issue is further compounded when combined with self-phase modulation, which causes further spectral broadening to an already broad spectrum under normal dispersion conditions. As more wavelength components are generated, more dispersion is experienced, causing further temporal broadening and reduction of the peak pulse intensity.

Though effects of self-phase modulation and material dispersion should be considered, it should be noted that for a typical Yb-based amplified femtosecond laser (1 μm wavelength, 10 nm bandwidth), the material dispersion in glass is -50 ps/km/nm , giving a pulse duration increase of 5 fs/cm . As these sources often have pulse widths of $\sim 200 \text{ fs}$, material dispersion from glass in the optical system is negligible. It is only for femtosecond systems with extremely short pulse widths ($\sim 20 \text{ fs}$) that material dispersion becomes a problem [85].

The aforementioned non-linear effects are a constant concern, however the choice of a higher-valued NA can mitigate these fabrication challenges. It is vitally important to note that the value of the numerical aperture has a high degree of impact on the cross-sectional symmetry of the final laser-written features. Above an NA of ~ 0.6 , this cross-section is roughly symmetric (for ‘standard’ index materials where n is in the range of ~ 1.5 such as fused silica). For lower NA values, the features become elongated and highly a-symmetric. In this case, spatial beam correction is required to correct this asymmetry [16,86]. For values of $\text{NA} > 1$, laser pulses from a femtosecond oscillator may be used, taking advantage of the high repetition rate (usually in the tens of megahertz). In this regime, energy transfer builds up at the focus (the period of the repetition rate is much smaller than the heat diffusion time of $\sim 1 \mu\text{s}$) and eventually diffuses out as heat [87,88]. This method has the added advantage of increased processing times, and can create features larger than the original focus [87]. Additionally, the choice of NA sets the threshold energy required for material modification, while the number of incident pulses sets the final feature size.

2.3 EXPOSURE VARIABLES IN CRYSTALS

Crystalline materials offer many unique properties including even order nonlinearities, birefringence, and broad transmission ranges. In these materials, the origins of refractive index change differ greatly from that of their amorphous glass counterparts. As was discussed previously, irradiation of silica glasses results in a re-arrangement of the material lattice, leading to compaction and an increase of the refractive index [55,89]. In crystalline media however, disruption of the regular material lattice results in a reduction of the material density and a subsequent reduction in refractive index. In general, the morphological changes resulting after femtosecond irradiation of crystalline materials may be classified into one of two categories. So-called Type I structural changes classified by a melting of the focal volume and, in some cases, a change in stoichiometry. Type II changes are classified by a complete destruction of the material lattice leading to induced stress from expansion of the focal volume.

The mechanisms behind Type I modifications involve a similar re-orientation of the material lattice as seen in the case of amorphous materials, but the outcome is entirely different due to the regular structure of the crystal. This regime of morphological change is characterized by a melting of the focal volume, which leaves behind an amorphous core, as first observed for femtosecond-modified α -quartz [33]. This change from crystalline to amorphous structure has the effect of reducing the refractive index as well as the density of the material within the focal volume. Induced stresses from expansion of the focal volume give rise to symmetrical index change on either side of the damage region, which has been found to be capable of guiding light. [33] Similar results have been found in lithium niobate ($LiNbO_3$) [90,91] at pulse energies just above the modification threshold. In this case however, an increase in the extra-ordinary

refractive index (n_e) is found and sufficient index change is found in the laser-fabricated structures to confine a guided mode. Several mechanisms have been proposed for there resulting increase in refractive index including a change in stoichiometry after thermal diffusion of ions during fabrication, movement of free charges due to the photorefractive effect, and defect generation in the laser-modified lattice [90]. Furthermore, the nonlinear properties of the material are reduced in the irradiated regions of the substrate. As the incident pulse energy is increased, the morphology of the laser-induced structures changes dramatically.

At higher pulse energies, Type II structures are generated, which are characterized by a severe reduction of material density (i.e. complete destruction of the lattice) in the focal volume accompanied by a reduction of both the ordinary and extraordinary refractive indices. Due to the severe damage imparted to the material, these structures are not suitable for guiding light. The expansion of the focal volume however, as suggested by Gorelik *et al.* [33], is responsible for an induced stress field, which manifests itself as a symmetrical change in refractive index to either side of the damage site. Waveguides have been fabricated using a modified form of this technique (the so-called ‘double-track’ technique) whereby two damage tracks are written with spacing such that the mode field of the stress distributions of each track overlap, creating a well defined waveguide [38,92,93].

Pulse duration in crystals has a strong impact on modification due to depletion from absorption for shorter ($\sim 50 - 100$ fs) pulses, which is of particular concern in crystals with large nonlinearities such as lithium niobate [32] and lithium tantalate [31]. Focal distortion is also a concern as the same nonlinearities that contribute to energy depletion also lead to filamentation from self-focusing of the laser pulses. This distortion is further complicated by index mismatch induced spherical aberrations. To mitigate the effects of inherent material nonlinearities and to

enable better control over the size of the modified region, longer pulse-widths of up to ~ 1 ps have been reported [32]. Studies have shown that pulses delivered to the lattice with duration of 50 fs have little effect on material modification, despite having high peak intensity. Conversely, 500 fs pulses are shown to have more effect on the material. Absorption from the 50 fs pulse is 2x larger than the 500 fs pulse due to the energy being absorbed over a larger area, despite a peak fluence 6x higher for the 500 fs pulse than the 50 fs pulse [32].

Now that the framework for understanding the mechanisms behind energy transfer and index modification have been laid, the techniques and equipment for applying these phenomena to produce guiding structures will be covered.

2.4 EXPERIMENTAL SETUP

2.4.1 Method for Waveguide Creation

At the experimental level, the fabrication of waveguides using an ultrafast laser is a mechanically simple process, which is accomplished by translating the beam focus through the sample at a fixed velocity. This allows the researcher an additional control parameter, which is the velocity at which the beam focus is moved through the writing substrate. All of the waveguides studied in this work were fabricated in a similar manner, which is laid out in Figure 2.6.

The basics of a standard laser fabrication setup consist of a (A) beam path for the writing laser beam, (B) a focusing objective, (C) a suitable substrate, and a motion stage (not shown) with which to translate the beam focus through the material. For the work that will be discussed here, the sample was mounted to a motion stage while the objective was kept in a fixed position. Movement of the writing objective is possible, however the complications involved with the design of a free-space beam delivery system make its implementation impractical.

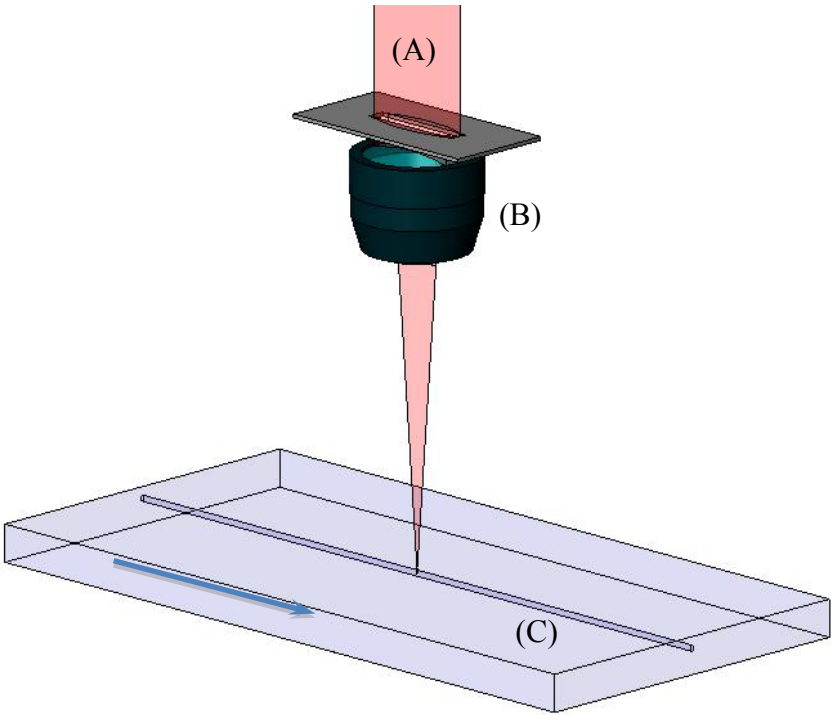


Figure 2.6 – Diagram of the method used for waveguide fabrication.

2.4.2 Motion Stage and Laser System

The writing setup used in this work is based around a laser oscillator and a regenerative amplifier manufactured by Coherent, Inc., which is displayed in Figure 2.7. The oscillator (labeled ‘Mira 900’ in the figure) produces ~ 120 fs pulses at a repetition rate of 76 MHz. A small portion of the output beam from the Mira is fed to the regenerative amplifier (labeled ‘RegA 9000’ in the figure) for further amplification.

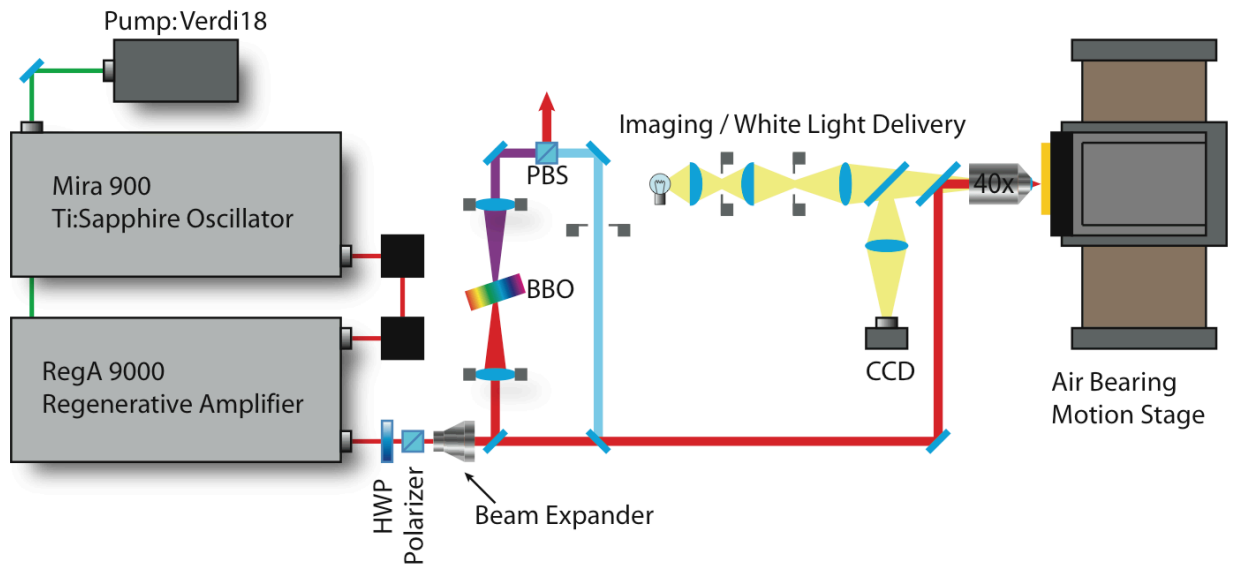


Figure 2.7 – Diagram of the ultrafast laser waveguide writing system.

This system boosts the pulses to have an average output power of 1.2W ($\sim 4.8 \mu\text{J} / \text{pulse}$) at a repetition rate of 250 kHz. The pulses from the RegA then follow a beam path that allows for attenuation of the power using a combination of a rotating half-wave-plate (HWP) and fixed cube polarizer. From this point, the beam may be used directly or passed to a second stage that doubles the beam frequency (second-harmonic generation) using a nonlinear beta-barium-borate (BBO) crystal. This process produces a shorter wavelength for the writing process, since it has been reported that some materials respond better to shorter wavelengths during processing [38]. The beam is then directed through a confocal microscope, which images the sample during waveguide fabrication and allows for easier sample alignment during setup. The beam then passes through the writing objective where it meets the sample in which waveguides are to be written. This sample is mounted to a 3-axis motion stage manufactured by Aerotech, Inc. and has a repeatability of 50 nm.

2.4.3 Characterization Stage

After fabrication, a waveguide sample is then prepared for characterization of the guiding features to determine losses and overall mode size of the fabricated structures. The edges of the sample are first ground and polished to give a high-grade surface quality so as to avoid any unwanted losses from defects, and scratches, as well as ensure that the waveguide end-facet and the sample end-facet coincide. This setup can be seen in Figure 2.8.

After polishing, the sample is mounted to a station using a vacuum assisted hold down device. An optical switch provides a variety of diode laser sources at both the visible (635 nm) and telecom (1550/1560) wavelength ranges. This laser light is delivered to a silicon v-groove, which contains an optical fiber that has been cleaved and polished. This v-groove assembly is mounted to a 3-axis motion stage, so that the output facet of the fiber may be butt-coupled to the end facet of the waveguides that are to be interrogated. An imaging system is placed opposite the fiber v-groove assembly, on the opposite side of the sample, and is used to image the output facets of the laser-written waveguides. This imaging system has several purposes, the first of which is to aid in initial coupling of the laser-written waveguides using visible laser light (635 nm) in combination with a visible CCD camera. Afterward, the wavelength may be switched to IR (1550/1560 nm) and the guided mode profile of the features can be viewed and captured using an IR CCD. Additionally, this setup may also be used for loss measurements. A turning mirror is placed in the beam path, just after the imaging objective, which directs the out-coupled laser light to a power detector. Various other components (not shown for simplicity) also aid in sample

alignment, such as an overhead CCD camera. Finally, components may be added to the system by connecting an auxiliary fiber to the optical switch.

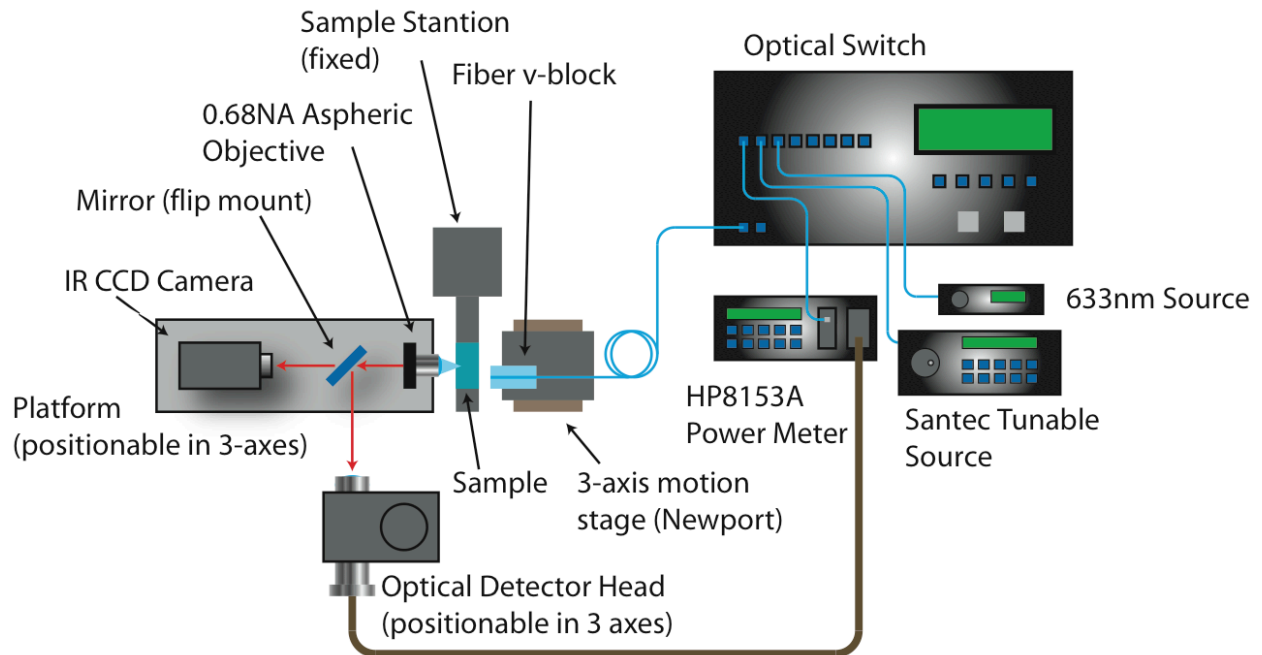


Figure 2.8 – Diagram of the characterization system used for measurement and analysis of ultrafast laser written waveguiding structures.

3.0 POLING IN FUSED SILICA

In collaboration with:

Simon Fleming and Honglin An
Second-harmonic microscopy studies
University of Sydney

Silica glass is an important material for optical applications as it exhibits excellent properties such as a broad transmission window with low loss and high mechanical strength. These properties have enabled silica to be the most widely used material in telecom applications, where it is easily drawn into fibers for carrying light. In such an industry as telecom, signal switching is often required for routing signals among different fibers, a process which relies on materials with nonlinearities. As silica is a centrosymmetric system, it inherently contains no even-order nonlinearities and hence has no role in active switching or routing.

Thermal poling is a process that allows for the enhancement of nonlinearities in silica glass through modification of inherent charges in the lattice, and has been widely used for inducing optical nonlinearities in this amorphous material for some time [94]. The poling process relies on the creation of mobile charges through promotion to higher energy levels (and in this case is done thermally), which are then preferentially drifted through the glass by applying a strong electric field. With the field still applied, the sample is allowed to cool, trapping the migrated charges in place thereby creating a region of space charge and hence a ‘frozen in’ electric field

[87,95,96], This chapter will discuss the basics of thermal poling as well as its application to femtosecond laser written waveguides in silica glass.

Optical nonlinearities are generally described in terms of the material susceptibility (χ) according to the following polynomial expansion:

$$P = \varepsilon_0(\chi^{(1)}E + \chi^{(2)}E^2 + \chi^{(3)}E^3 + \dots) \quad \text{Equation 3.1}$$

where P is the dielectric polarization in terms of a polynomial expansion of the susceptibility, E electric field, and ε_0 the vacuum permittivity. χ is a complex quantity where the real part represents the delay and is directly related to the refractive index n as was discussed previously, while the imaginary part describes the loss or gain experienced by propagating light. In the above expansion, $\chi^{(1)}$ is directly related to the refractive index. $\chi^{(2)}$ is of the most interest to poling, since it describes how the refractive index varies linearly with applied electric field and $\chi^{(3)}$, as will be shown shortly, is directly responsible for the generation of $\chi^{(2)}$ in silica glasses. The electric field E may be separated into two parts to describe an applied E -field, E_{appl} , and the E -field of the propagating light, $E_1(\omega)$, as follows:

$$E = E_{appl} + E_1(\omega) \quad \text{Equation 3.2}$$

Substituting this into Equation 3.1 taking relevant terms and ignoring third order susceptibility and above gives:

$$P(\omega) = \varepsilon_o \left(\chi^{(1)} + 2\chi^{(2)}E_{appl} \right) E_1(\omega) \quad \text{Equation 3.3}$$

This is the basis for electro-optic switching, however it is important to remember that, in silica glass (a centrosymmetric system), there exists no second order susceptibility, therefore the process outlined in Equation 3.3 is not possible in these materials.

The process of poling however, allows for the creation of a second order nonlinearity through the interactions of a so-called frozen-in E -field with the third order susceptibility, according to:

$$\chi^{(2)} = 3\chi^{(3)}E_{frozen} \quad \text{Equation 3.4}$$

This process is based on a charge separation model [97], which relies on the presence of inherent charges in silica glass (alkali ions) that are immobile at room temperature. These ions are located near defect sites that provide an opposing charge, keeping the ions trapped. When heated to a certain temperature (~ 300 °C for silica), the charges become excited and can move through the glass matrix. The application of a large external electric field preferentially migrates the charges toward the electrode of opposite charge. Allowing the sample to cool to room temperature while keeping the applied field in place re-traps the charges in their new (migrated) location. The resulting space-charge field from concentrated charge generates an electric field, known as the

‘frozen-in’ field. It is this field which acts on the third order nonlinearity to generate a second order nonlinearity [97]. A diagram of this process may be seen in

Figure 3.1(a, b). It is believed that the ions responsible for the most migration are sodium (Na^+), though it is widely accepted that other, less-mobile species such as H^+ and H_3O^+ also contribute to this space charge region [96] (Figure 3.1(b)).

If the poled region of the glass can be successfully overlapped with femtosecond laser written waveguides, a low-cost and easy-to-produce device will be realized (See Figure 3.1(a)). Second-harmonic (SH) generation has already been demonstrated in poled optical fibers and planar waveguides [98,99], and electro-optic (EO) switches and modulators based on thermally poled planar waveguides and fibers have also been demonstrated and tested in real transmission systems [100-102]. Based on this information, it should be possible to combine the techniques of thermal poling and DLW waveguides to produce a low-cost switching device in silica glass

Thermal poling of a silica glass pre-modified by femtosecond laser irradiation was first reported in 2002, with an increase in SON being found in the structurally modified glass region [100-102]. Recently, an EO waveguide modulator fabricated in fused silica by a combination of femtosecond laser direct writing and thermal poling has been demonstrated with an estimated effective EO coefficient of 0.17 pm/V for the TE mode [103]. Apart from these two, relevant reports are still scarce. This work presents the results of a study to characterize the SON in thermally poled fused silica, which was successfully overlapped with laser-written guiding structures. Direct visualization of the SON distribution reveals a substantially different behavior from the previously reported results.

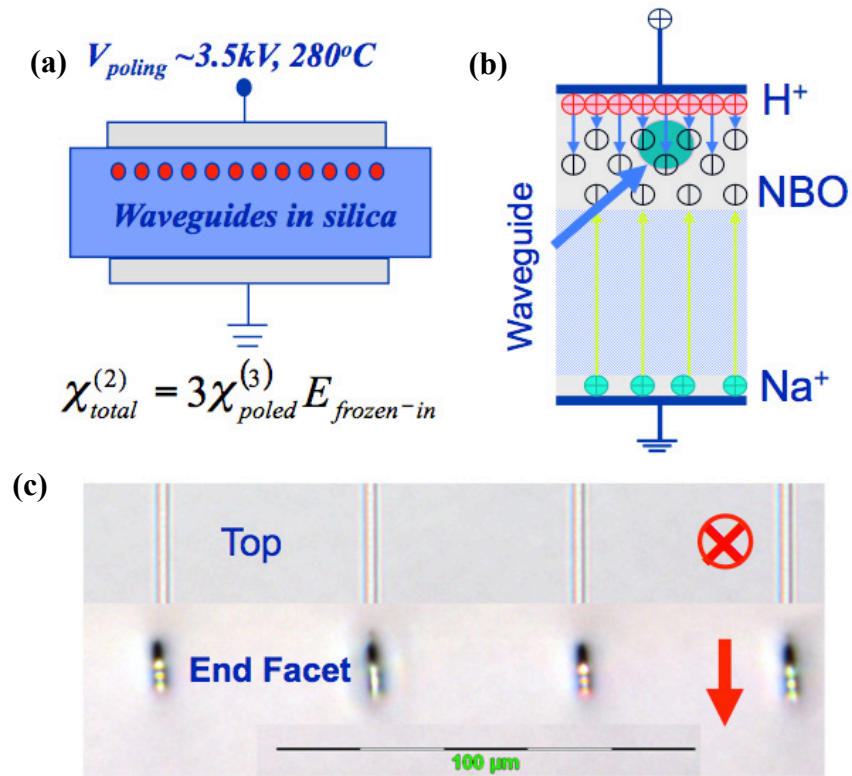


Figure 3.1 - Illustration of the thermal poling process in silica glasses. (a) Overview of the thermal poling setup. (b) Charge migration in relation to attached electrodes and waveguide position. (c) Top and end-facet view of poled waveguides. The red arrows mark the incident writing beam direction. Reprinted with permission from Honglin An, University of Sydney.

The glass samples used in this experiment were plates of a synthetic flame-fused silica (Corning 7980). Parallel lines of waveguides were written in the bulk of the silica substrate by scanning with a focused beam from the fabrication system discussed in Section 2.4.2, which was configured to provide 400 nm pulses and a variable repetition rate of 250 – 500 kHz. The pulse energy ranged from 160 to 300 nJ/pulse and the scanning speed varied from 50 to 500 $\mu\text{m/s}$. All waveguides were written in a plane parallel to the surface of the silica plate, with a depth of 12 – 25 μm beneath the surface. For features with a depth of greater than 15 μm , hydrofluoric acid (HF) etching was used to thin the plates until the waveguides were at least 15 μm beneath the surface. This distance ensures an effective overlap between the laser-written structures and the thermal-poling-induced nonlinear region. Typical white-light optical microscopy images of these structures are shown in Figure 3.2. The upper and lower waveguides are written with 240 nJ pulses at 250 kHz with scanning speeds of 100 and 75 $\mu\text{m/s}$, respectively. In this figure, the end-facet image clearly indicates that waveguiding structures have been successfully fabricated in the silica plate, however the dark region behind the light-guiding region shows evidence of voids in the material, most likely caused by microexplosions [57]. Thermal poling was carried out in air with pressed-on electrodes, a poling voltage of 3.5 kV, and a substrate temperature of 280 $^{\circ}\text{C}$ for 70–100 min. The exact poling duration was determined by the depth of the laser-written waveguides beneath the surface of silica plates. After poling, the spatial profile of the SON was investigated by directly visualizing the distribution of the generated SH signals from the poled samples using SH microscopy, as described elsewhere [104].

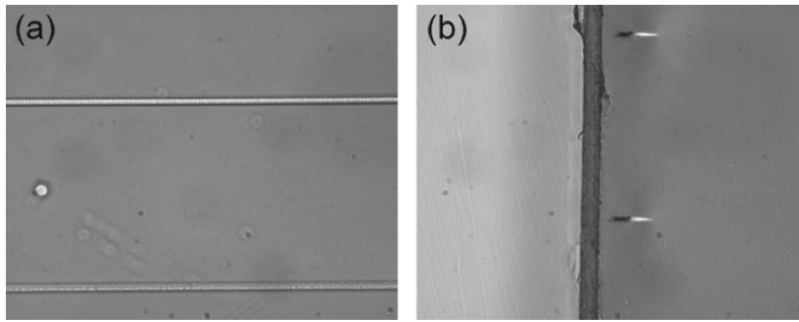


Figure 3.2 - White Light microscopy images of the laser-written waveguide structures in Corning 7980 silica plates. (a) Top view and (b) side view. The line spacing is 100 μm . The writing laser was incident from left to right in (b). Reprinted with permission from [30]. Copyright 2009, [American Institute of Physics](#).

To prepare the poled samples for microscopy studies, a microscope cover slip was attached to the anode side of the poled silica plates, providing support and protection during grinding and polishing of the sample end facets. The sample assembly was then cleaved in half to expose two cross sections parallel to the applied poling field, which were also polished to a high optical grade in preparation for SH microscopy studies. The samples were rotated for the SH measurement so that the polarization direction of the fundamental laser beam was parallel to the poling direction in order to utilize the larger nonlinearity component d_{33} [97]. The transverse spatial resolution of the SH microscopy is estimated to be 0.4 μm .

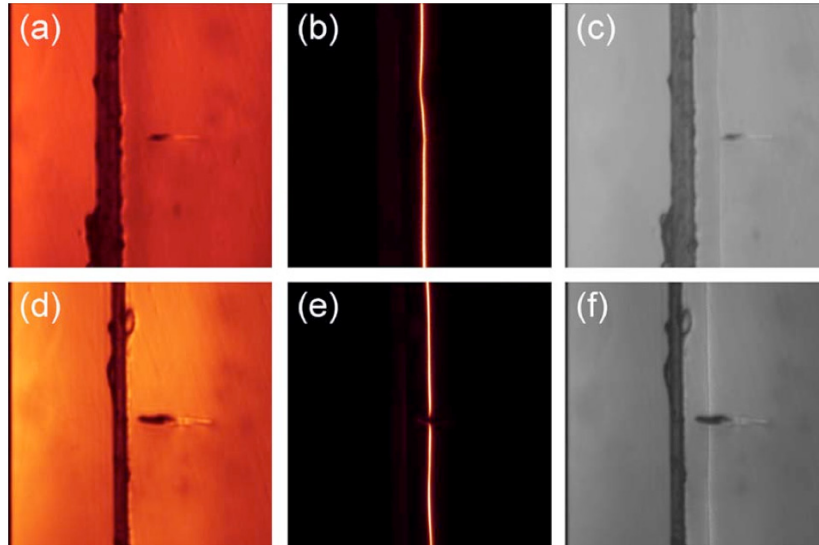


Figure 3.3 - Distribution of SH light in femtosecond-laser-modified Corning 7980 silica thermally poled for 70 min. (a) and (d) are ordinary transmission images, (b) and (e) are SH images, and (c) and (f) are overlay images of the corresponding ordinary transmission and SH images. Reprinted with permission from [30]. Copyright 2009, [American Institute of Physics](#).

Typical SH micrographs of the silica plates poled for 70 min are shown in Figure 3.3. The waveguide structure in Figure 3.3(a - c) is written with 160 nJ pulses at 250 kHz and 150 $\mu\text{m} / \text{s}$, while that in Figure 3.3(d - f) is written with 160 nJ pulses at 500 kHz and 100 $\mu\text{m}/\text{s}$. In all the poled plates, it was found that the induced SON was localized in a narrow layer approximately 9.4 μm beneath the anode surface. As shown in Figure 3.3(a), the SON layer did not reach the laser-modified region, and is continuous and uniform in signal strength, as observed in prior work [57]. In Figure 3.3(d), the laser-modified region was closer to the surface, and the SON layer now intersects the dark part of the modified region. Where the original SON layer was

continuous, it is now broken into two sections, with no SH signal found in the modified region. Presumably this is due to the micro-explosion induced structural irregularities [104], which, due to voids in the material, prohibit the migration of the SON layer through this region. For all samples poled for 70 min, the SON layer did not reach the waveguiding region. The SON magnitude, $d_{33} \sim 0.07 - 0.1$ pm/V, is also lower than that in fused quartz silica.

To enable better overlap the nonlinear region with the laser-written waveguides, a longer poling duration of 100 min was chosen. Before poling, some silica plates were cut into two half-sections, one of which had an additional processing step. As alkali ions are known to play an important role in poling, it was suspected that their scarcity in the synthetic Corning 7980 silica might be responsible for the smaller SON achieved. For this reason, one-half of each plate was first annealed in air at 600 °C for 4h in an attempt to introduce and redistribute alkali ions to the annealed plates, after which both halves were identically poled. Typical SH micrographs from the polished cross sections of these samples are shown in Figure 3.4. In all images, the annealed and un-annealed halves of the same sample are affixed back to back with the un-annealed to the left and the annealed section to the right.

By measuring the positions of the waveguides and SON layers, it is clear that the SON layer has now reached the waveguides in both samples, being 3.1 μm into the un-annealed waveguide and 2.7 μm into the annealed waveguide. The SON layer is weaker in the waveguiding regions than that outside the laser-modified region in both samples, as evidenced by a measurement of d_{33} within the waveguide, which was measured to be at least 1.9 times lower than that found in the bulk substrate. It was also found that the SON layer around the waveguides seems to lag behind than SON found farther away from the laser-modified region, indicating decreased ion mobility in this region.

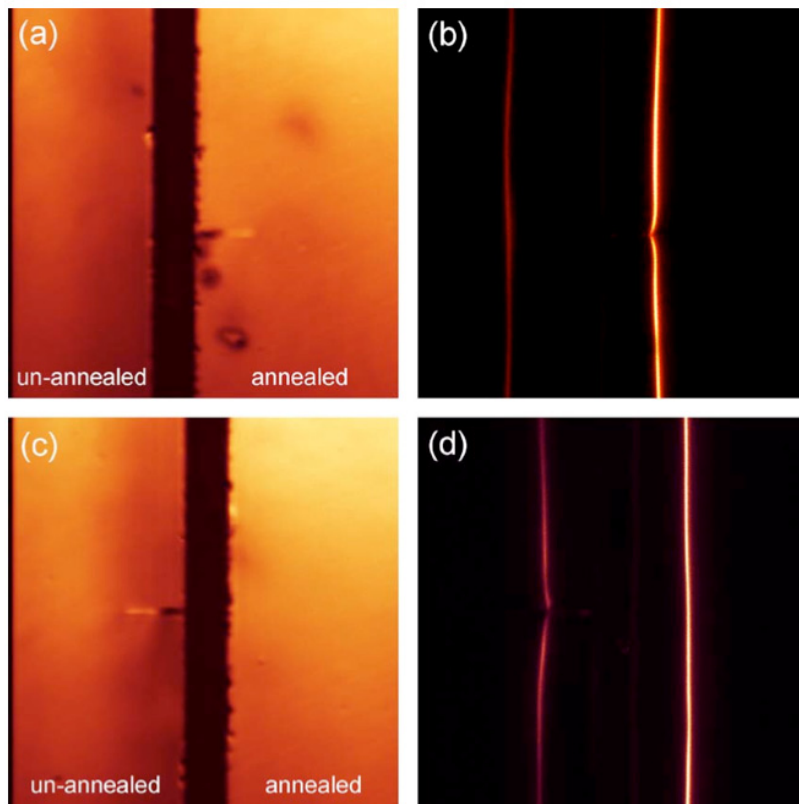


Figure 3.4 - Distribution of SH light in femtosecond-laser- modified Corning 7980 silica thermally poled for 100 min. (a) and (c) are ordinary transmission images, while (b) and (d) are SH images. Reprinted with permission from [30]. Copyright 2009, [American Institute of Physics](#).

This is perhaps a result of the glass network becoming denser due to laser irradiation. The SON layers well away from the laser-modified region are all straight and uniform in intensity. It is also interesting to note the SH signal layer in the annealed samples is much brighter than that in the un-annealed samples. In this case, the ratio of $d\beta$ in the two samples was estimated to be in the range of 1.6 – 2.5. This increase is attributed to a higher concentration of mobile alkali ions in the annealed sample, with surface contamination due to handling as the primary source.

These findings are in contrast to the previously published results [105], where an enhancement of the SON layer was found in the laser-modified region. However, a direct comparison cannot be made as the silica types and femtosecond laser irradiation conditions are different for both cases. The weaker SON layer found in the laser-modified region is tentatively attributed to compaction of the glass network. As the femtosecond-laser-written waveguide is a direct result of the denser glass structure, lower mobility for alkali ions and other charges within this densified glass region is expected, making it more difficult for ions to either enter or exit this modified region and form the frozen-in space-charge field [95,96,106]. The net result is a weak space-charge field and a corresponding weak SON. Additionally, the resulting densified silica network could also be accompanied by a further reduction in alkali ion density in the laser-modified region. To test this hypothesis, a soda lime glass was chosen, and the distribution of alkali ions in a modified region written by a Spitfire Ti:Sapphire laser (800 nm wavelength, 1 kHz repetition rate, 120 fs pulse duration, 1.2 J pulse energy, 50 $\mu\text{m/s}$ scanning speed, and 0.25NA focusing objective) was measured with an energy dispersive x-ray spectrometry (EDS).

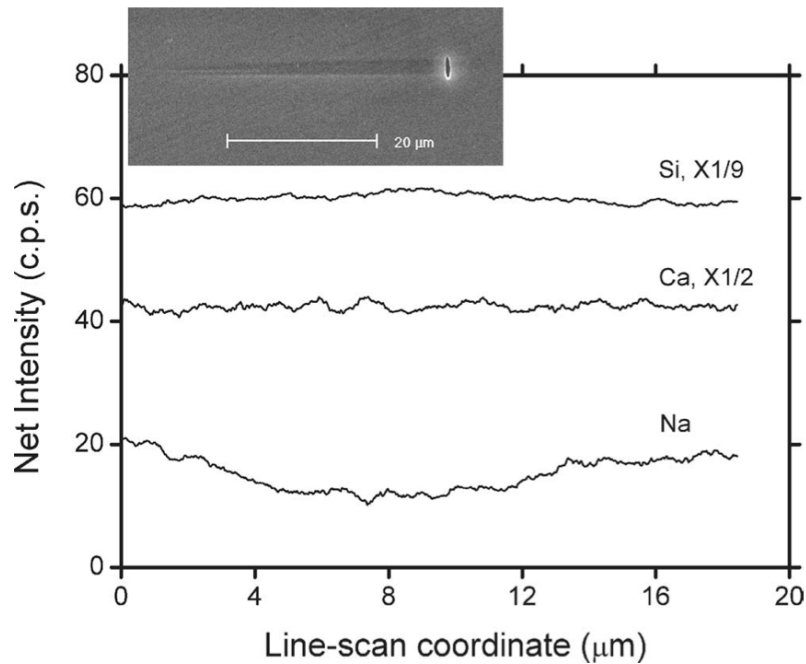


Figure 3.5 - Distribution of chemical elements within the femtosecond laser-modified region of soda lime glass. The inset shows an SEM image of the laser-modified region. Reprinted with permission from [30]. Copyright 2009, [American Institute of Physics](#).

This technique was not attempted on the fused silica samples, since the level of alkali ions found in this substrate is beyond the limit of the EDS technique. The result from a line scan across the laser-modified region is shown in Figure 3.5. To better enable identification of the laser-modified regions under a scanning electron microscope (SEM), the polished surface was etched in diluted hydrofluoric acid to give a small amount of surface relief. In this plot *Si* is shown as a reference. It is clear that the concentration of Na^+ decreased in the laser-modified region, while *Ca* stays almost unchanged. Similar results have been reported in a *PbS*-doped silicate glass irradiated with femtosecond laser pulses [107], which provides indirect support for

the hypothesis of a lower level of Na^+ in the laser-modified region found in fused silica. Further experiments are needed to fully resolve this issue.

For the work presented in this section, it is clear that the introduction of optical nonlinearities into silica glasses presents a challenge, particularly when combined with ultrafast laser fabrication of waveguides. Though the mechanisms of ion transport that contribute to the induced space charge region are well understood, the problem of reduced mobility due to material from laser irradiation still remains, which limits the effectiveness of this technique for producing optical nonlinearities in laser-written waveguides. This problem may be overcome however, through careful choice of a writing substrate that inherently contains the desired optical nonlinearities. If waveguides are fabricated in such a way that the material properties (and hence nonlinearities) are preserved, then the benefits of stronger interaction with these nonlinearities through optical confinement will be easily obtained without the difficulties of the poling process previously discussed. In the next section, ultrafast laser fabrication of waveguides in crystalline materials is presented, in which waveguides are created in an un-modified region of the substrate, preserving the properties of the material while still providing strong optical confinement.

4.0 FEMTOSECOND MODIFICATIONS IN CRYSTALLINE MATERIALS

As discussed in Section 2.3, waveguide fabrication in crystalline materials using ultrafast laser writing presents a unique fabrication challenge. The properties of crystalline materials are such that waveguides are formed indirectly in relation to the laser-modified region of the substrate. Disruption of the material lattice leads to an induced stress, causing a change in refractive index, the location of which is highly dependent on the stress direction. This section presents efforts to fabricate laser-written waveguides in two crystalline materials, lithium tantalate ($LiTaO_3$) and sapphire (Al_2O_3). Laser writing in lithium tantalate closely follows results reported in other nonlinear, ferroelectric materials such as lithium niobate ($LiNbO_3$), in which waveguiding regions are found to be stress induced and located to either side of the damage site, whereas sapphire demonstrates a stress-induced index change mechanism that is similar but opposite to other crystalline materials. In lithium tantalate, the effects of the laser writing on the nonlinear properties of the crystal are studied using second harmonic (SH) microscopy. Additionally, the mechanisms behind the induced change in refractive index are investigated using confocal micro-Raman analysis. Finally, waveguide writing in sapphire is explored using the same writing techniques and micro-Raman studies to determine the origins of the induced guiding structures.

4.1 LITHIUM TANTALATE

In collaboration with:

Simon Fleming and Honglin An
Second-harmonic microscopy studies
University of Sydney

Daniel Jaque
Micro-Raman analysis
University of Madrid

Lithium tantalate ($LiTaO_3$) is a crystalline material that possesses unique optical, piezoelectric, and pyroelectric properties, making it useful for applications in nonlinear optics [108], terahertz generation [109], and pyroelectric nuclear fusion [110]. The combination of direct laser writing with the unique properties of this material offers an incentive to produce 3D active devices such as optical routers and switches to suit the needs of complicated optical network topologies. Fabrication of low-loss waveguides in crystalline materials is a challenge due to the anisotropic nature of the optical and mechanical properties of these materials, which are more susceptible to laser-induced micro-cracks and optical scattering loss. In the last few years, high repetition rate femtosecond laser pulses have produced low-loss waveguides in amorphous glasses [88,111]. This is largely attributed to heat accumulation effects from repetition rates of 250 kHz or greater, which enhances localized melting and thus assists in minimizing optical loss due to scattering. The high-repetition rate laser processing technique might be especially attractive for waveguide fabrication in crystalline materials as localized melting may reduce the anisotropic stress buildup around focal volume [88].

The formation of index change regions by ultrafast laser irradiation involves multiple processes during the laser interaction with the writing medium. Laser-induced micro-explosions produce voids and localized melting regions around the focal volume. The location, geometry, and magnitude of index change depend strongly on laser processing parameters as well as the properties of the physical writing medium. Using near-field optical microscopy and atomic force microscopy mapping, the index profiles induced in amorphous glasses have been extensively studied [112]. For nonlinear crystals and applications, the impact of laser-induced modification on nonlinear optical coefficients such as $\chi^{(2)}$ and $\chi^{(3)}$ must be considered simultaneously with the index change profile. This work demonstrates the formation of waveguides in lithium tantalate ($LiTaO_3$) through the use of a high repetition rate ultrafast laser. Further, waveguiding and electro-optic (EO) characteristics of the 3D waveguides are studied simultaneously around the laser-modified regions.

Waveguide fabrication was performed using the writing setup outlined in Section 2.4.2, utilizing a writing wavelength of 800 nm and a 40x (0.68NA) aspheric objective. A 0.5 mm thick Z-cut $LiTaO_3$ sample was used as a waveguide substrate, with the writing beam incident along the z-axis (c-axis) of the crystal, and polarized parallel to the writing direction. Waveguides were formed at a depth of 150 μm using various pulse energies ranging from 100 nJ to 1.6 μJ and a wavelength 800 nm. Within this wide laser fluence window, 2.6 cm length waveguides were inscribed with writing speeds from 100 $\mu\text{m/s}$ to 5 mm/s. The samples were then cut, ground, and polished for detailed characterization of each damage site. Within this wide processing window, distinctly different guiding characteristics can be seen at the extremes of this range of parameters.

Figure 4.1(a, b) shows optical microscope pictures of the end-facet profile for damage sites created at 1.6 μJ (5 mm/s) and 300 nJ (1 mm/s), respectively. The writing laser was incident from the top of the image. Both laser fluences yielded a similar lateral waveguide width at 1 μm , which is just slightly larger than the diffraction limit of the given writing objective (0.68 μm). From this we infer that the lateral width only depends on the focal spot size of the objective, which is in contrast to the 2 μm waveguide width formed in fused silica using the identical optical setup and processing parameters.

The cross-sectional view of the modified region reveals significant differences between the two laser energies. At the maximum available pulse energy of 1.6 μJ , the modified region induced by the writing beam is much larger than that caused by the lower pulse energy of 300 nJ. Despite the higher pulse energy, no visible voids were formed for this high fluence, which can be attributed to increased nonlinear absorption (self focusing, etc.), leading to energy depletion and limiting the peak fluence of the laser pulse. In an interesting contrast, reducing the pulse energy to 300 nJ led to the appearance of voids, which can be seen as a dark strip (~ 20 μm in length) below the laser modified region. Both pulse energies exhibit a bright narrow strip, which appears to be the guiding region, although for higher energies guiding was found to exist outside this region in the bulk material. For the given conditions, the laser-modified region extends much deeper into the substrate than the Rayleigh range of the objective (~ 13 μm), which is likely due to nonlinear filamentation of the focused writing beam. The depths of visible laser damaged regions are ~ 72 and ~ 34 μm , respectively. This is in contrast to fused silica, where the depth of the laser-modified region roughly matches the depth of the focus of the objective.

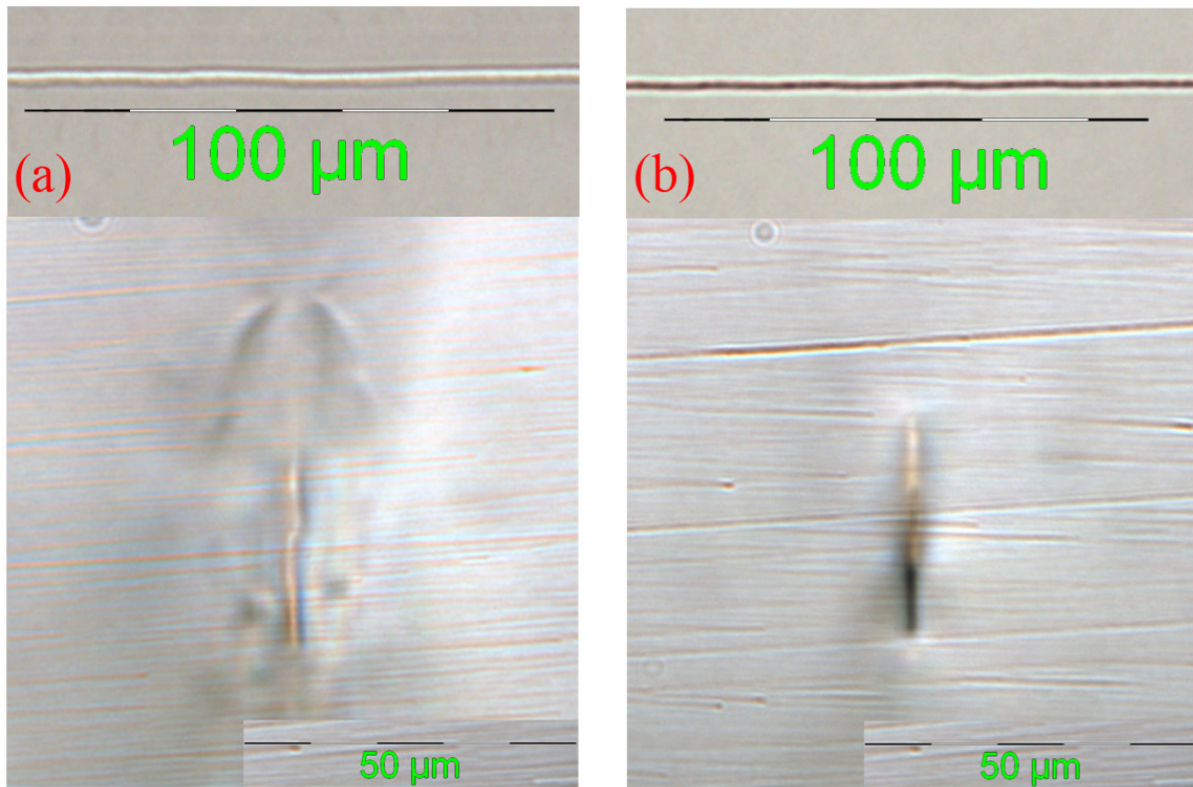


Figure 4.1 - Optical microscope images of laser induced damage sites in lithium tantalate for pulse energies and translation speeds of (a) 1.6 μJ at 5 mm/s and (b) 300 nJ at 1 mm/s. Reprinted with permission from [31]. Copyright 2008, [American Institute of Physics](#).

Figure 4.2(b – e) shows mode profile images captured using an IR CCD camera for the damage site pictured in Figure 4.1(a) guiding 1550 nm. This waveguide was inscribed with incident pulse energy of 1.6 μJ and a writing velocity of 5 mm/s. The white-light image in Figure 4.2(a) was taken with the same IR camera just before capturing the mode profile, and is given for reference in order to spatially locate the guided modes within the laser-modified structure. The red scale bar in all figures represents a length of 15 μm . The extent of the laser-modified region is quite large, producing several guiding regions at 1550 nm.

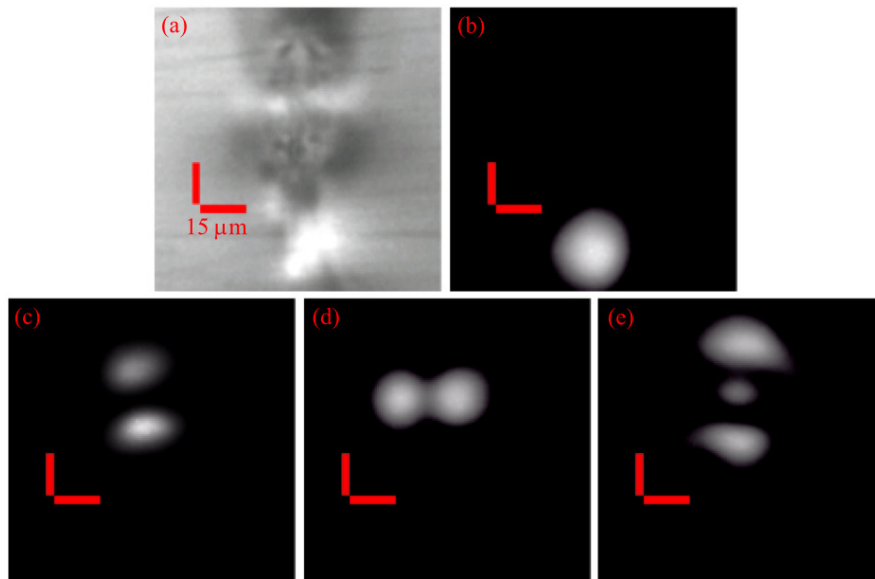


Figure 4.2 – (a) White light image of a damage site fabricated with with 1.6 μJ pulses and a velocity of 5 mm/s. (b)-(e) Layout of various guiding regions for the damage displayed in (a). The scale bar in the image represents a distance of 15 μm . Reprinted with permission from [31]. Copyright 2008, [American Institute of Physics](#).

A well-defined single-mode appears below the laser-modified region, as shown in Figure 4.2(b). In contrast, guiding above the laser-modified zone yields complex mode structures. By changing the launching condition, it was possible to couple into adjacent structures in the laser-modified region, as shown in Figure 4.2(c – e). Due to the complexity of these structures, some of the observed modes may be higher order.

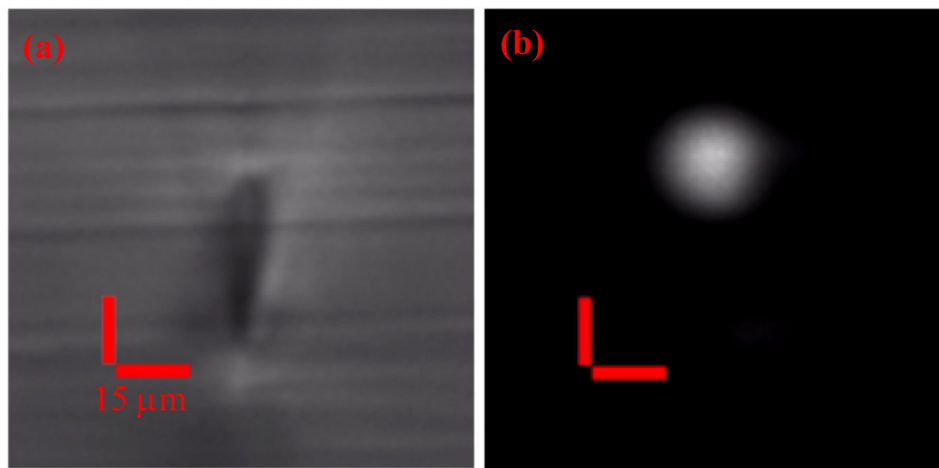


Figure 4.3 – (a) White light image for a damage site fabricated at 300 nJ and a velocity of 1 mm/s. (b) guided mode for the damage site written displayed in (a). The scale bar in the image represents a distance of 15 μm . Reprinted with permission from [31]. Copyright 2008, [American Institute of Physics](#).

Figure 4.3 (a) and (b) shows the guided mode for a damage site written with 300 nJ pulses and a writing speed of 1 mm/s. At lower pulse energies, guiding was found only to occur at regions just above the laser-modified region, where a single-mode waveguide appears to form with an average mode-field diameter (MFD) of $\sim 20 \mu\text{m}$.

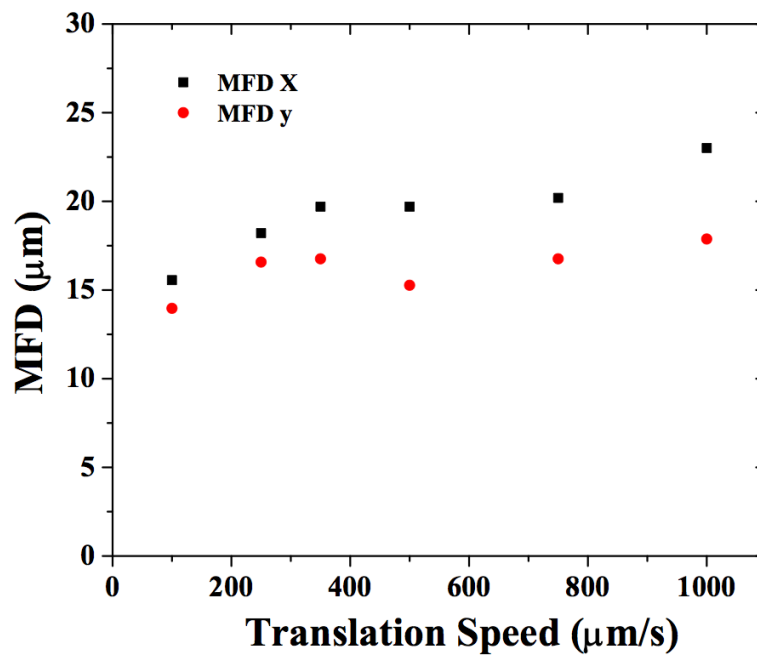


Figure 4.4 - X and Y mode-field-diameters for the 300 nJ damage site depicted in **Figure 4.3**. Reprinted with permission from [31]. Copyright 2008, [American Institute of Physics](#).

Figure 4.4 plots the MFD as a function of laser writing speed for a pulse energy of 300 nJ. If the lateral size of 1 μm from the visual inspection shown in Figure 4.1(b) is used as the waveguide size, the index change induced by the 300 nJ laser pulse is estimated to be greater than 1×10^{-2} . Single-mode guiding regions were also formed for pulse energies of less than 300 nJ, with writing speeds between 100 $\mu\text{m/s}$ to 1 mm/s.

In addition to the guiding properties, the modification of the nonlinear optical properties of the laser-modified region is equally important for device applications. The modification of the second-order nonlinearity (SON) was studied and visualized using second-harmonic (SH) microscopy, which is a non-destructive characterization technique commonly used for the analysis of second-order nonlinearities [104]. A diagram of this setup can be seen in Figure 4.5. This setup consisted of an inverted Leica DMIRBE microscope and Leica TCS2MP confocal system, with an excitation wavelength of 830 nm provided by a Coherent Verdi-Mira laser system, producing pulses in the 100 – 200 fs range. The SH setup was equipped with dual photomultiplier transmitted light detectors to capture both the ordinary and SH optical transmission. A dichroic filter (505 DCLP) divides the detectable spectrum (380-680 nm) at 505 nm, delivering a different portion to each channel. The shorter (channel 2) and longer (channel 1) channels were each filtered, to receive only the SH signal (channel 2) and two-photon fluorescence (channel 1), respectively. Maximum SH signal was obtained by orienting the sample such that the polarization of the excitation light was parallel to the poling direction [104].

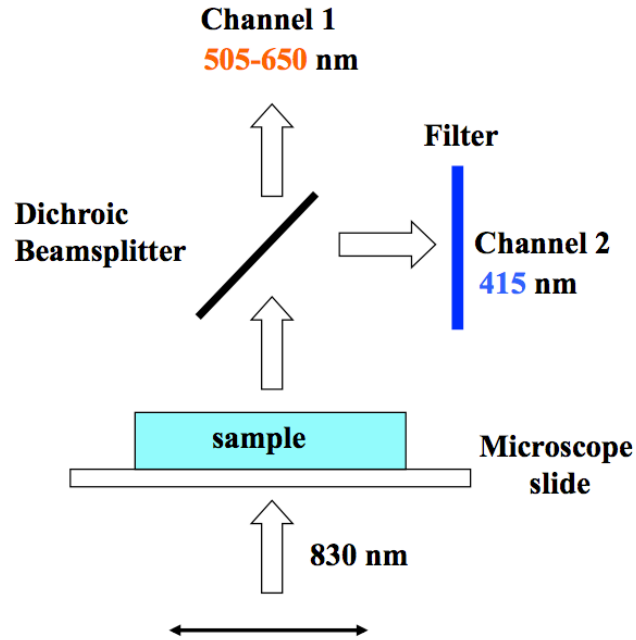


Figure 4.5 – Detail of the second-harmonic setup used for characterization of the poled silica samples. Reprinted with permission from Honglin An, University of Sydney.

Figure 4.6(a) shows the ordinary transmission image of a waveguide cross section. A linearly polarized 830 nm Ti:Sapphire laser was focused and scanned across the end-facet of the waveguide, while the resulting SH signal was collected to form an SH image of the waveguide, as shown in Figure 4.6(b). The transverse spatial resolution of the SH microscopy was estimated to be $\sim 0.4 \mu\text{m}$ with a depth of focus $\sim 2 \mu\text{m}$. Most of the SH signal was collected within the focal volume. The polarization of the incident fundamental beam was along the horizontal direction, as indicated in Figure 4.6(b).

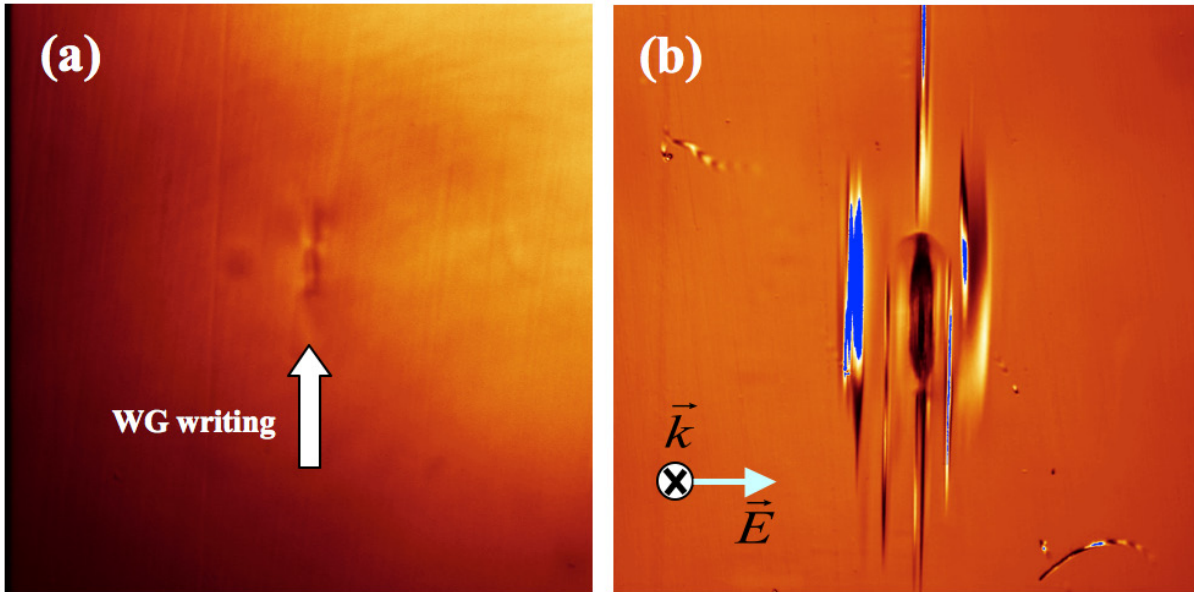


Figure 4.6 - (a) Microscope image for the laser damage site written at 300 nJ and 2 mm/s translation speed as captured with the SH microscope setup and (b) the corresponding SH image. The incident writing beam direction and polarization and propagation direction of the incident excitation laser are indicated in (a) and (b) respectively. The blue region in (b) indicates a saturation of the SH signal. Reprinted with permission from [31]. Copyright 2008, [American Institute of Physics](#).

It can be seen that, within the focal volume, the SON has been significantly decreased, displaying a darker region compared to other parts of the sample. The edge of the region containing decreased SON signal appears smooth, suggesting that melting and re-solidification of the substrate has occurred. This loss of SON within the focal volume indicates a destruction of the crystalline lattice resulting from irradiation by femtosecond laser pulses. Within the focal volume, the laser intensity is sufficiently high to promote nonlinear absorption processes, transferring the laser energy to the crystal lattice and raising the temperature above the melting

point of the substrate. After the pulse is no longer present, the focal volume quickly cools (within tens of microseconds), leaving behind an amorphous structure, thus losing original SON. This process should be accompanied by a reduction in material density (increase in volume), creating stress around the focal volume, which could explain the substrate distortions observed around the laser-modified region in Figure 4.6(b).

Initial examination of these results indicates that the decrease of SON within the focal volume is a drawback to fabrication of waveguides in LiTaO₃ using femtosecond laser writing. However, it is important to remember that guiding regions created by induced stress are found above and below the focal volume, as shown in Figure 4.2 and Figure 4.3. For the guiding region above the focal volume, an increase of $\sim 2x$ in the SH signal was observed as compared to that collected from the bulk material. Even stronger SH signal was observed along both sides of the focal volume, which saturated the detector. Most of the SH signal was collected within a focal volume with the depth of 2 μm , which is comparable to the coherence length of about 1.7 μm for the process of the SH generation. Thus the increase of the SH signal is unlikely due to domain inversion of the crystal. It is possible however, that the structure inhomogeneity and drastic index change induced by the ultrafast laser is likely to cause an increase of the SH signal.

In order to gain further insight into the mechanisms behind the induced refractive change, and to estimate the total magnitude of index change produced, micro-Raman analysis was performed [113] on a damage site created with 300 nJ pulses and a translation speed of 1 mm/s. A transmission image of this feature is shown in Figure 4.7(a), with the corresponding guided mode at 1550 nm shown in (b), just above the laser-written feature.

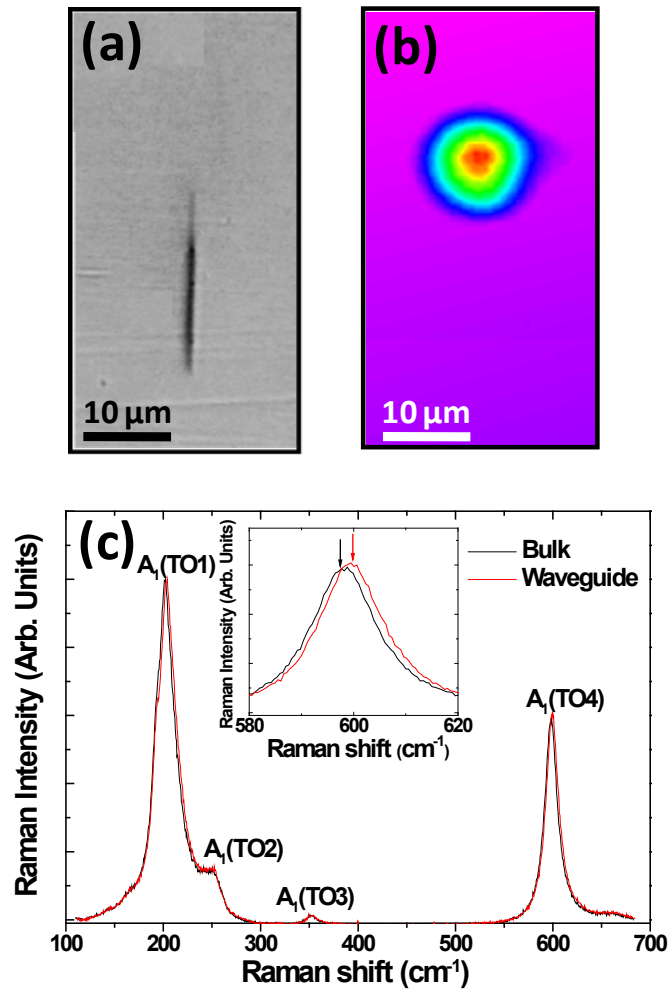


Figure 4.7 – (a) Microscope image of a damage site written at 300 nJ and a translation speed of 1 mm/s. (b) Guided mode profile of the stress-induced waveguide at 1550 nm. Note the proximity to the laser-induced damage site. (c) $x(zz)\bar{x}$ micro-Raman spectrum as obtained from the bulk (black) and waveguide (red) locations. The inset shows a magnified view of the $A_1(\text{TO4})$ mode. Reprinted with permission from [113]. Copyright 2009, [American Institute of Physics](#).

Micro-Raman investigations were performed with a fiber-coupled confocal microscope, which delivered a 488 nm excitation beam to the sample surface via a 100x oil immersion objective (UplanSApo, 1.4NA). The spatial and spectral resolutions of this system were estimated to be 200 nm and 0.4 cm^{-1} respectively. A spatial Raman spectral map was obtained using the two-axis positioning capabilities of the microscope system. Typical $x(zz)\bar{x}$ Raman spectra as obtained from bulk material (un-irradiated) and waveguide location are shown in Figure 4.7(c). The Raman A(TO) modes are labeled and properly identified according to prior work [114]. The similarity between the two obtained spectra gives relevant information about the modifications induced in the crystal lattice. The lack of appearance of additional Raman modes suggests that the crystal structure has not been re-arranged by laser damage within the location of the waveguide. Additionally, no reduction in intensity is found indicating that the lattice has not been significantly damaged. Upon further examination of the $A_1(\text{TO4})$ mode, as shown in the inset of Figure 4.7(c), a clear shift toward larger vibration energies is found. Similar shifts were also found for the $A_1(\text{TO1})$ and $A_1(\text{TO2})$ modes as well. The weak intensity of the $A_1(\text{TO3})$ mode prevented accurate measurement of any induced shift due to the error involved with the fitting process.

When examining the data as a whole, the general blueshift of the Raman modes suggests the presence of compressive stress within the guiding region, as reported by previously published work [115], and similar results have been reported for ultrafast laser written waveguides fabricated in gadolinium tungstate crystals [116]. Compressive stress is known to cause an increase in refractive index [117], and here likely accounts for the formation of the guiding structure, provided that the induced change in lattice density is dominant over the pressure induced changes in the average electronic polarizability [118].

To further correlate these results with the formation of waveguides in lithium tantalate, spatial Raman maps for the integrated Raman intensity, shift, and line width of the $A_1(\text{TO}_4)$ mode were obtained, as shown in Figure 4.8.

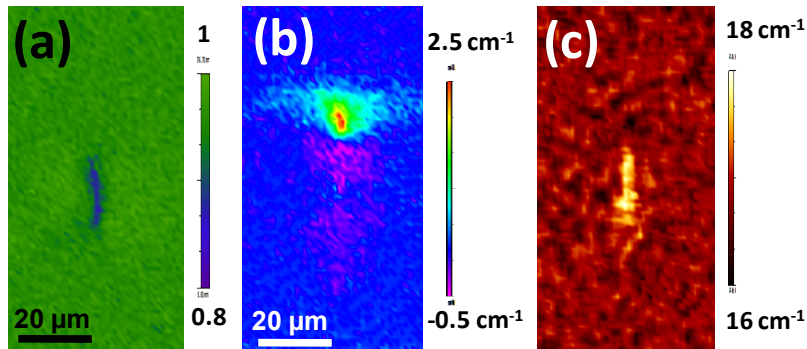


Figure 4.8 – Spatial Raman maps for the $A_1(\text{TO}_4)$ mode, showing (a) the integrated Raman intensity, (b) Raman shift, and (c) line width of the $A_1(\text{TO}_4)$ mode. Reprinted with permission from [113]. Copyright 2009, [American Institute of Physics](#).

A 20% overall reduction in Raman intensity is found in the region of the focal volume, as depicted in Figure 4.8(a), indicating extensive lattice damage and void formation. Broadening of the Raman line (Figure 4.8(c)) lends further support to the creation of lattice disorder within the region modified by the laser focal volume. Results presented earlier in this section also support this notion, as it was found that the nonlinear coefficients of the material lattice are significantly reduced [31]. The location of the waveguide is indicated in Figure 4.8(b), where the spatially resolved induced shift coincides with the spatial location of the guided mode, as displayed in Figure 4.7(b). It is evident from Figure 4.7 and Figure 4.8 that the compressive stress (and hence

waveguide cross-section) has minimal overlap with the laser-damaged region of the substrate, ensuring minimum propagation losses.

Figure 4.8 gives additional information about the parameters of the induced waveguide as well. As there is no noticeable reduction in the integrated Raman intensity (Figure 4.8(b)), one can infer that the nonlinear properties of the substrate are preserved in the region of the waveguide. Taking the full-width-half-maximum (FWHM) of the induced shift, as displayed in (b), gives a better estimate of the physical waveguide size. A Gaussian fitting yields values of 6.2 μm and 7.1 μm along the vertical and horizontal directions respectively, which is in contrast to the ~ 2 μm lateral width of the laser-induced damage site. Lastly, the overall magnitude of the induced shift in (b) may be used as a rough estimation of the material compression induced by the laser damage site. Using the Grüneisen parameter of the $A_1(\text{TO}_4)$ mode ($0.2 \text{ cm}^{-1} / \text{kBar}$) [115], a maximum compressive stress of ~ 10 kBar is estimated at the location of the waveguide. Given that there is clear evidence of a change (increase) in refractive index due to lattice compression, it may be assumed that the change in the lattice unit cell volume ($\Delta V/V \sim 10^{-2}$, estimated from the averaged Young's modulus of LiTaO_3) is dominant over the pressure-induced reduction in electronic polarizability.

Raman maps were also obtained for features written with higher pulse energies of 1 μJ . These images are shown in Figure 4.9. An optical microscope image of the damage site is displayed in (a) as a reference. As was evident from Figure 4.2, multiple guiding regions are found for features written at higher pulse energies, suggesting the extent of induced index change (and induced stress) spans a larger distance than for the case of features written at 300 nJ. For this higher energy case, a reduction in Raman intensity is also found in the region of the focal volume (Figure 4.9(b)), again indicating a reduction of material density due to lattice damage

and void formation. A general blueshift of the Raman modes is found surrounding the focal volume, as displayed in Figure 4.9(c).

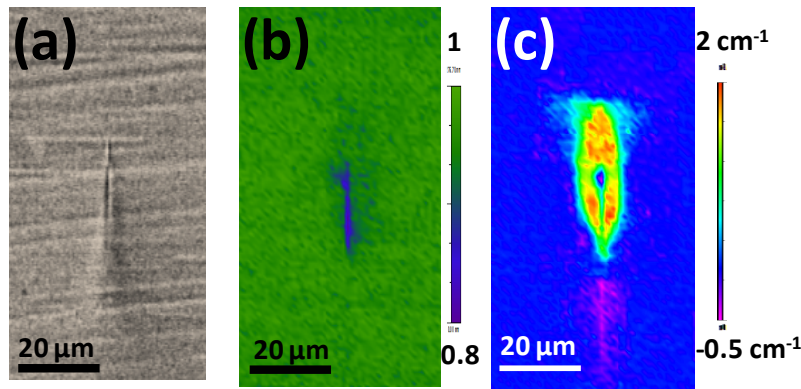


Figure 4.9 – (a) optical microscope image of a laser-induced damage site written at 1 μJ and 1 mm/s translation speed. (b) Spatial map of the integrated Raman intensity for the A₁(TO₄) mode and (c) induced shift of the same mode. Reprinted with permission from [113]. Copyright 2009, [American Institute of Physics](#).

Following the same argument as presented for Figure 4.8, the measured induced shift displayed in Figure 4.9(c) suggests that the increase in pulse energy generates much larger compressive forces, thereby distorting a larger region of the lattice around the focal volume. This larger area of material compression likely gives rise to a more spatially expansive change in refractive index leading to the multi-mode guiding behavior observed in Figure 4.2. It should be noted that the results of this work are in contrast to previous reports of ultrafast laser waveguide fabrication in *LiNbO₃*, in which Raman shifts within the volume of the waveguide were found to trend toward a general redshift [119]. The difference in induced shift denotes different

mechanisms involved in the formation of the guiding region. In the case of $LiNbO_3$, waveguide formation was found to be a consequence of a change in the spontaneous polarization brought about by ionic rearrangement of the material lattice.

The work presented in this section opens the possibility for waveguide fabrication in other crystalline materials. Although the detailed mechanism of the SON changes is unknown, strong SH signal shown in Figure 4.6(b) provides clear evidence that the guiding region retains the crystalline structure of the bulk substrate along with a preserved and strong SON coefficient. This is further re-enforced by the evidence of a guiding region, as indicated by the spatial Raman maps depicted in Figure 4.8 and Figure 4.9. These maps confirm the location of the waveguide, as well as give clear evidence that the guiding region is located well away from the laser induced damage track, and that the crystal structure within this region is preserved. These results suggest that efficient nonlinear optical devices based on 3D waveguides can be fabricated using ultrafast lasers.

In the next section, the writing technique presented here is extended to include waveguide fabrication in crystalline sapphire. Though the damage imparted to the material induces stress surrounding the focal volume, the mechanisms behind index change and waveguide formation are opposite to those found in lithium tantalate. Additionally, the induced refractive index is lower so that guiding is not supported at 1550 nm.

4.2 SAPPHIRE

In collaboration with:

Daniel Jaque and Antonio Benayas
Micro-fluorescence investigations
University of Madrid

This section presents efforts to extend waveguide fabrication using high repetition rate (250 kHz) repetition rate ultrafast laser pulses to sapphire (Al_2O_3) crystals. The use of UV (400 nm) laser pulses is employed, reducing the order of the multi-photon excitation process, and consequently the laser intensity required for permanent index modification of the crystal lattice. The basic propagation properties of the obtained waveguides as a function of the writing conditions (such as pulse energy and writing speed) are reported and discussed. In order to gain a better understanding of the laser-matter interaction in sapphire under these irradiation conditions, and to determine the waveguide formation mechanism, spatial and spectral analysis of micro-fluorescence generated by trace Cr^{3+} ions is analyzed. Given this information, the refractive index change induced by the laser-modified focal volume is also estimated.

There are many potential applications for sapphire in harsh, high-temperature environmental sensing [120] and super continuum generation in the mid-IR range [121]. Sapphire may also be doped with transition metal ions, making it a well-known material for solid-state lasers and optical amplifiers [122]. Several methods of waveguide fabrication in sapphire have already been investigated, including ion in-diffusion, pulsed laser deposition, reactive ion etching, and ion beam implantation [123-125]. Very recently, channel waveguides in

Ti-doped sapphire crystals have also been fabricated using a low-repetition rate infrared laser, operating at 1 kHz with a wavelength of 750 nm [126], however the possible optimization of these waveguides based on the benefits of bulk heating from high-repetition rate ultrafast laser pulses is still unexplored.

The waveguides studied in this work were fabricated with the laser system outlined in Section 2.4.2, while utilizing the second-harmonic generation (SHG) portion of the setup, producing 400 nm pulses at a repetition rate of 250 kHz. The writing beam was focused into a nominally pure, (0001) oriented Sapphire sample (Crystal Systems Inc.) at a depth of 150 μm with a 40X (0.68NA) aspheric objective. The sapphire sample was translated at velocities of 0.2 to 5 mm/s, allowing inscription of waveguides parallel to the A-axis (1120 crystallographic axis), with pulse energies varying from 100 to 500 nJ.

Figure 4.10 (top) shows the optical microscope cross-section images of the laser-induced modification produced in the Sapphire sample with different pulse energies and translation speeds. Arrows indicate the propagation direction of the UV irradiation pulses. Note that the length of the modified region decreases with decreasing pulse energy and increasing translation speed, as expected for a total reduction in laser fluence under these conditions. The guiding properties of the laser-written structures were investigated using a 632 nm He-Ne laser, which was coupled into the damage sites and surrounding substrate with a 20x microscope objective. Regions with enough index change to support guided modes were found a few microns below the damage sites. Within the explored processing window, features written at the highest pulse energy of 500 nJ displayed guiding regions for all translation speeds studied (0.2 – 5 mm/s).

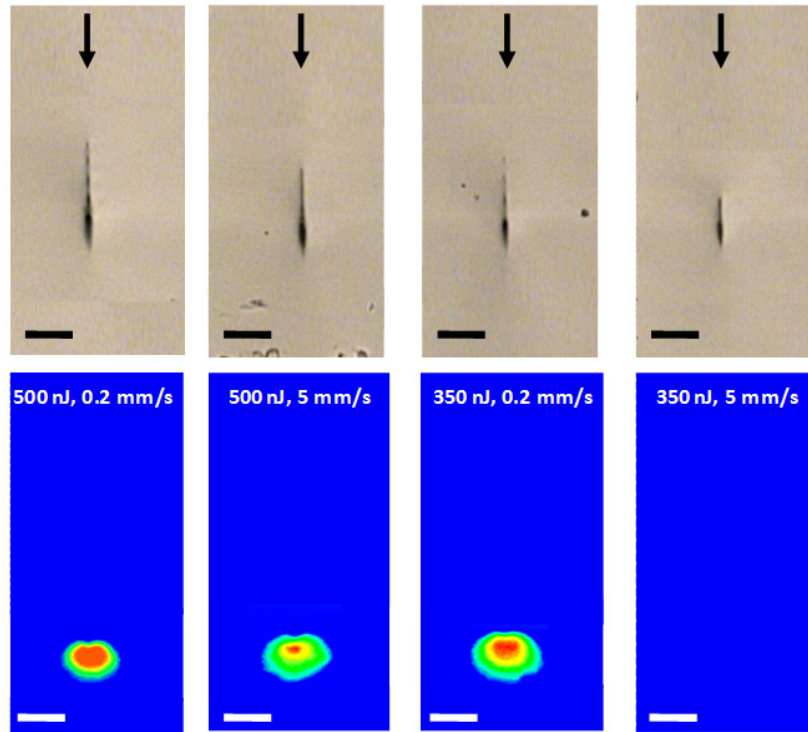


Figure 4.10 - Optical microscope images of the end face of the irradiated Sapphire sample as obtained for different pulse energies and translation speeds. The black arrows visible in the top of the figure indicate the propagation direction of the UV writing pulses. Fundamental propagation modes at 632 nm for each waveguide are shown in the bottom half of the figure. Note that, for the feature written with pulse energy of 350 nJ, no waveguiding was found for the maximum translation speed. Scale bar is 20 microns. Reprinted with permission from [35]. Copyright 2009, [Optical Society of America](#).

It was also found that the maximum translation speed at which guiding formations are found decreases constantly with decreasing pulse energy, which is clearly shown in Figure 4.10 (bottom). For the intermediate pulse energy of 350 nJ, sufficient index change to support a guided mode was only observed for the feature written with the minimum translation speed of 0.2 mm/s.

For all of the waveguides studied in this section, no waveguiding was found for the telecom wavelength of 1550 nm. This fact may be due to weak index change and/or an index change region that is (spatially) too small to support guiding at this wavelength. The relative location of the guiding regions with respect to the damage site is very similar to the results obtained in sapphire using low repetition rate IR laser pulses [126].

In order to gain a better understanding of the waveguide formation mechanisms, micro-fluorescence from trace amounts of Cr^{3+} ions was analyzed and used as a marker to determine if further optimization of the waveguide writing process in sapphire was possible. In sapphire, the concentration of trace Cr^{3+} ions has been estimated to be no higher than 0.1 atomic %. Micro-fluorescence studies were performed with a scanning confocal microscope, which collected the fluorescence signals generated by the laser-modified regions with a 100x (0.9NA) microscope objective. This objective was used for both delivering the 488 nm excitation beam, as well as collecting fluorescence signal from the sample. After passing through a confocal aperture, the collected signal was then focused into a fiber-coupled, high-resolution spectrometer. Typical micro-luminescence spectra obtained for this experiment can be seen in Figure 4.11(a), which shows two sharp, well-defined R lines characteristic of Cr^{3+} ions [127].

This well-known spectral feature is an invaluable tool for investigating and understanding ultrafast laser interaction with the sapphire lattice. Analysis of the spectral shift, intensity, and

spectral broadening of this feature in relation to the spatial location has been found to give information about changes in the lattice of similar crystalline materials [127], and is used here to determine the mechanisms behind waveguide formation in sapphire. For this investigation, a 488 nm excitation spot originating from the previously mentioned confocal microscope setup was scanned over the cross-sections of four laser-written structures as shown in Figure 4.10. It was found that, in all cases, the intensity of the *R* lines was strongly reduced within the focal volume of the laser-written feature. This was also accompanied by a slight spectral broadening, as shown in Figure 4.11(a) and (b). Both figures correspond to the structure fabricated with pulse energy of 500 nJ and a translation speed of 0.2 mm/s.

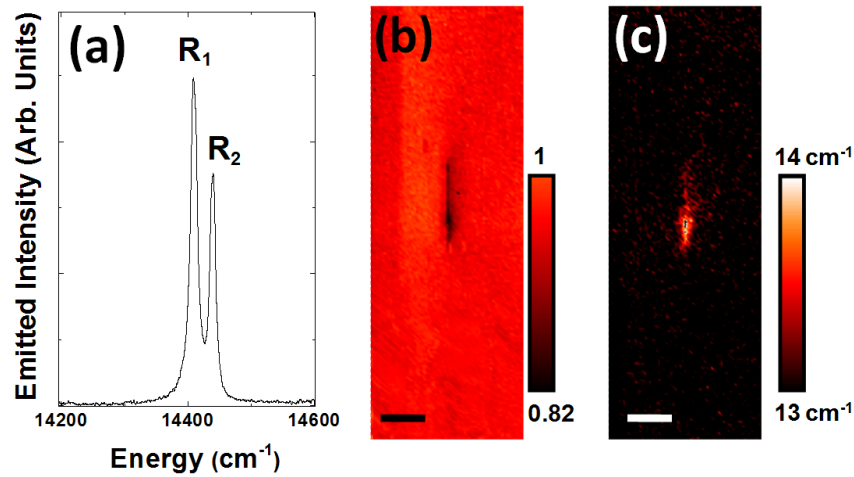


Figure 4.11 - (a) Measured micro-luminescence spectra from the micro-structured sapphire sample, as obtained after 488 nm excitation. The R_1 and R_2 lines generated by Cr^{3+} traces are labeled. (b) Spatial dependence of the R_1 line intensity and (c) bandwidth as obtained from the laser-written feature fabricated with a pulse energy of 500 nJ and a translation speed of 0.2 mm/s. Scale bar is 20 microns. Reprinted with permission from [35]. Copyright 2009, [Optical Society of America](#).

The simultaneous reduction and broadening of the R lines displayed in Figure 4.11 denotes a partial damage and/or disordering of the sapphire network in the region of the laser focal volume, which is likely due to the large laser fluences achieved during writing. Evidence of filamentation due to self-focusing of the writing beam (as shown in Figure 4.10) further supports this hypothesis. In the region of waveguide formation, just below the focal volume, no significant reduction or broadening of the Cr^{3+} lines is found, indicating that the laser-induced waveguide is located in an un-damaged region of the bulk material.

While the reduction of intensity and broadening of these R lines provides information about modification of the material lattice, more relevant information about the mechanism

behind waveguide formation can be obtained by examining the spectral shift of these lines with respect to spatial location on the end-facet of the sample. A spatial map displaying the spectral shift of the R_1 fluorescence line can be seen in Figure 4.12 [128]. These spectral maps are representative of the same four laser-written structures displayed in Figure 4.10. Analysis of the R_2 line produced similar images as well.

It was found that, for the structures displaying sufficient index change to support a guided mode (features created with 500 nJ pulse energy and those obtained with 350 nJ pulse energy and a minimum translation speed of 0.2 mm/s), the fluorescence images display clear evidence of a spectral shift in the R_1 line. The structural modifications found in these features are characterized by a red shift of the R_1 line within the focal volume and by a blue shift of the same line at the location of the induced guiding region, just below the laser damage site. It is well known that a shift of the R_1 line is indicative of a compressive or tensile stress within the sapphire lattice. In the case of the laser-written features presented here, disruption of the local lattice within the focal volume creates compression through an increase in material density (red shift), causing a tensile stress (dilation) in the region of the waveguide location (blue shift). These results are consistent with prior reports [34,128,129], in which it was concluded that the refractive index of sapphire increases when a tensile stress is applied (when the local density is reduced). This result is a direct consequence of the dominant contribution of the electronic polarizability enhancement over the atomic density reduction of the lattice.

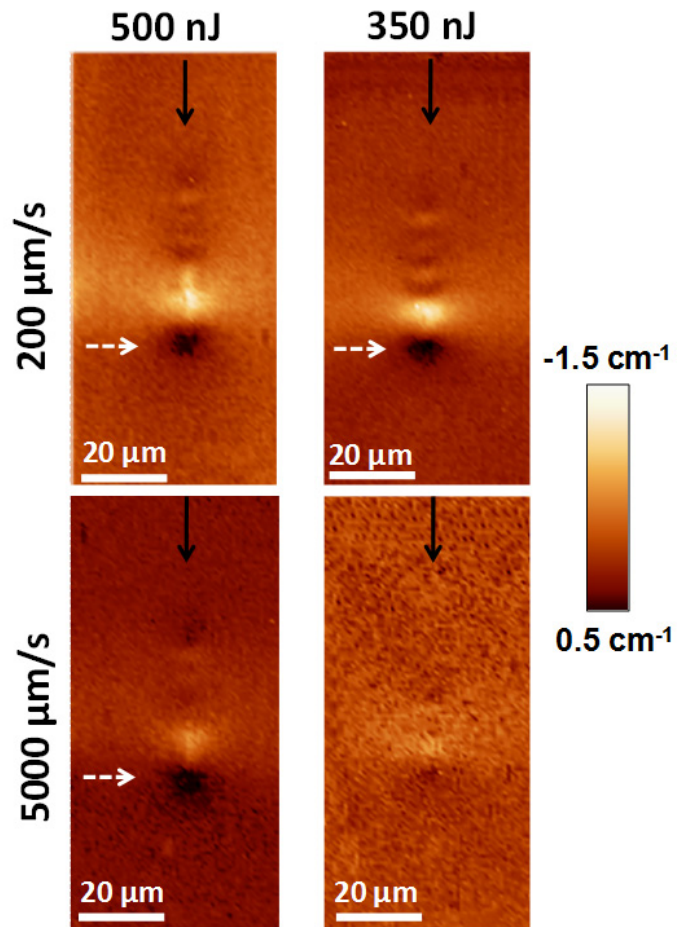


Figure 4.12 - Spatial distribution of the spectral shift of the R_l line as measured for four damage sites. The pulse energy and translation speed for each feature is labeled accordingly. The direction of the incident writing beam and waveguide location are represented by solid and dashed arrows, respectively. Reprinted with permission from [35]. Copyright 2009, [Optical Society of America](#).

The fluorescence images displayed in Figure 4.12 reveal that the region of refractive index change (and location of the guiding region) is a locally dilated area, just below the laser damage track. For the structure written with pulse energy of 350 nJ and a translation speed of 5 mm/s, no appreciable blue shift of the R_1 line was observed, suggesting that the total deposited energy was not sufficient to generate a significant density modification in the Sapphire network, leading to an absence of guided mode support for this structure. It is clear that, for the sapphire case presented here, waveguides are formed as a consequence of a local lattice dilatation. This in contrast to laser-written waveguides fabricated in other crystalline systems, in which local compression of the material lattice has been identified as the mechanism behind refractive index change [31].

There exists a well-established pressure coefficient of the R_1 line, which was used in conjunction with the measured red and blue shifts displayed in Figure 4.12 to estimate the maximum induced compressive and tensile stresses stress present in the substrate around the laser-modified region [128,130]. For the structure written at 350 nJ and 0.2 mm/s, these values were found to be 0.46 GPa at the focal volume (compressive) and 0.25 GPa at the location of the guiding region (tensile), which is consistent with a similar analysis based on the R_2 line shift. The tensile stress of 0.25 GPa induced in the guiding region yields a density variation of $(\Delta\rho/\rho_o) \approx 0.4\%$ and $\approx -0.2\%$ at the focal volume and waveguide, respectively. According to S.C. Jones *et al.* [34], these variations in the local density would cause a refractive increment of $\Delta n = -0.1 \cdot (\Delta\rho/\rho_o) \approx 1 \times 10^{-4}$ at the waveguide location. This value is comparable to previous reports on laser-written waveguides in Sapphire fabricated with low repetition rate IR ultrafast pulses ($\Delta n \approx 2 \times 10^{-4}$) [127]. This index change is not sufficient to support guided modes at the telecommunication wavelength of 1550 nm.

The evidence presented in this section gives clear insight into the fabrication difficulties concerning devices in crystalline materials. Though these challenges are easily overcome, the requirements on pulse width and focusing conditions are not overly strict. Additionally, the nonlinearities associated with these materials do not greatly influence the creation of the guiding structure due to the mechanisms involved. The inclusion of nonlinearities within the guiding region and preservation of the material properties make ultrafast laser inscription an attractive avenue for waveguide fabrication in crystals, however the stress mechanisms involved in refractive index change limit this approach due to its directional nature. For this reason, it is often desirable to fabricate waveguides in glasses that also contain nonlinearities. As will be discussed in the next section, the creation of smooth index change in highly nonlinear amorphous materials presents an even greater challenge, as the combination of high nonlinearity along with a large refractive index contrast between the substrate and air induces both temporal and spatial distortions at the focus, leading to degradation of the waveguide quality.

5.0 CHALCOGENIDE GLASS

Chalcogenide (CHG) glasses are a class of semiconducting materials based on the chalcogenide elements of sulfur (S), selenium (Se), and tellurium (Te), and are formed when combined with other elements such as germanium (Ge), arsenic (As), antimony (Sb), and gallium (Ga). They exhibit exceptional properties, such as low phonon energy, wide optical transmission windows from the visible to the mid infrared, and third order nonlinearities several magnitudes higher than those found in silica glasses.

Interest in these materials has grown considerably owing to the inherently high nonlinearities present in these materials, along with their applications to mid-IR photonics [131] and all-optical switching [132]. While ultrafast laser writing has been applied to a variety of materials, including those with optical gain [133] and strong optical nonlinearities [134], more recent work has demonstrated waveguide fabrication in chalcogenide glass using a variety of writing techniques. These methods including a single [135] and multiple-pass [136] writing approach. Though these methods have shown that direct-laser writing in chalcogenides is indeed a possibility, the material properties of these glasses have made the fabrication of waveguides and photonic devices particularly difficult.

As with all methods of creating photonic devices, an important aspect of the fabrication process is to optimize the processing parameters to improve the optical qualities of the fabricated structures. In ultrafast laser writing, this is nominally achieved through proper choice and fine-

tuning of several factors, including repetition rate, wavelength, writing speed, and pulse energy of the laser. In many situations however, adjustment of these parameters is not sufficient to produce optical devices with satisfactory performance.

This challenge is most evident for laser processing of chalcogenide glasses. The very properties of high nonlinearity that are considered beneficial also have a strong impact on laser pulse propagation, and thus affect the outcome of device fabrication. This effect is difficult to mitigate through the optimization of laser writing parameters alone. Additionally, spherical aberrations resulting from the high refractive index of this material are introduced at the focus of the writing laser, distorting the focus at depths of more than a few tens of microns and adding further difficulty to the fabrication process.

This section presents efforts to improve the process of fabricating waveguides in chalcogenide glass using an ultrafast laser and to apply these techniques to produce more advanced devices (beyond basic waveguides) for mid infrared applications. The first section (Section 5.1) is devoted to the improvement of both the spatial and temporal profile of the writing beam in order to improve linear and nonlinear laser-material interactions. These efforts result in low loss waveguides with a nearly circular cross section. In Section 5.2, this technique of waveguide fabrication is then applied to the formation of multi-order Bragg waveguides for use in mid infrared applications.

5.1 GALLIUM LANTHANUM SULFIDE (GLS)

In collaboration with:

Daniel Jaque and Antonio Benayas
Micro-Raman investigations
University of Madrid

To overcome the fabrication challenges associated with ultrafast laser fabrication of photonic devices in chalcogenide glass, this section explores spatial beam shaping [86] and temporal pulse shaping using adaptive optical elements [137] as a means to mitigate spatial and temporal distortion of the writing beam. These efforts result in significant improvements to the quality of waveguides produced in CHG glasses using the ultrafast laser writing technique. Optimization of the spatial profile, as well as the pulse width of the writing beam, leads to a highly symmetric single-mode waveguide at 1560 nm with a minimum propagation loss of 0.65 dB/cm.

Due to a high non-linear figure of merit and superior environmental stability [138], gallium lanthanum sulfide (GLS) chalcogenide glass was chosen as the waveguide substrate. The writing beam, which was supplied by the laser system outlined in Section 2.4.2 and circularly polarized, was focused at a depth well below ($\sim 275 \mu\text{m}$) the surface of GLS substrate (25x25x1 mm, ChG Southampton) using a 40x aspheric lens ($\text{NA} = 0.68$). This depth was chosen to prevent damage to the waveguide end facets due to chipping of the sample edges from regular handling. The incident pulse energy was fixed at 400 nJ. These conditions were chosen to provide the best material response over a wide range of pulse-widths, giving a strong and consistent change in refractive index. In preparation for characterization, the sample was cut and polished to a high optical grade.

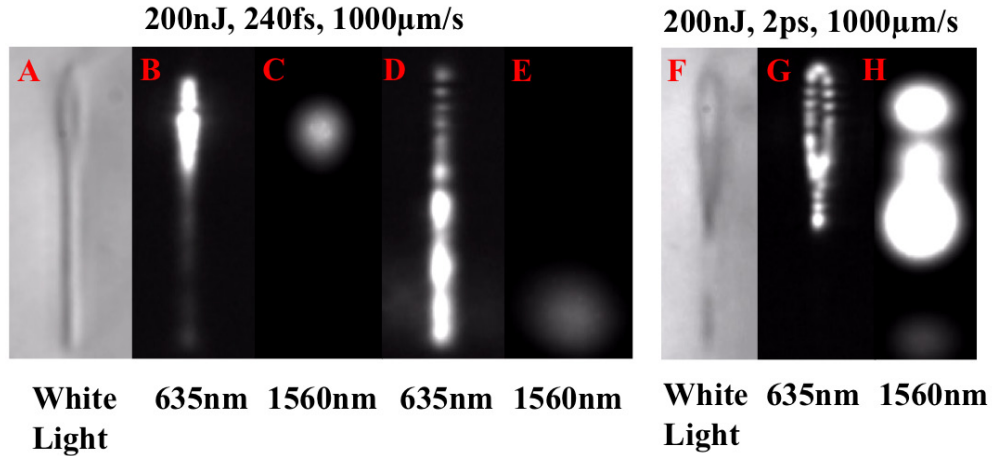


Figure 5.1 – Plot of guided modes displaying the pulse width dependence of the waveguide writing process in GLS chalcogenide glass at pulse widths of 240 fs (left) and 2 ps (right). The images in (A) and (F) are representative white light images of the laser-induced damage sites, as captured with a microscope. These are given as a reference so that the guided modes may be spatially located within the feature. Reprinted with permission from [28]. Copyright 2012, [Optical Society of America](#).

The strong nonlinearity present in GLS substrates presents a significant challenge for ultrafast laser processing as shown in Figure 5.1(A – E), which displays an optical microscope image of laser-induced features written with a pulse-width of 240-fs along with supported guided modes. These images were acquired simultaneously so that the guiding region may be spatially located within the cross-section of the laser written features. These results are in agreement with *Hughes et al.* [135], where highly asymmetric features are found due to a combination of spherical aberration and strong non-linear material interaction (Figure 5.1A). One guided mode was observed at 1560 nm in the 'head' of the modified zone (Figure 5.1C), with a second guiding zone present near the 'tail' of the same feature (Figure 5.1E). Mode-field diameters observed in both regions are significantly larger than the width of visible damage tracks, giving

rise to poor optical confinement. Guided modes at 635 nm are shown at these two coupling points for comparison (Figure 5.1B and D).

To improve the shape of the index profile, a temporal pulse shaper (Bio-Photonics FemtoJock) was used to stretch the pulse to 2 ps in order to reduce the lengthening of the focal volume due to nonlinear-induced self-focusing. This leads to significant improvement in laser-induced waveguide profiles and gives rise to much stronger mode confinement at both 635 nm and 1560 nm as evidenced by Figure 5.1(G, H). These results show a strong dependence of waveguide performance on the duration of the writing laser pulse, suggesting that Kerr self-focusing is the primary driving mechanism behind feature elongation. This explanation however, does not account for the increase in feature width at the longer pulse-width of 2 ps. Chalcogenides, which has similar properties to heavy-metal oxide glasses, have been shown to be susceptible to residual heating [139]. In order to take advantage of this effect and to further explore the effects of pulse width on the guided-mode characteristics of GLS laser-written waveguides, the astigmatic-beam shaping technique [86] was employed, to further improve focal distortion.

All features were written with a pulse energy of 400 nJ / pulse and a fixed translation speed of 250 $\mu\text{m/s}$. Though not all pulse-widths gave rise to visible index modification, all features still displayed evidence of sufficient index contrast to support guided modes either at 635 nm or 1560 nm.

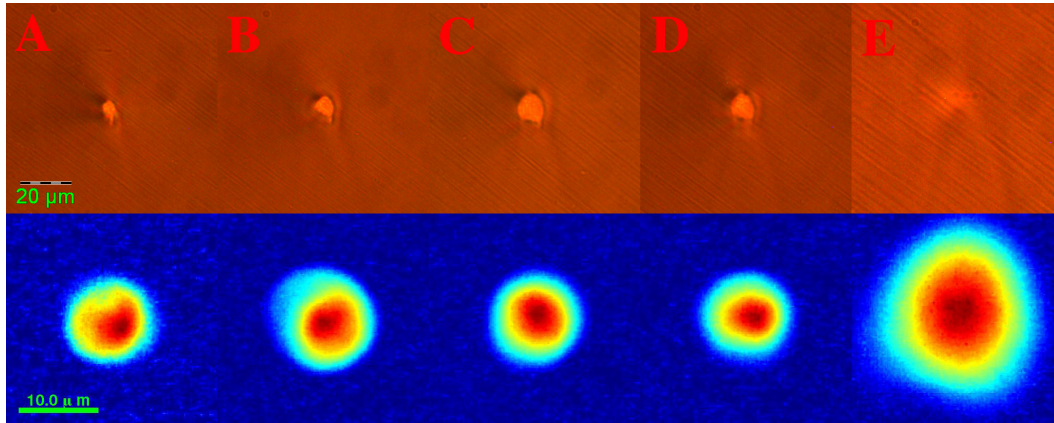


Figure 5.2 – End facet views (top) and corresponding guided modes at 1560 nm (bottom) for waveguides fabricated in GLS chalcogenide glass using the astigmatic beam shaping technique. Left to right: (A) 2.75 ps, (B) 2.1 ps, (C) 1.5 ps, (D) 1 ps, (E) 500 fs. A minimum mode field diameter of 11.3 μm was found at the waveguide written with a pulse width of 1.5 ps. For features written at 4.5 ps and 3.75 ps, guiding was only found for a wavelength of 635 nm. These features were not visible under a standard white-light microscope. Reprinted with permission from [28]. Copyright 2012, [Optical Society of America](#).

The combined spatial and temporal shaping of the writing laser produced highly symmetric waveguides, as shown in Figure 5.2. Guided modes were also found to be symmetric and centered at the laser-modified sites. For pulse-widths above 2.75 ps, guiding was only present for 635 nm. For pulse-widths between 2.75 ps and 1 ps, strong mode confinement at 1560 nm was found, indicating optimal writing conditions for minimum mode size. At shorter pulse-widths (< 1 ps), mode size was found to increase dramatically suggesting weak index contrast and poor mode confinement.

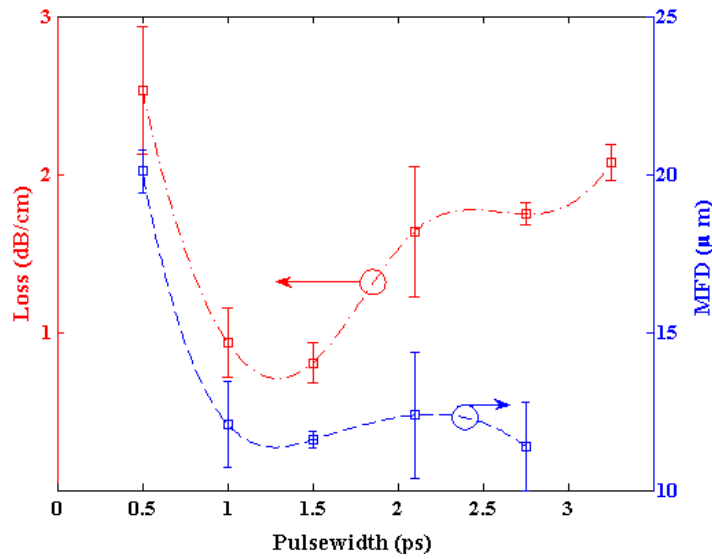
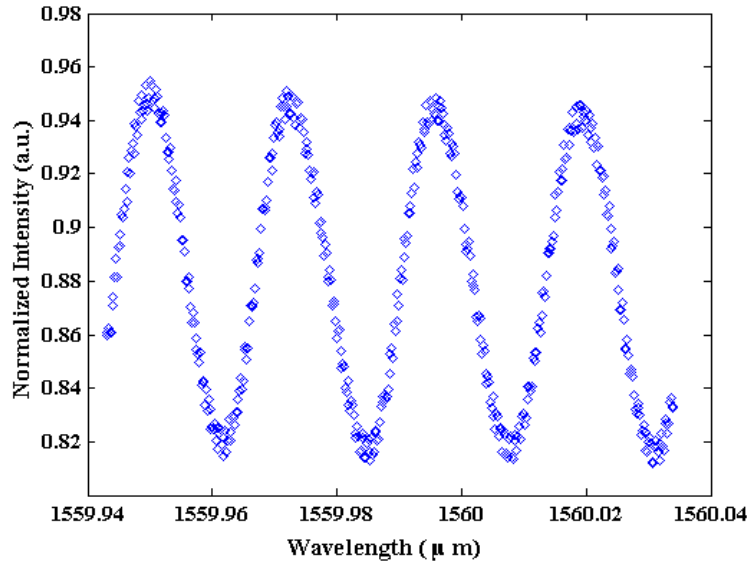


Figure 5.3 – (top) Plot of the fringe pattern obtained for the lowest loss feature written at 1.5 ps, with a loss of 0.65 db/cm and (bottom) the mode-field diameter of all guided modes and loss vs. pulse-width. Optimal writing conditions are found for features which coincide with a pulse width of 1 – 1.5 ps. Reprinted with permission from [28]. Copyright 2012, [Optical Society of America](#).

Waveguide loss measurements were performed based on the Fabry-Pérot resonance method [135,140] using a temperature-tunable DFB diode laser with a center wavelength of 1560 nm, and a wavelength tuning step size of 1 pm. Figure 5.3 (top) shows the fringe pattern for the best result, which was found to occur for features written with a pulse-width of 1.5 ps. The waveguide propagation loss, determined by the ratio of the periodic maxima to the minima of the fringe, is calculated as 0.65 dB/cm. The corresponding mode field diameters (MFD) and loss vs. pulse width are plotted together in Figure 5.3 (bottom). The data indicates an optimal processing window between 1 and 2 ps, where the minimum MFD and lowest loss coincide. There is very little sensitivity in the MFD size in relation to longer pulse widths, however it rises drastically for pulse durations less than 1 ps. Measurements have yet to be performed to map the refractive index change around the laser modification area, however comparable dimension of the laser modified area ($\sim 10\mu\text{m}$ in Figure 5.2C) and the MFD (e.g. $11.3\ \mu\text{m}$ for Figure 5.2C) measured for the 1.5 ps pulse-width suggests that the refractive index change is slightly smaller, but comparable to, the index contrast of a standard fiber.

Waveguide loss is significantly higher outside of this window, especially for shorter pulse-widths. The optimal processing window identified by this work is outside of the pulse-width provided by a typical commercial ultrafast laser, which may explain the fabrication difficulties encountered by various research groups.

In order to gain a better understanding of the trends displayed in Figure 5.3, confocal Raman imaging was performed on several structures fabricated with different pulse widths, as described elsewhere [141]. The characteristic Raman spectrum of GLS consists of broad bands whose intensity can be correlated, in a first order approximation, to the modification degree of

the original network. Figure 5.4 shows the cross sectional confocal Raman intensity images of three characteristic waveguides fabricated with pulse widths of 1, 1.5 and 2.1 ps.

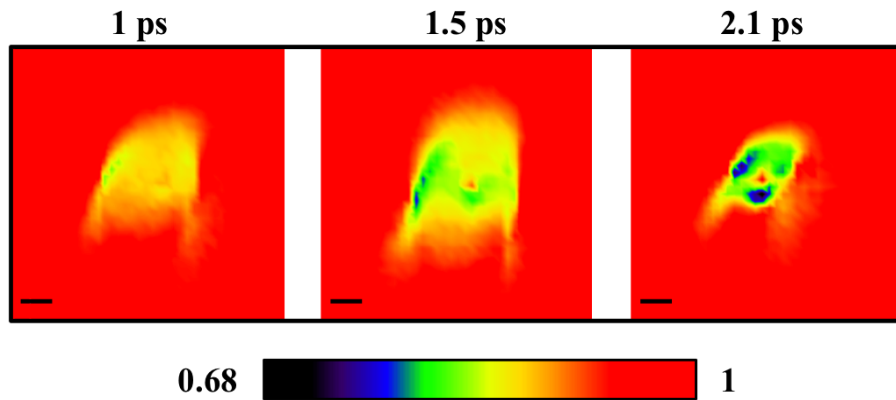


Figure 5.4 – Spatial Raman maps indicating a reduction of Raman intensity for three waveguides written pulse widths of 1, 1.5 and 2.1 ps. The scale bar in the images represents a distance of 3 μm . Reprinted with permission from [28]. Copyright 2012, [Optical Society of America](#).

For all waveguides studied in Figure 5.4, Raman back scattering intensity decreases within the guiding area, indicating the presence of broken bonds and / or extended defects, indicating that both effects likely contribute to increased propagation losses. Further analysis of this data indicates that the structure fabricated at 2.1 ps contains a larger amount of material damage, leading to larger propagation losses. This is in good agreement with the measurement results shown in Figure 5.3, where an increase in propagation loss is found for structures fabricated at pulse-widths of greater than 2 ps.

For features written in the pulse with range of 1 to 1.5 ps, the above Raman data indicates that, within this range, pulses are long enough to modify the GLS refractive index, and lead to the formation of waveguides, but do not generate a sufficient magnitude of broken bonds within the material to lead to large propagation losses. Furthermore, as indicated by the Raman data and the trends displayed in Figure 5.3, it can be concluded that pulse-widths shorter than 1 ps generate more material defects (higher intensity) as well as spread the refractive index change over a larger area (temporal distortion of the pulse), leading to higher propagation losses. Pulse-widths longer than 2 ps lack sufficient intensity to positively modify the GLS substrate for a fixed pulse energy of 400 nJ, thereby producing insufficient index change to support a well confined guiding mode.

The next section discusses the application of this temporal and spatial beam shaping technique to the fabrication of Bragg waveguides. Formation of these structures adds another level of complexity to an already complicated fabrication procedure. Spatial control of the laser-written mode size is crucial to the quality of the reflections obtained from these periodic structures, since it must be ensured that waveguides only support a single guided mode.

5.2 BRAGG WAVEGUIDES IN GLS

This chapter presents work that builds on the writing techniques presented in Section 5.1 to fabricate Bragg waveguides in GLS chalcogenide glass. The exceptionally low loss of this technique combined with the controllability of the waveguide size provides a new avenue for writing these advanced structures. First through sixth order Bragg waveguides are demonstrated with reflectivity as high as ~25 dB at 1551 nm. The application of this writing method to higher-order gratings shows promise for mid-IR applications whose fundamental Bragg wavelength lies within the range of these multi-order grating waveguides.

Bragg reflectors were first demonstrated in optical fiber [142], and have since been fabricated using the ultrafast DLW technique [143,144]. With recent interest in mid-IR applications [131], it is of great importance that the fabrication of Bragg waveguide be explored for chalcogenide glasses. These glasses are available with various doping of active ions, allowing for the fabrication of integrated mid-IR laser sources [145]. The incorporation of Bragg structures into waveguides in chalcogenide glasses will allow for reinforcement of the lasing mode, leading to greater power and efficiency from this relatively small device. Additionally, the fabricated structures may also find use for mid-IR filtering [136] and sensing [146] applications.

The Bragg waveguides studied in this work were fabricated using a single pass technique, in which periodic interruption of the writing beam forms the Bragg structure and waveguide during the same pass. The induced average DC index change is sufficient to support guided modes, while the AC refractive index modulation provides the periodic structure needed for Bragg reflections. For beam modulation, a periodic signal was fed to the cavity-dumper-on-

demand (CoD) input on the regenerative amplifier stage of the laser system, with the modulation frequency determined by:

$$f = \frac{2\nu n_{eff}}{\lambda_c} \quad \text{Equation 5.1}$$

where f is the CoD modulation frequency, ν is the writing velocity, n_{eff} is the effective refractive index, and λ_c is the Bragg wavelength. Waveguides studied in this work were designed for a center wavelength of $\lambda_c \sim 1550$ nm, and $n_{eff} \sim 2.37$ with a fixed writing velocity of $\nu = 1000$ $\mu\text{m/s}$. Figure 5.5 shows a white light microscope image of the Bragg waveguides from first through sixth order as viewed from the incident writing laser direction (top). The grating order m , is defined as $m\Lambda_1$ where Λ_1 is the first-order grating period. A uniform waveguide (referred to as “0th order” and containing no grating) is shown for comparison.

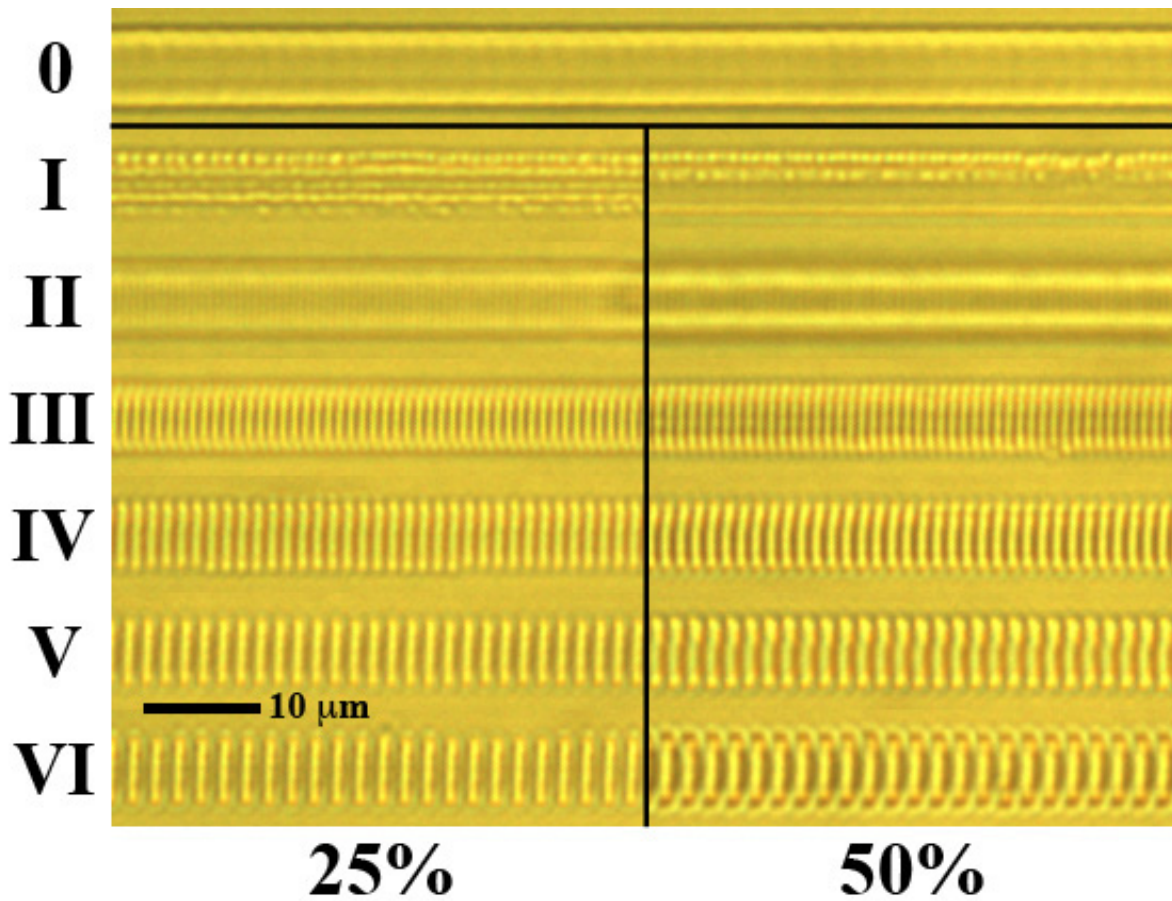


Figure 5.5 - Top view of laser written Bragg waveguides in GLS CHG glass for 25% and 50% duty cycle. First through sixth order gratings are shown with a zeroth order (no grating) waveguide shown at the top for comparison. All features were written at 300 nJ / pulse, 1 mm/s, and 1.5 ps pulse-width. The writing beam was incident into the figure, with the writing direction from right to left.

A comparison was made between two writing regimes by varying the duty cycle (mark-to-space ratio) of the modulated writing beam. It was found that using a duty cycle of 50% led to the production of lower quality gratings, possibly due to thermal effects present from the use of picosecond length pulses. In gratings from second to sixth order, the grating period is clearly visible in the image, however the first order structures showed no clear sign of periodic modulation of the index when viewed using the highest magnification available of 63x. Despite the use of a high-magnification microscope objective (Olympus Neo SPLan 80x / 0.75NA), the nominal focused spot size inside the CHG substrate ($\sim 1 \mu\text{m}$) exceeds the fundamental Bragg period ($\sim 329.5 \text{ nm}$). If thermal effects due to the use of picosecond length writing pulses are also taken into account then these two factors will contribute to a “washing out” of the grating structure.

Slight distortions of the width of the waveguides are also visible, which is believed to be due to the beam shaping method used. Any surface scratches or defects in the material which lead to an attenuation of the beam power at the focus have been found to cause changes in the width of the waveguide, as this directly affects the volume of material ionized, and hence the resulting induced index change [86].

Unlike Bragg waveguides written in materials such as silica [111,147,148] and phosphate glass [16], the individual Bragg periods of the waveguides presented here are not uniform in cross-section as shown in Figure 5.5. Each period, though uniform in spacing, shows slight variation in shape that is often not perpendicular to the propagation direction of the guided mode. At first it was believed that this may have been due to misalignment in the beam shaping telescope, but on further examination it was discovered that these distortions often orient themselves in relation to the translation direction of the writing laser beam. In the case of Figure

5.5, the writing direction was from right to left. The directional orientation is most noticeable for third and fourth order. The periods demonstrate a slight curvature, as though the writing beam were ‘dragging’ the material along with it as the waveguide was formed. As the period spacing is increased, the distortions begin to take on more complex shapes, which are most prominent for the fifth order grating written at 50% duty cycle. Generally gratings written with the lower duty cycle of 25% show fewer distortions to the individual periods, suggesting that higher average power likely contributes to thermal effects. It should be noted however that these distortions are often not uniform along the entire facet of each Bragg period. The examples given here are at roughly the same depth of focus for comparison.

Distortions in the grating periods may also be due to another phenomenon known as the “quill” effect [149-151], in which material modification shows preference to the translation direction of the writing beam due to the so-called pondermotive force set up by tilt in the pulse front. In order to obtain 1.5 ps pulses, the grating compressor in the regenerative amplifier is purposefully de-tuned to give longer pulses. We have found significant spatial chirp in the writing beam, which is evidence that pulse front tilt is present [152]. Further experiments are needed to determine if the grating quality (both spatial and spectral) may be improved with optimization of the pulse front tilt and writing direction in relation to the tilt.

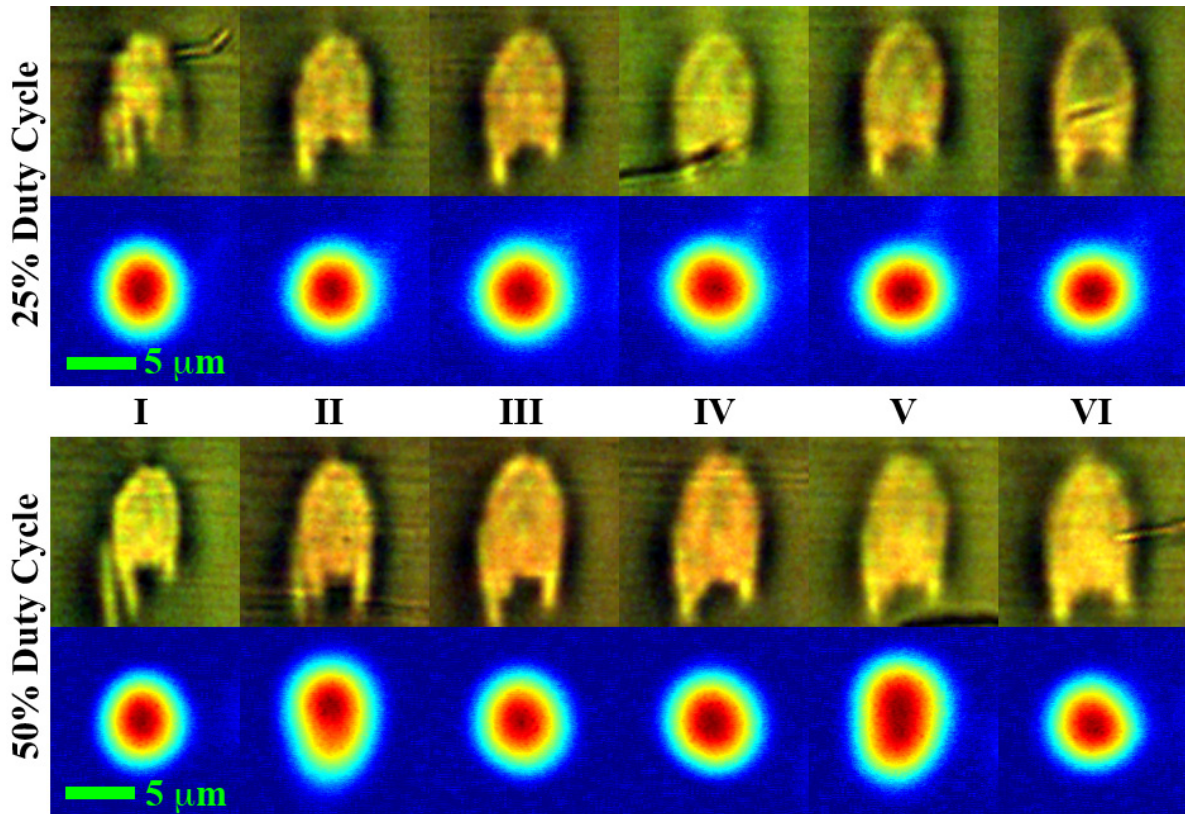


Figure 5.6 - End facet view of laser written Bragg waveguides in GLS CHG glass, showing approximate guided mode locations. All features were written at 300 nJ, 1 mm/s translation speed, and 1.5 ps pulse width. The writing laser was incident from the top of the figure. Features written with a duty cycle of 50% tended toward multi-mode guiding, suggesting increased thermal effects due to a higher average power incident on the glass, which is expected for picosecond regime laser writing.

The guided mode structure of the Bragg waveguides was studied by butt coupling 1560 nm light into one end of each of the waveguides with an SMF 28 optical fiber, while simultaneously imaging the other end with a 50x microscope objective and IR CCD camera. Figure 5.6 shows the end facet view along with guided modes at 1560 nm for Bragg waveguides written with 25% and 50% duty cycle respectively. In comparison to work presented in Section 5.1 [28], the cross-section of the waveguides is slightly elongated. Full correction of spatial distortions was not possible due to the limited entrance aperture of the 80x writing objective used (~3 mm clear entrance aperture), which was chosen for increased spatial resolution when writing lower-order gratings. For this reason, careful control of the pulse energy was needed to ensure optimal waveguide quality, while keeping the structures the proper size to support only a single guided mode.

The increased magnification of the writing objective yields comparatively smaller waveguides and hence, smaller guided modes, with a mode-field-diameter on the order of ~8 μm . Careful examination of the guided mode structure in Figure 5.6 reveals that, on average, the waveguides written with a duty cycle of 50% (higher average power) often demonstrate multi-mode guiding behavior due to a slightly larger cross-sectional waveguide size. For a duty cycle of 25% however, all structures guide a clean, single mode.

Grating spectra were obtained by coupling broadband light into each of the Bragg waveguides with an angle-cleaved fiber. The end facets of the waveguide sample were angle ground and polished to reduce back reflections from the high index material. The reflection spectra were collected using a circulator on the launch side of the waveguides while the transmitted light was simultaneously collected at the exit face. Both signals were recorded on an optical spectrum analyzer.

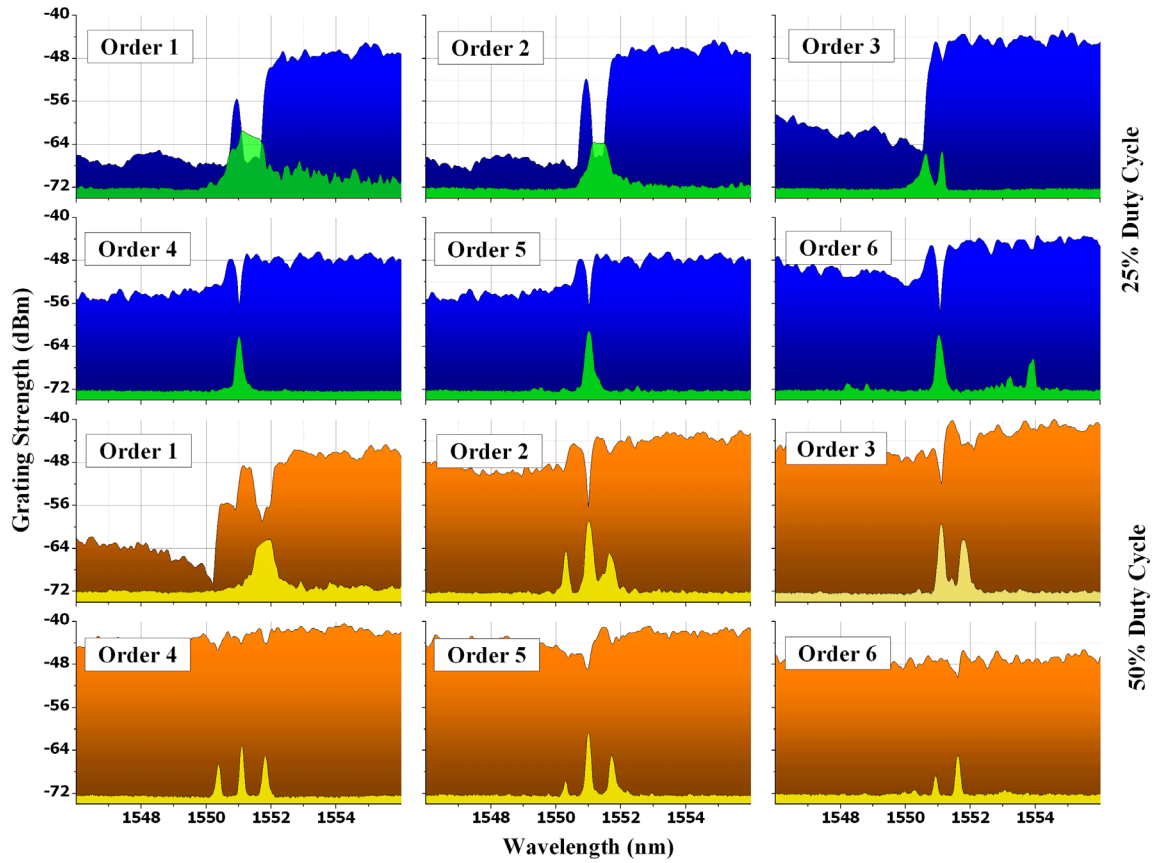


Figure 5.7 - Grating spectra for Bragg reflectors fabricated in GLS chalcogenide glass with a fixed pulse energy of 300 nJ and 1 mm/s translation speed. The top half of the figure represents spectra obtained for features written with a duty cycle of 25%, while the bottom half represents those fabricated with a duty cycle of 50%. Both reflection (green, yellow) and transmission (blue, orange) are displayed.

Figure 5.7 shows grating spectra obtained from the guiding structures obtained upon interrogation with broadband light. From this figure, it is evident that the differences in duty cycle play a role in the quality of the grating response. The top half of the figure (colored green and blue) represents first through sixth order reflection (green) and transmission (blue) spectra for gratings fabricated with a duty cycle of 25%. From a qualitative point of view, this series of grating spectra shows a trend of narrowing line-width with increasing grating order for the reflection portion of the spectrum. Additionally, fewer side-lobes and spectral artifacts are seen outside of the main central reflection peak. The transmission spectral also show considerable improvement, as less radiation loss due to an infinite cladding mode is seen for higher orders [106].

This is in sharp contrast to the lower half of the figure, which represents spectra for gratings written with a duty cycle of 50%. For all orders, a central reflection peak is always accompanied by side lobes, accompanied by a degradation of the overall quality of the spectra, displaying almost no transmission dip for orders four through six.

There are several possible explanations for the results presented here. In the case of grating written with a duty cycle of 50%, it is likely that the larger duty cycle imparts higher average power to the substrate during Bragg waveguide fabrication. This higher average power, as we have already seen in Figure 5.5, manifests itself in the form of thermal effects, which lead to distortion of the individual grating periods. While distortion of the grating is known to cause radiation mode losses [106], it is unclear whether this will impart enough modification to the grating to cause the appearance of side lobes. When compared to results for 25% duty cycle, the appearance of side structure around the main peak is almost non-existent for grating orders of four and above.

Another possible explanation is a variation in the motion error of the waveguide stage itself. These grating spectra have a similar appearance to that of another type of Bragg reflector known as a super structure grating [106,153]. If tuning of the motion control parameters is not optimized for the translation stage, the positional error for a fixed velocity will manifest itself as a sinusoidal change in acceleration over the distance traveled. Though small, this sinusoidal change in acceleration (and hence position) will impart a slow-moving (in comparison to the Bragg period) sinusoidal modulation over the length of the grating, creating a secondary fluctuation in grating period on top of the already ‘uniform’ grating.

Studies involving Bragg waveguide fabrication in other materials such as fused silica [154] have shown that multiple peaks are often found in the reflection spectra of these structures due to birefringence. This birefringence is a product of the laser fabrication process, and is easily compensated for by changing the polarization of the interrogation light. Similar techniques were used for spectral studies of the Bragg reflectors presented here, however it was found that changing the polarization of the interrogation light had little effect on the spectral position or magnitude of the reflected and transmitted peaks.

The spectral characteristics of the first order gratings for both duty cycles may also be further improved. It is believed that the limitations of spot size combined with thermal effects are the main cause for the poor spectral quality seen at the fundamental Bragg period. The use of a higher magnification objective may assist in improving spatial resolution, however a double-pass writing scheme may be required. With such a high magnification (80x, 0.75NA in this case), the limited entrance aperture of the objective restricts the total amount of correction to the spatial cross-section of the fabricated waveguide, which also limits the lateral size. Any further reduction of the waveguide size may increase losses, and lead to a structure that is too small to

guide light all together. In this situation, a uniform waveguide may be written first, followed by a grating written over the uniform waveguide during a second pass using a higher magnification objective, similar to writing techniques used to form Bragg reflectors in optical fiber [155-158]. This technique preserves the proper waveguide size for efficient guiding, but may limit the maximum index contrast generated in the grating, reducing the strength of the reflection and rejection peaks.

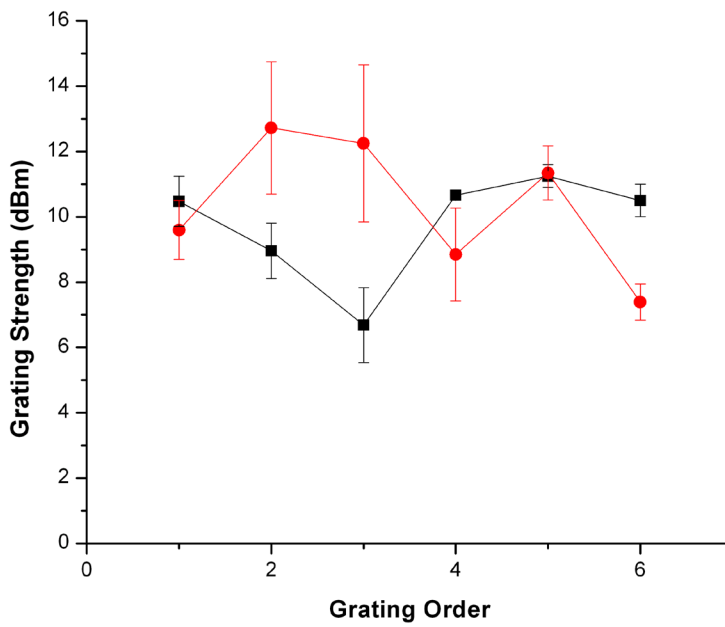
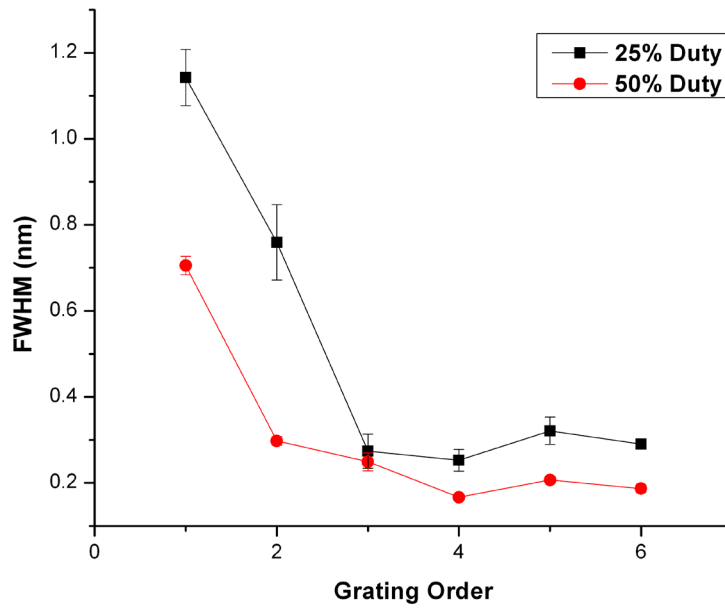


Figure 5.8 – Plots of the grating FWHM (top) and grating strength (bottom) versus grating order.

Figure 5.8 shows the reflection spectra line width (FWHM, top) and grating strength (dBm, bottom) versus grating order. The grating line width stays relatively consistent for third order gratings and larger. The values for gratings written at 25% duty cycle are slightly wider, which is expected since the lower duty cycle imparts less average power to the material, resulting in a lower index contrast of the individual grating periods. As was previously mentioned, the first and second order gratings are unusually wide due to the thermal mechanisms involved during fabrication.

The bottom plot in Figure 5.8 shows grating strength versus order. Here a fair amount of variability is found, since losses vary considerably for each grating. The end-fact quality of the sample was checked rigorously to ensure that it was free from damage and of a high optical quality. The variability seen here however is likely due to defects in the actual waveguide generated during fabrication. As was mentioned earlier, any scratches on the surface of the sample or defects within the bulk material lead to an attenuation of the incident power from the writing beam. When using the astigmatic beam shaping technique, any reduction in intensity leads to a reduction in waveguide size. In many cases, the waveguide width is significantly reduced, leading to increased scattering loss.

6.0 SUMMARY

6.1 CONCLUSION

In summary, this work presents novel device fabrication techniques, which were applied to a variety of substrates, including amorphous fused silica, lithium tantalate, crystalline sapphire, and GLS chalcogenide glass. A brief review of each of these materials will be given here.

In section 3.0 , waveguide inscription was combined with a technique known as thermal poling, in which heat is applied to the substrate in order to generate free charges, which are then preferentially drifted across the sample by applying a high-strength electric field. After a pre-determined amount of time, the heat is removed and the charges are ‘frozen in’, creating a space charge region. This space charge region is responsible for the generation of second order nonlinearities in silica glass, which under normal conditions has none. This poling technique was then combined with ultrafast laser waveguide inscription, with the intent of overlapping the SON layer with the fabricated waveguides. It was found that this was indeed possible, but the charge layer did not fully penetrate the core of the waveguide. It was believed that this was due to a reduction in ion mobility, brought about by material compaction of the glass in the irradiated region of the substrate.

Laser fabrication of waveguides was then applied to two crystalline materials in Section 4.0 , lithium tantalate and sapphire. In both of these materials, it was found that the induced

refractive index change was an indirect consequence of the laser-generated damage and that no guiding regions were found within the modified focal volume. In the case of lithium tantalate, the induced index change was found to be due to a localized compressive stress, brought about by expansion of the focal volume. Micro-Raman studies confirmed the location of the waveguide several microns away from the damage site, indicating that the index change mechanism was indeed compressive stress related. Further investigations using SH microscopy also demonstrated that the nonlinear properties are preserved within the guiding region. Additionally, the spatial separation of the guiding region from the laser-modified area ensures that the guided mode will experience minimal losses. The index change mechanism in sapphire was found to exhibit a similar behavior, however in this case the focal volume experiences an increase in density, leading to a tensile stress around the laser damage track. The induced tensile stress (not compression, as in the case of lithium tantalate) is responsible for the creation of a guiding region. Due to the relatively low magnitude of the generated change in refractive index, guiding was only found for a wavelength of 635 nm.

Finally in Section 5.0 , the ultrafast laser waveguide fabrication technique was applied to a highly nonlinear material, gallium lanthanum sulfide chalcogenide glass. This material presents unique fabrication challenges due to its inherently high nonlinearities and large refractive index. The high nonlinearity of this material poses a problem for the propagation of ultrafast laser pulses, which, as discussed in Section 2.2.2, leads to distortion of the focus due to the effects of self-focusing. This problem is further compounded by index-mismatch induced spherical aberrations. The resulting cross-section of the index change region is of poor quality and unsuitable for low-loss propagation of light. The poor mode quality also does not lend itself well for coupling to other devices, such as optical fiber. For these reasons, a technique of temporal

pulse shaping and spatial beam shaping were employed to improve the temporal and spatial profiles of the writing pulse and waveguide respectively. Nearly circular waveguides were fabricated with a lowest measured loss of 0.65 dB/cm. Losses were compared for different regimes of incident laser pulse width, and it was found that an optimal processing window exists in the range of 1 – 1.5 ps. Micro-Raman analysis confirmed a reduction in Raman signal intensity within the guiding region of the waveguides, indicating the creation of lattice defects. These defects are likely to cause increased propagation loss, and were found in greater numbers for laser pulse widths outside of this optimal processing window.

The writing technique of applying temporal and spatial beam shaping was then applied to the fabrication of Bragg waveguides in GLS. Bragg reflectors require a clean, single guided mode in order to generate a single reflection peak, making this method of fabrication necessary. Bragg waveguides were designed for a center wavelength of 1550 nm, and written in GLS from the first through sixth Bragg order. Higher order gratings were attempted for a two-fold purpose. Initially, it was discovered that the focal spot ($\sim 1 \mu\text{m}$) was much larger than the fundamental Bragg period ($\sim 320 \text{ nm}$), leading to a structure that was ‘washed out’. This was confirmed by the low-quality reflection spectra obtained for the first and second order gratings. Secondly, higher order gratings have applications for mid-IR applications, as the higher order becomes the fundamental order at longer wavelengths. Using optimized parameters from the initial experiments in GLS, Bragg reflectors were written with a duty cycle of 25% and 50%. The resulting reflection spectra demonstrated better spectral characteristics for the waveguides fabricated with a duty cycle of 25%. It is believed that this was due to the presence of thermal effects, causing the individual grating periods to ‘creep’ together during fabrication. Additionally, fluctuations in the waveguide width and spacing may lead to the appearance of

side-lobe structure in the grating spectra. Further investigation is needed to determine the cause of these spectral and spatial distortions.

6.2 FUTURE OUTLOOK

Ultrafast laser inscription of waveguides in transparent materials offers much promise for photonic device fabrication. The advantages of this direct-write technology not only reduce cycle time and cost, but allow for a greater device density and increased complexity than ever before seen in optical device production. The social implications of reduced energy consumption and cost are a driving factor, however the universal nature of this fabrication approach holds the most appeal. As technology moves forward, more and more uses for ultrafast laser fabrication are being discovered.

Though the techniques presented here are novel, they may be applied to future endeavors for the fabrication of low-loss photonic devices. As an example, though the generation of SON within laser-written waveguides in silica was un-successful (Section 3.0), the technique of thermal poling may be more easily combined with fabrication methods such as the double track approach for crystalline materials [38,141], while using crystalline quartz as the waveguide substrate. Since the mechanisms of index change are different in crystalline materials than those found in silica glasses, a localized induced stress may possibly allow for greater ion mobility into the induced guiding region, leading to the successful creation of an SON layer within the guiding region.

Likewise, the double track approach could also be successfully combined with the modulation technique used to fabricate Bragg reflectors. If implemented in active crystalline

materials such as Nd doped YAG ceramic, extremely compact waveguide lasers may be formed, which do not require external cavity mirrors to reinforce the lasing mode. Additionally, this may be taken a step further to include Ti:Sapphire crystals for the production of very small ultrafast laser sources.

As research in the field of ultrafast laser processing progresses, researchers will continue to drive an ever increasing trend of system integration, incorporating similar techniques to the ones presented here to fabricate devices which combine multi-disciplinary devices onto a common substrate. Examples of these types of microsystems have already been fabricated [5,65], and often incorporate disparate fields such as biology, fluidics, and photonics. Fabrication techniques discovered in this field will forever continue to evolve along with new and exciting devices, all based around material modification and removal through the use of an ultrafast laser.

BIBLIOGRAPHY

- [1] K.M. Davis, K. Miura, N. Sugimoto, K. Hirao, *Opt. Lett.* 21 (1996) 1729.
- [2] W.F. Brinkman, D.E. Haggan, W.W. Troutman, *IEEE J. Solid-State Circuits* 32 (1997) 1858.
- [3] C.M. Ramani, in: OFCNFOEC 2006. 2006 Optical Fiber Communication Conference and the National Fiber Optic Engineers Conference, IEEE, 2006, p. 11 pp.
- [4] A.H.J. Yang, S.D. Moore, B.S. Schmidt, M. Klug, M. Lipson, D. Erickson, *Nature* 457 (2009) 71.
- [5] A. Schaap, Y. Bellouard, T. Rohrlack, *Biomed. Opt. Express* 2 (2011) 658.
- [6] Y. Bellouard, *Opt. Mater. Express* 1 (2011) 816.
- [7] K. Oysted, *Ieee 2005 Custom Integrated Circuits Conference* 15 -3 (2005) 511.
- [8] T. Kajita, Un-Ku Moon, G.C. Temes, *IEEE Trans. Instrum. Meas.* 51 (2002) 853.
- [9] C. Doerr, *IEEE Journal of Lightwave Technology* 24 (2006) 4763.
- [10] P. Lambert, *Capillary Forces in Microassembly* by Pierre Lambert. Berlin: Springer, 2008. ISBN 978-0-387-71088-4 -1 (2008).
- [11] H. Maune, S. Han, R. Barish, M. Bockrath, *Nature* 8 (2009) 61.
- [12] Z. Wang, R. Bao, X. Zhang, X. Ou, C.-S. Lee, J.C. Chang, X. Zhang, *Angewandte Chemie International Edition* 50 (2011) 2811.
- [13] L. Xu, G. Tempea, A. Poppe, M. Lenzner, C. Spielmann, F. Krausz, A. Stingl, K. Ferencz, *Applied Physics B: Lasers and Optics* 65 (1997) 151.
- [14] Q. Cao, S. Chi, *J. Opt. Soc. Am. B* 17 (2000) 1304.
- [15] T. Brabec, F. Krausz, *Reviews of Modern Physics* 72 (2000) 545.

- [16] M. Ams, G. Marshall, D. Spence, M. Withford, *Opt Express* 13 (2005) 5676.
- [17] L.A. Fernandes, J.R. Grenier, P.R. Herman, J.S. Aitchison, P.V.S. Marques, *Opt Express* 19 (2011) 11992.
- [18] G. Della Valle, R. Osellame, *Journal of Optics a: Pure and Applied Optics* 11 (2009) 013001.
- [19] S. Sundaram, C. Schaffer, *Applied Physics a: Materials Science & Processing* 76 (2003) 379.
- [20] D. Homoelle, S. Wielandy, A.L. Gaeta, N.F. Borrelli, C. Smith, *Opt. Lett.* 24 (1999) 1311.
- [21] Y. Sikorski, A.A. Said, P. Bado, R. Maynard, C. Florea, K.A. Winick, *Electron. Lett.* 36 (2000) 226.
- [22] A.M. Streltsov, N.F. Borrelli, *J. Opt. Soc. Am. B* 19 (2002) 2496.
- [23] J. Chan, T. Huser, S. Risbud, J. Hayden, D. Krol, *Applied Physics Letters* 82 (2003) 2371.
- [24] C. Florea, K. Winick, *J. Lightwave Technol.* 21 (2003) 246.
- [25] A. Zoubir, M. Richardson, C. Rivero, A. Schulte, C. Lopez, K. Richardson, N. HÜ, R. VallÈe, *Opt. Lett.* 29 (2004) 748.
- [26] A. Saliminia, N. Nguyen, M.-C. Nadeau, S. Petit, S. Chin, R. Vallee, *Journal of Applied Physics* 93 (2003) 3724.
- [27] A. Zoubir, C. Lopez, M. Richardson, *Optics Letters* 29 (2004) 1840.
- [28] B. McMillen, B. Zhang, K.P. Chen, A. Benayas, D. Jaque, *Opt. Lett.* 37 (2012) 1418.
- [29] J. Siegel, J.M. Fernández-Navarro, A. García-Navarro, V. Diez-Blanco, O. Sanz, J. Solis, F. Vega, J. Armengol, *Applied Physics Letters* 86 (2005) 121109.
- [30] H. An, S. Fleming, B.W. McMillen, K.P. Chen, D. Snoke, *Applied Physics Letters* 93 (2008) 061115.
- [31] B. McMillen, K. Chen, Honglin An, Simon Fleming, V. Hartwell, D. Snoke, *Applied Physics Letters* 93 (2008) 111106.
- [32] A.H. Nejadmalayeri, P.R. Herman, *Opt. Lett.* 31 (2006) 2987.

- [33] T. Gorelik, M. Will, S. Nolte, A. Tuennermann, U. Glatzel, *Applied Physics a: Materials Science & Processing* 76 (2003) 309.
- [34] S.C. Jones, B.A.M. Vaughan, Y.M. Gupta, *Journal of Applied Physics* 90 (2001) 4990.
- [35] A. Benayas, D. Jaque, B. McMillen, K. Chen, *Opt Express* 17 (2009) 10076.
- [36] A. Benayas, D. Jaque, B. McMillen, K. Chen, *Journal of Applied Physics* 107 (2010) 033522.
- [37] G.A. Torchia, A. Rodenas, A. Benayas, E. Cantelar, L. Roso, D. Jaque, *Applied Physics Letters* 92 (2008) 111103.
- [38] Ben McMillen, B. Zhang, K. Chen, A. Benayas, D. Jaque, *CLEO:2011 - Laser Applications to Photonic Applications* (2011), Paper JTU1105 (2011).
- [39] S.H. Lin, P.-L. Chen, C.-I. Chuang, Y.-F. Chao, K.Y. Hsu, *Opt. Lett.* 36 (2011) 3039.
- [40] B.C. Stuart, *Phys Rev Lett* 74 (1995) 2248.
- [41] B.C. Stuart, *Phys. Rev. B* 53 (1996) 1749.
- [42] C. Schaffer, A. Brodeur, *Meas. Sci. Technol.* 12 (2001) 1784.
- [43] L.V. Keldysh, *Zh. Eksperim. I Teor. Fiz. Vol: 47* (1964).
- [44] R.R. Gattass, E. Mazur, *Nature Photon* 2 (2008) 219.
- [45] E. Yablonovitch, *Phys Rev Lett* 29 (1972) 907.
- [46] S.S. Mao, F. Qu r, S. Guizard, X. Mao, R.E. Russo, G. Petite, P. Martin, *Applied Physics a: Materials Science & Processing* 79 (2004).
- [47] K. Miura, J. Qiu, H. Inouye, T. Mitsuyu, K. Hirao, *Applied Physics Letters* 71 (1997) 3329.
- [48] L. Sudrie, M. Franco, B. Prade, A. Mysyrowicz, *Optics Communications* 171 (1999) 279.
- [49] Y. Shimotsuma, P. Kazansky, J. Qiu, *Phys Rev Lett* 91 (2003) 247405.
- [50] C. Hnatovsky, R.S. Taylor, P.P. Rajeev, E. Simova, V.R. Bhardwaj, D.M. Rayner, P.B. Corkum, *Applied Physics Letters* 87 (2005) 014104.
- [51] S. JUODKAZIS, K. NISHIMURA, S. Tanaka, H. MISAWA, *Phys Rev Lett* (2006).

- [52] A.M. Streltsov, N.F. Borrelli, *Opt. Lett.* 26 (2001) 42.
- [53] M. Will, S. Nolte, B.N. Chichkov, A. Tünnermann, *Appl. Opt.* 41 (2002) 4360.
- [54] R. Osellame, N. Chiodo, V. Maselli, A. Yin, M. Zavelani-Rossi, G. Cerullo, P. Laporta, L. Aiello, S. De Nicola, P. Ferraro, A. Finizio, G. Pierattini, *Opt Express* 13 (2005) 612.
- [55] J.W. Chan, T. Huser, S. Risbud, D.M. Krol, *Opt. Lett.* 26 (2001) 1726.
- [56] R. BRUCKNER, *Journal of Non-Crystalline Solids* 5 (1970) 123.
- [57] E.N. Glezer, E. Mazur, *Applied Physics Letters* 71 (1997) 882.
- [58] C.B. Schaffer, J.F. García, E. Mazur, *Applied Physics a: Materials Science & Processing* 76 (2003) 351.
- [59] L. Sudrie, M. Franco, B. Prade, *Optics Communications* 191 (2001) 333.
- [60] E. Bricchi, B.G. Klappauf, P.G. Kazansky, *Opt. Lett.* 29 (2004) 119.
- [61] P. Kazansky, W. Yang, E. Bricchi, J. Bovatsek, *Applied Physics Letters* 90 (2007) 151120.
- [62] P. Rajeev, M. Gertsvolf, C. Hnatovsky, *Journal of Physics B: Atomic Molecular and Optical Physics* 40 (2007) S273.
- [63] C. Hnatovsky, R.S. Taylor, E. Simova, P.P. Rajeev, D.M. Rayner, V.R. Bhardwaj, P.B. Corkum, *Applied Physics a: Materials Science & Processing* 84 (2006) 47.
- [64] A. Marcinkevičius, S. Juodkaziš, M. Watanabe, M. Miwa, S. Matsuo, H. Misawa, J. Nishii, *Opt. Lett.* 26 (2001) 277.
- [65] Y. Bellouard, A. Said, M. Dugan, P. Bado, *Opt Express* 12 (2004) 2120.
- [66] V. Maselli, R. Osellame, G. Cerullo, R. Ramponi, P. Laporta, L. Magagnin, P.L. Cavallotti, *Applied Physics Letters* 88 (2006) 191107.
- [67] S. JUODKAZIS, S. Matsuo, H. MISAWA, V. Mizeikis, A. Marcinkevicius, H.-B. Sun, Y. Tokuda, M. Takahashi, T. Yoko, J. Nishii, *Applied Surface Science* 197–198 (2002) 705.
- [68] E.N. Glezer, M. Milosavljevic, L. Huang, R.J. Finlay, T.H. Her, J.P. Callan, E. Mazur, *Opt. Lett.* 21 (1996) 2023.
- [69] C. Schaffer, N. Nishimura, E. Glezer, A. Kim, *Opt Express* 10 (2002) 196.

- [70] M. Sakakura, Phys. Rev. B 71 (2005) 024113.
- [71] M. Sakakura, M. Terazima, Y. Shimotsuma, K. Miura, K. Hirao, Opt Express 15 (2007) 5674.
- [72] S.K. Sundaram, E. Mazur, Nat Mater 1 (2002) 217.
- [73] B. Chichkov, C. Momma, S. Nolte, Applied Physics a: Materials Science & Processing 63 (1996) 109.
- [74] X. Liu, D. Du, IEEE Journal of Quantum Electronics 33 (1997) 1706.
- [75] R.W. Boyd, Nonlinear Optics (Second Edition), 2nd ed. Nonlinear Optics, 2003.
- [76] J.B. Ashcom, R.R. Gattass, C.B. Schaffer, E. Mazur, J. Opt. Soc. Am. B 23 (2006) 2317.
- [77] N. Bloembergen, IEEE Journal of Quantum Electronics 10 (1974) 375.
- [78] M. Kamata, M. Obara, Applied Physics a: Materials Science & Processing 78 (2004) 85.
- [79] J.H. Marburger, Progress in Quantum Electronics 4, Part 1 (1975) 35.
- [80] Y.R. Shen, Progress in Quantum Electronics 4, Part 1 (1975) 1.
- [81] Y.R. Shen, New York, Wiley-Interscience, 1984, 575 P. 1 (1984).
- [82] P.L. Kelley, Phys Rev Lett 15 (1965) 1005.
- [83] A. Chong, W.H. Renninger, D.N. Christodoulides, F.W. Wise, Nature Photon 4 (2010) 103.
- [84] N. Psaila, R. Thomson, H. Bookey, S. Shen, N. Chiodo, R. Osellame, G. Cerullo, A. Jha, A. Kar, Opt Express 15 (2007) 15776.
- [85] P. Günter, J.-P. Huignard, Topics in Applied Physics, Springer Berlin Heidelberg, Berlin, Heidelberg, 2005.
- [86] R. Osellame, S. Taccheo, M. Marangoni, R. Ramponi, P. Laporta, D. Polli, S. De Silvestri, G. Cerullo, J. Opt. Soc. Am. B 20 (2003) 1559.
- [87] C.B. Schaffer, A. Brodeur, J.F. García, E. Mazur, Opt. Lett. 26 (2001) 93.
- [88] S. Eaton, H. Zhang, P. Herman, F. Yoshino, L. Shah, J. Bovatsek, A. Arai, Opt Express 13 (2005) 4708.

- [89] J.W. Chan, T.R. Huser, S.H. Risbud, D.M. Krol, *Applied Physics a: Materials Science & Processing* 76 (2003) 367.
- [90] J. Burghoff, H. Hartung, S. Nolte, *Applied Physics a: Materials Science & Processing* (2007).
- [91] G.A. Torchia, C. Mendez, I. Arias, L. Roso, A. Rodenas, D. Jaque, *Applied Physics B: Lasers and Optics* 83 (2006) 559.
- [92] W.F. Silva, C. Jacinto, A. Benayas, J.R. Vazquez de Aldana, G.A. Torchia, F. Chen, Y. Tan, D. Jaque, *Opt. Lett.* 35 (2010) 916.
- [93] J. Siebenmorgen, K. Petermann, G. Huber, K. Rademaker, S. Nolte, A. Tünnermann, *Applied Physics B: Lasers and Optics* 97 (2009) 251.
- [94] R.A. Myers, N. Mukherjee, S.R.J. Brueck, *Opt. Lett.* 16 (1991) 1732.
- [95] P. Kazansky, *Optics Communications* 110 (1994) 611.
- [96] T.G. Alley, S.R.J. Brueck, R.A. Myers, *Journal of Non-Crystalline Solids* 242 (n.d.) 165.
- [97] S. FLEMING, *Journal of the Ceramic Society of Japan* 116 (2008) 1007.
- [98] H.-Y. Chen, J.-S. Sue, Y.-H. Lin, S. Chao, *Opt. Lett.* 28 (2003) 917.
- [99] A. Canagasabey, C. Corbari, Z. Zhang, P.G. Kazansky, M. Ibsen, *Opt. Lett.* 32 (2007) 1863.
- [100] M. Abe, T. Kitaga, W. Kuninori, H. Akira, H. Yasuji, Ohmori, *Integrated Photonics Research* (1996), Paper ITuD5 (1996).
- [101] J. Li, N. Myren, W. Margulis, B. Ortega, *IEEE Photonics Technology Letters* 17 (2005) 1571.
- [102] O. Tarasenko, W. Margulis, *Opt. Lett.* 32 (2007) 1356.
- [103] G. Li, K.A. Winick, A.A. Said, M. Dugan, P. Bado, *Opt. Lett.* 31 (2006) 739.
- [104] H. An, S. Fleming, G. Cox, *Applied Physics Letters* 85 (2004) 5819.
- [105] C. Corbari, J.D. Mills, O. Deparis, B.G. Klappauf, P.G. Kazansky, *Applied Physics Letters* 81 (2002) 1585.
- [106] T. Erdogan, *J. Lightwave Technol.* 15 (1997) 1277.

- [107] N. Takeshima, Y. Kuroiwa, Y. Narita, S. Tanaka, K. Hirao, *Opt Express* 12 (2004) 4019.
- [108] S.-Y. Tu, A.H. Kung, Z.D. Gao, S.N. Zhu, *Opt. Lett.* 30 (2005) 2451.
- [109] N.E. Yu, C. Kang, H.K. Yoo, C. Jung, Y.L. Lee, C.S. Kee, D.K. Ko, J. Lee, *J. Opt. Soc. Korea* 12 (2008) 200.
- [110] B. Naranjo, J.K. Gimzewski, S. Putterman, *Nature* 434 (2005) 1115.
- [111] H. Zhang, S. Eaton, J. Li, P. Herman, *Opt. Lett.* 31 (2006) 3495.
- [112] L. Gui, B. Xu, T.C. Chong, *Photonics Technology Letters, IEEE* 16 (2004) 1337.
- [113] B. McMillen, K. Chen, D. Jaque, *Applied Physics Letters* 94 (2009) 081106.
- [114] Y. Repelin, E. Husson, F. Bennani, *Journal of Physics and Chemistry of Solids* 60 (1999) 819.
- [115] A. Jayaraman, A.A. Ballman, *Journal of Applied Physics* 60 (1986) 1208.
- [116] S.M. Eaton, C.A. Merchant, R. Iyer, A.J. Zilkie, A.S. Helmy, J.S. Aitchison, P.R. Herman, D. Kraemer, R.J.D. Miller, C. Hnatovsky, R.S. Taylor, *Applied Physics Letters* 92 (2008) 081105.
- [117] C. Kittel, *Introduction to Solid State Physics*, 8th ed. Wiley, 2004.
- [118] A. Benayas, D. Jaque, S.J. Hettrick, J.S. Wilkinson, D.P. Shepherd, *Journal of Applied Physics* 103 (2008) 103104.
- [119] A. Ródenas, A.H. Nejadmalayeri, D. Jaque, P. Herman, *Opt Express* 16 (2008) 13979.
- [120] Y. Zhang, G.R. Pickrell, B. Qi, A. Safaai-Jazi, A. Wang, *Opt. Eng.* 43 (2004) 157.
- [121] J.H. Kim, M.-K. Chen, C.-E. Yang, J. Lee, S.(. Yin, P. Ruffin, E. Edwards, C. Brantley, C. Luo, *Opt Express* 16 (2008) 4085.
- [122] J. Bai, G. Cheng, X. Long, Y. Wang, W. Zhao, G. Chen, R. Stoian, R. Hui, *Opt Express* 20 (2012) 15035.
- [123] V. Apostolopoulos, L.M.B. Hickey, D.A. Sager, J.S. Wilkinson, *Opt. Lett.* 26 (2001) 1586.
- [124] A.A. Anderson, R.W. Eason, L.M.B. Hickey, M. Jelinek, C. Grivas, D.S. Gill, N.A. Vainos, *Opt. Lett.* 22 (1997) 1556.

- [125] A. Crunteanu, M. Pollnau, G. Jänchen, C. Hibert, *Applied Physics B: Lasers and Optics* 75 (2002) 15.
- [126] V. Apostolopoulos, L. Laversenne, T. Colomb, C. Depeursinge, R.P. Salathe, M. Pollnau, R. Osellame, G. Cerullo, P. Laporta, *Applied Physics Letters* 85 (2004) 1122.
- [127] R.A. Forman, G.J. Piermarini, J.D. Barnett, S. Block, *Science* 176 (1972) 284.
- [128] Q. Ma, D.R. Clarke, *J American Ceramic Society* 76 (1993) 1433.
- [129] N.M. Balzaretti, J.P. Denis, J.A.H. da Jornada, *Journal of Applied Physics* 73 (1992) 1426.
- [130] I. Horcas, R. Fernandez, J.M. Gomez-Rodriguez, J. Colchero, J. Gomez-Herrero, Baro, *Rev. Sci. Instrum.* 78 (2007) 013705.
- [131] N. Carlie, J. Musgraves, B. Zdyrko, I. Luzinov, J. Hu, V. Singh, A. Agarwal, L. Kimerling, A. Canciamilla, F. Morichetti, A. Melloni, K. Richardson, *Opt Express* 18 (2010) 26728.
- [132] M. Galili, J. Xu, H. Mulvad, *Opt Express* 16 (2009) 2182.
- [133] A. Rodenas, A. Benayas, J.R. Macdonald, J. Zhang, D.Y. Tang, D. Jaque, A.K. Kar, *Opt. Lett.* 36 (2011) 3395.
- [134] M. Pelusi, V. Ta'Eed, L. Fu, E. Magi, *IEEE Journal of Selected Topics in Quantum Electronics* 14 (2008) 529.
- [135] M. Hughes, W. Yang, D. Hewak, *Applied Physics Letters* 90 (2007) 131113.
- [136] A. Ródenas, G. Martin, B. Arezki, N. Psaila, G. Jose, A. Jha, L. Labadie, P. Kern, A. Kar, R. Thomson, *Opt. Lett.* 37 (2012) 392.
- [137] A.M. Weiner, *Rev. Sci. Instrum.* 71 (2000) 1929.
- [138] R. Curry, S. Birtwell, A. Mairaj, X. Feng, *Journal of Non-Crystalline Solids* 351 (2005) 477.
- [139] M. Sakakura, M. Shimizu, Y. Shimotsuma, *Applied Physics Letters* 93 (2008) 231112.
- [140] G.T. Reed, A.P. Knights, *Silicon Photonics: an Introduction*, 1st ed. Wiley, London, 2004.
- [141] A. Rodenas, G.A. Torchia, G. Lifante, E. Cantelar, J. Lamela, F. Jaque, L. Roso, D. Jaque, *Applied Physics B: Lasers and Optics* 95 (2009) 85.

- [142] K.O. Hill, Y. Fujii, D.C. Johnson, B.S. Kawasaki, *Applied Physics Letters* 32 (1978) 647.
- [143] H. Zhang, S.M. Eaton, J. Li, P.R. Herman, *Electron. Lett.* 42 (2006) 1223.
- [144] C. Miese, M.J. Withford, A. Fuerbach, *Opt Express* 19 (2011) 19542.
- [145] T. Schweizer, D.W. Hewak, D.N. Payne, T. Jensen, G. Huber, *Electron. Lett.* 32 (1996) 666.
- [146] R.J. Martín-Palma, V. Torres-Costa, C.G. Pantano, *J. Phys. D: Appl. Phys.* 42 (2009) 055109.
- [147] H. Zhang, S.M. Eaton, P.R. Herman, *Opt Express* 14 (2006) 4826.
- [148] H. Zhang, S. Eaton, P. Herman, *Opt. Lett.* 32 (2007) 2559.
- [149] P.G. Kazansky, Technical Meeting IEEE Photonics Society on Technology and Applications of Ultrafast Laser Inscription (2009).
- [150] P.G. Kazansky, Y. Shimotsuma, J. Qiu, W. Yang, M. Sakakura, M. Beresna, Y. Svirko, S. Akturk, K. Hirao, *Advanced Laser Technologies* (2009).
- [151] P. Kazansky, M. Beresna, Y. Shimotsuma, *Osa / Bgpp 2010* (2010).
- [152] Y. Shimotsuma, M. Sakakura, P.G. Kazansky, M. Beresna, J. Qiu, K. Miura, K. Hirao, *Advanced Materials* 22 (2010) 4039.
- [153] C. Lu, J. Cui, *Optical Fiber Technology* 14 (2008) 97.
- [154] H. Zhang, S. Eaton, J. Li, A. Nejadmalayeri, P. Herman, *Opt Express* 15 (2007) 4182.
- [155] D. Grobnic, S.J. Mihailov, R.B. Walker, C.W. Smelser, C. Lafond, A. Croteau, *IEEE Photon. Technol. Lett.* 19 (2007) 943.
- [156] D. Grobnic, C. Smelser, R. Walker, *IEEE Photon. Technol. Lett.* 18 (2006) 2686.
- [157] D. Grobnic, Stephen J Mihailov, Christopher W Smelser, Robert B Walker, Huimin Ding ED, *Bragg Gratings, Photosensitivity, and Poling in Glass Waveguides* (2010) BWA1.
- [158] D. Grobnic, Stephen J Mihailov, Christopher W Smelser ED, *Bragg Gratings, Photosensitivity, and Poling in Glass Waveguides* (2007) BWB4.